

Combined lidar and radar observations of vertical motions and heterogeneous ice formation in mixed-phase layered clouds

Field studies and long-term monitoring

Der Fakultät für Physik und Geowissenschaften
der Universität Leipzig
eingereichte

DISSERTATION

zur Erlangung des akademischen Grades

DOCTOR RERUM NATURALIUM
(DR. RER. NAT.)

vorgelegt

von Diplom-Physiker Johannes Bühl
geboren am 21. September 1983 in Reutlingen

Leipzig, den 25. September 2014

Contents

Contents	3
1 Introduction	5
2 Heterogeneous ice formation: The role of vertical air motions	9
2.1 Interactions between aerosols, atmospheric dynamics and clouds	9
2.2 Active versus passive remote sensing of clouds	10
2.3 Review of recent literature on the theory of mixed-phase cloud parcels . .	11
2.4 Connecting observations with simulations	16
2.5 Arising questions	18
3 Lidar and radar synergy. Part I: Signal strength	19
3.1 Description of lidar and radar backscattering	19
3.2 Detection of spherical and non-spherical particles with lidar and radar . .	25
4 TROPOS remote-sensing facility for simultaneous profiling of aerosols, clouds and meteorological parameters	31
4.1 Instrument overview	31
4.2 Measurement example	33
4.3 Measurement strategy for the UDINE campaign at Leipzig (2010–2013) .	35
4.4 LACROS data storage and processing	36
4.5 Mixed-phase cloud classification scheme	38
5 Lidar and radar synergy. Part II: Vertical-velocity measurement with Doppler lidar, cloud radar and wind profiler	41
5.1 Doppler wind lidar	41
5.2 Cloud-radar data processing	56
5.3 Linking Doppler lidar and cloud radar	57
5.4 Capabilities of lidar and radar to probe turbulence	60
5.5 Combined observations with Doppler lidar, cloud radar and wind profiler	62
6 Vertical-velocity and glaciation statistics of mid-latitude and sub-tropical layered clouds	71
6.1 Overview about UDINE and SAMUM campaigns	71
6.2 Case studies from UDINE	75
6.3 Observation of cloud freezing with LACROS	80
6.4 Quantification of heterogeneous ice formation in mixed-phase layered clouds	84

6.5	Combined lidar/radar vertical-wind statistics in layered clouds	88
7	Towards the measurement of ice-particle flux from cloud-radar spectra	101
7.1	A measure for the particle nucleation rate accessible by remote sensing .	102
7.2	Deriving ice-particle flux from cloud-radar spectra	104
7.3	Preparation of cloud-radar spectra	105
7.4	Case studies	107
7.5	Size separation of particles	115
7.6	Discussion of errors and scope of the method	115
8	Summary, conclusions and outlook	119
8.1	Summary and conclusions	119
8.2	Outlook	121
	Bibliography	125
	List of symbols	137
	List of abbreviations	141

1 Introduction

Clouds always cover about two thirds of the Earth’s surface. They thus determine the Earth’s albedo to a high degree and are an important regulator of the global radiation balance. Therefore, they pose a crucial component in numeric climate projections. Even small errors in the knowledge about physical composition and global distribution of clouds can lead to high uncertainties in the estimation of the human impact on the presently observed change in global climate.

In the last report of the Intergovernmental Panel on Climate Change (IPCC) aerosol-cloud interactions (ACI) were identified as one of the most uncertain components of human climate impact [Boucher et al., 2014]. The direct influence of aerosol properties on clouds [Twomey, 1977] and the numerous fast adjustments [Albrecht, 1989] of the cloud systems are estimated to create an effective radiative forcing of -0.45 W m^{-2} , but with an uncertainty of around 100%. At present state of knowledge, changes in cloud properties seem to be one of the strongest components counteracting the radiative forcing of $+1.68 \text{ W m}^{-2}$ introduced by human CO_2 emissions.

Comparisons between model outputs and satellite observations showed that the prediction of clouds is still fairly inaccurate [Zhang et al., 2010b]. There is a considerable lack of process-level understanding, especially for mixed-phase clouds which contain liquid water and ice particles at the same time. Within and around such mixed-phase clouds a complex interplay between aerosols, water and air motions takes place. The Leibniz Institute for Tropospheric Research at Leipzig (TROPOS) has been active in investigating aerosols and clouds since the foundation of the institute in the year 1992. Aerosol fluxes into clouds [Engelmann et al., 2008; Schmidt et al., 2013] and long-range aerosol transport [Baars et al., 2011; Groß et al., 2011; Müller et al., 2005] have been explored along with mixed-phase cloud freezing processes [Ansmann et al., 2005, 2009; Seifert et al., 2010; Kanitz et al., 2011] by means of lidar remote sensing. Activities of other groups on this topic include lidar measurements in arctic mixed-phase clouds [de Boer et al., 2009] and aircraft measurements in mixed-phase mid-level clouds [Fleishauer et al., 2002; Noh et al., 2012; Korolev and Isaac, 2006; McFarquhar et al., 2013]. The CloudSat and CALIPSO (Cloud-Aerosol Lidar and Infrared Pathfinder Satellite Observations) satellites are used for combined lidar/radar measurements from space to probe the cloud top height and the properties of falling ice particles below the cloud at the same time [Zhang et al., 2010a,b]. In the context of this work, “cloud top” and “cloud base” refer to the vertical extent of the predominantly liquid top of a cloud layer. The height range below this top layer, where particles may deposit, is called “virga”.

Air- and spaceborne measurement techniques at the same time have their limitations. Aircraft can deliver unique measurements of liquid water and ice crystals, but they can only measure at one height at the same time. They can either observe ice formation at

cloud top or the resulting ice crystals at cloud base. Also flying through supercooled liquid- or mixed-phase layers is difficult because of aircraft and instrument icing. From space, a detailed look into the processes and the determination of specific particle properties is not possible.

The recent efforts brought insight into the effects that aerosol particles have on clouds. But the dynamics of the aerosol-cloud interaction is still poorly understood [Morrison et al., 2012]. Information about air movement in and around the clouds are largely absent, although air motions mediate the interaction between aerosols and cloud droplets. Gravity waves can create a cloud, turbulence can entrain aerosol particles in and out of a cloud. Small-scale vertical movements lead to regular changes in water-vapor supersaturation controlling the evaporation and growth of cloud droplets. The role of vertical air motions and turbulence in the formation of ice particles and in the regulation of the Wegener–Bergeron–Findeisen (WBF) process has been found to be unclear by Korolev [2007]. However, any approach to this problem is hampered by the absence of measurements giving direct and quantitative information about vertical motions in the vicinity of clouds. The following chapter gives an overview about this problem.

For the continuous observation of aerosols, clouds and their interactions TROPOS built the multi-instrument measurement platform LACROS (Leipzig Aerosol and Cloud Remote Observations System). LACROS combines the abilities of advanced Raman/polarization lidars [Althausen et al., 2000, 2009; Mattis et al., 2004], a cloud radar, a Doppler lidar [Engelmann et al., 2008; Bühl et al., 2012], a microwave radiometer [Rose et al., 2005] and several auxiliary measurement systems to provide important parameters of aerosol and cloud layers simultaneously. Its lidars mainly sense aerosol particles and small droplets at predominantly liquid cloud bases. The cloud radar delivers information about the presence and the properties of large ice particles falling in the virgae. The difference between the lidar and radar systems is analyzed in detail in Chapter 3. LACROS as a whole is described in Chapter 4.

The combination of lidars and radars is used here for the first time to draw a coherent picture of the processes within turbulent cloud layers in the middle troposphere. In this way, height, phase (liquid, mixed-phase or ice) and vertical velocity at cloud bases of mid-level layered clouds are probed simultaneously. Layered clouds are ideal targets for the observation and investigation of cloud-droplet freezing processes. They can be penetrated completely by both lidar and radar and show narrow constraints on environmental variables like pressure and temperature. Knowledge about the complete vertical wind field around such a cloud system and inside its turbulent layers is needed for the quantification and understanding of the physical processes. Large-scale vertical motions are important for the generation of clouds (e.g., gravity waves). Small-scale turbulence is the dominant driver for the microphysics within a cloud layer. Formation of ice crystals via contact or immersion freezing, the generation of large droplets, support or inhibition of the WBF process and the recreation of liquid drops in the presence of ice crystals critically depend on vertical air motion [Korolev and Isaac, 2003].

This work aims in particular at the integration of Doppler lidar data into continuous measurements and field campaigns of TROPOS with LACROS. Despite the need for those measurements, there is currently no measurement instrument that is specifically

designed to measure vertical wind fields at cloud base. Cloud radars simply do not sense the small droplets, and the signal from Doppler lidars is contaminated by artifacts caused by the large signal gradient at cloud base and the laser pulse chirp. In Chapter 5, methods are introduced to reduce these artifacts and accurately derive vertical air velocity in the vicinity of clouds, especially at cloud bases. These methods have been developed in the framework of this thesis. In Chapter 5, also the results of a small measurement campaign conducted at the Meteorological Observatory Lindenberg (MOL, Germany) are shown. Lidars and cloud radars can measure the vertical wind field inside, but usually not around cloud layers due to the absence of tracer targets. The air motion itself, however, can be sensed by wind profilers exploiting Bragg scattering in clear air [Strauch et al., 1984]. In a cooperative effort between TROPOS and the German Meteorological Service (DWD, Deutscher Wetterdienst), simultaneous operation of a wind profiler, a Doppler lidar and a cloud radar was tested at MOL for the first time. This unique combination of instruments allows the independent observation of large-scale air motion, small-scale turbulence and particle fall velocities inside complex cloud scenes. The effort was motivated by experience from measurements with LACROS and is intended to show a way towards obtaining the complete picture of vertical motions in the vicinity of clouds.

A comprehensive statistics of vertical motion patterns at cloud base was collected with Doppler lidar during the UDINE (Up- and Downdrafts in Drop and Ice Nucleation Experiment, Leipzig, 2010–2013) and SAMUM-2 (Saharan Mineral Dust Experiment, Cape Verde, 2008) projects, offering the unique opportunity to compare mid-latitude and sub-tropical layered clouds. Combined with the simultaneous measurements of powerful polarization lidars (UDINE and SAMUM-2) and a cloud radar (UDINE), a comprehensive look into the processes of ice formation and vertical motion is possible for the first time. In Chapter 6, the statistics of vertical velocity at cloud bases is presented together with the simultaneously measured properties of ice crystals falling from the cloud base. Basic ice cloud properties (e.g., ice-water content) are evaluated with classic and proven methods [e.g., Hogan et al., 2006]. In Chapter 7, a new method is proposed to measure the flux of ice crystals through cloud base to get an idea of the nucleation efficiency in cloud layers. The particle size spectra necessary for this approach are derived from radar spectra based on the terminal fall velocities of ice crystals. The proposed method relies on a combination of Doppler lidar, cloud radar and wind profiler to retrieve the true terminal fall velocity of the particles relative to the surrounding air. Chapter 8 summarizes the work and gives an outlook on further steps to be taken.

2 Heterogeneous ice formation: The role of vertical air motions

2.1 Interactions between aerosols, atmospheric dynamics and clouds

The IPCC report 2013 states that “clouds and aerosols continue to contribute the largest uncertainty to estimates and interpretations of the Earth’s changing energy budget”. Clouds and aerosols cannot be treated independently, because aerosols acting as cloud condensation nuclei (CCN) are an abundant resource present in any place where a water cloud may form. Once activated, the cloud droplet in turn changes the chemical and physical properties of the CCN and influences its ability to form again a new droplet after evaporation. Activation and a possible subsequent freezing of water droplets can only occur, if supersaturation over liquid water is reached. Two possible ways towards supersaturation are radiative cooling of moist air or vertical movement leading to a temperature drop and hence a rise in relative humidity above the water-vapor supersaturation level. The actual freezing behavior of liquid droplets is then governed by an even more mysterious form of aerosols – the ice nuclei (IN). They only make up a very tiny fraction of all particles in the air, but at temperatures above $-38\text{ }^{\circ}\text{C}$ the presence of IN is required for droplet freezing and cloud glaciation. DeMott et al. [2010] showed that at $-20\text{ }^{\circ}\text{C}$ the fraction of IN in all aerosol particles larger than $0.5\text{ }\mu\text{m}$ in diameter is on average 10^{-3} . The temperature at which glaciation occurs is strongly connected with the IN composition [Stratmann et al., 2004; Hartmann et al., 2013; Phillips et al., 2013] and hence with their geographic origin [Seifert et al., 2010].

Both transport of aerosols and the formation of clouds can be observed in the atmosphere by means of remote sensing [Seifert et al., 2010; Kanitz et al., 2011]. But once a cloud has formed, the physical processes are usually hidden inside of the cloud layer in a mostly turbulent environment. The partitioning of liquid droplets and ice particles is thus difficult and one of the main reasons why the process-level understanding of mixed-phase clouds is low. However, for precise climate projections process-level understanding is critical, because phenomenological parameterizations solely based on present-day observations may lose their validity in future due to changes in the environmental conditions.

The complexity of mixed-phase clouds cannot be resolved by a single measurement system alone but needs combined measurements that probe different parameters at once. Already now it is clear that it will take years of continuous measurements all over the world to unravel the in-cloud processes in sufficient detail to make accurate cloud

predictions. Mixed-phase cloud processes play a role in different kind of clouds but accurate measurements are difficult. Lidars, e.g., cannot penetrate to the center of a convective thunderstorm cloud where even for radars signal attenuation is so strong that quantitative use of the signal is very limited. As measurement values from thin layered clouds are most easy to obtain and to evaluate, they are a good starting point for the kind of study carried out in this work.

While the challenging interaction between aerosol particles and cloud droplets poses a lot of unknowns, abundant and promising research is going on in this field [Hartmann et al., 2011; Chernoff and Bertram, 2010]. First-hand information about in-cloud turbulence however is virtually absent. Some aircraft studies [Fleishauer et al., 2002; Field et al., 2004] are present, but the observation is usually restricted to a few cases. This work aims at filling this gap for tropospheric mid-level layered clouds in the mid-latitudes and the sub-tropics. For that purpose, the first three years of LACROS observations at Leipzig are evaluated together with measurements from the SAMUM-2 campaign that took place at Praia, Cape Verde.

2.2 Active versus passive remote sensing of clouds

Active remote sensing with lidar and radar can yield precise information about the state of the atmosphere in general and about the properties of clouds in particular. The time and height resolution is usually on the order of seconds and tens of meter, respectively. For this work, the height, temperature, liquid/ice mixing state and vertical velocity at cloud base have to be collected simultaneously for each layered cloud under study. Passive remote-observation instruments like hyperspectral instruments on satellites provide information from a much wider field of view, deliver basic microphysical properties of clouds and allow some estimations of cloud top height. For the determination of the physical state of a layered cloud, active remote sensing allows for much more reliable and direct information. Ambiguities in the determination of height are smaller and ice crystals falling through the cloud base can be detected and classified unambiguously. Moreover, Doppler lidars or cloud radars even provide the only known methods to potentially determine vertical velocity at cloud base.

Figure 2.1a shows the satellite image of a cloud scene over Leipzig and the corresponding Doppler lidar and cloud radar measurements made at TROPOS around the same time. While the passive satellite cameras can only detect the mere presence of a cloud, the Doppler lidar and cloud radar at TROPOS detect strong vertical movements of up to $\pm 0.5 \text{ m s}^{-1}$ at the top of the cirrus layer. Below the high cirrus clouds, smaller layers of mid-level clouds become visible around 6:00 UTC (Coordinated Universal Time) showing up- and downdrafts alternating in the range of $\pm 1.0 \text{ m s}^{-1}$ on a much smaller time scale. By the time the cloud has moved over TROPOS, it may have changed, but the statistical behavior of the vertical motions may be representative for the cloud scene captured by the satellite. The example from Fig. 2.1 shows, how the combination of different remote-sensing instruments can upvalue the single systems.

Already in Fig. 2.1 the different sensitivities of Doppler lidar and cloud radar are

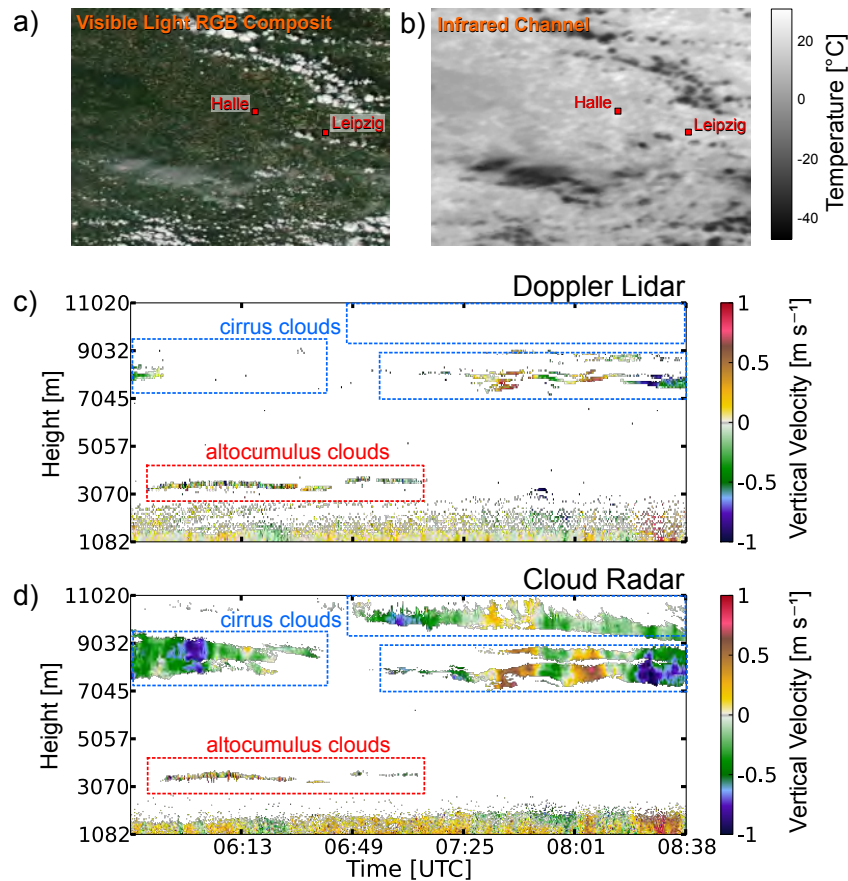


Figure 2.1: Visible-light (a) and infrared-light (b) satellite measurements taken at 9:21 UTC on 22 May 2013 are shown together with the corresponding Doppler lidar (c) and cloud radar (d) measurements between 6:00 and 8:38 UTC (Image Credit: United States Geological Survey). Positions of cloud layers are marked by the blue (high-level clouds) and red boxes (mid-level clouds). The measurement quantities of the single systems are discussed in Chapter 3.

visible. The high-level cirrus clouds (blue boxes) detected by the cloud radar are only partly visible in the Doppler lidar plots. On the other hand, the Doppler lidar detects the altocumulus (AC) cloud (red box) some minutes earlier.

2.3 Review of recent literature on the theory of mixed-phase cloud parcels

The microphysics of a mixed-phase cloud is dominated by the interplay between aerosols, water droplets, ice crystals and water vapor. At temperatures below 0 °C humid air has a slightly lower saturation vapor pressure over ice than over liquid water. If both liquid water and ice are present in a stationary air parcel, this leads to an evaporation of the liquid droplets and to a simultaneous growth of the ice crystals. This basic microphysical behavior of such a mixed-phase air parcel was first described a century ago by Wegener

[1911], Bergeron [1935] and Findeisen [1938] and is consequently called the Wegener–Bergeron–Findeisen (WBF) process.

2.3.1 Glaciating time of a mixed-phase cloud

A mixed-phase air parcel which does not move vertically and does not lose ice via deposition will eventually reach an equilibrium state with only ice crystals present. This basic consequence of the WBF theory contradicts observations in nature where mixed-phase cloud layers are observed to maintain their mixed-phase state over hours [Ansmann et al., 2009]. Korolev and Mazin [2003] showed that even small vertical velocities can significantly increase the glaciating time. In Fig. 2.2 the time until complete glaciation for a cloud parcel with a constant liquid water content (LWC), but different water-droplet number concentrations and mean droplet sizes is shown in dependence of vertical velocity. For an air parcel in rest the glaciating time is about 200 s, an updraft of 0.5 m s^{-1} already leads to a doubling of this value. However, after a certain time equilibrium will be reached and the formerly mixed-phase cloud will have glaciated completely.

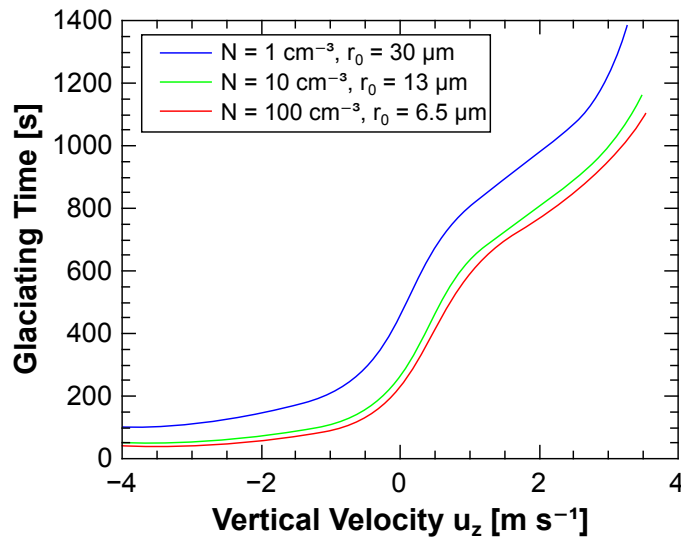


Figure 2.2: Glaciating time of a cloud parcel for different realistic cloud droplet and ice crystal configurations. The LWC is constant at 0.1 g kg^{-1} . N is the number concentration and r_0 the initial size of the water droplets at the begin of the simulation. The number of ice crystals is $N_i = 1 \text{ cm}^{-3}$, IWC is zero at the beginning, temperature is $T = -10 \text{ }^\circ\text{C}$. (Figure reproduced from Korolev and Mazin [2003].)

2.3.2 Supersaturation in a vertically moving mixed-phase cloud parcel

The analytical treatment of the supersaturation in cloud parcels goes back to Squires [1952]. In Korolev and Field [2008] the “effect of dynamics on mixed-phase clouds” is analyzed and it is shown that a turbulent layered cloud can maintain its mixed-phase

composition by constantly recreating liquid water from the vapor phase via upward motion. If an air parcel is ascending fast enough, the vapor pressure can surpass saturation over liquid water. CCN will then instantly activate liquid droplets which will eventually evaporate again when the parcel is no longer ascending fast enough. If the air parcel is in harmonic oscillatory motion, the ice crystals will grow during ascent and — if liquid droplets are present — even a short period during descent. During descent, the ice crystals will evaporate and release water vapor, which will facilitate the re-activation of liquid droplets during the next ascent. The supersaturation over liquid water S_w in a mixed-phase cloud parcel displaced vertically with constant velocity u_z can be described by the differential equation [Korolev and Mazin, 2003]

$$\frac{1}{S_w + 1} \frac{dS_w}{dt} = a_0 u_z - a_2 B_i^* N_i r_i - (a_1 B_w N_w r_w + a_2 B_i N_i r_i) S_w. \quad (2.1)$$

The particle size distribution is assumed to be monodisperse. N_i , N_w , r_i and r_w are the corresponding number concentrations and particle radii for ice and water, respectively. $a_0, a_1, a_2, B_i, B_i^*$ and B_w are constants holding thermodynamic parameters like temperature and latent heat of fusion. For a detailed description please refer to Korolev and Mazin [2003]. Eq. (2.1) is the mathematical representation of the WBF process. a_0 is a positive constant, so a source of water vapor is created on the right-hand side of the equation, if an air parcel is moving upwards ($u_z > 0$). The other terms represent the presence of ice crystals and liquid droplets and act as sinks of water vapor. Korolev and Mazin [2003] also show that Eq. (2.1) has the solution

$$S_w = \frac{S_{\text{qsw}} - C_0 \exp(-t/\tau_p)}{1 + C_0 \exp(-t/\tau_p)}, \quad (2.2)$$

with

$$S_{\text{qsw}} = \frac{a_0 u_z + b_i^* N_i r_i}{b_w N_w r_w + b_i N_i r_i} \quad (2.3)$$

and

$$\tau_p = \frac{1}{a_0 u_z + b_w N_w r_w + (b_i + b_i^*) N_i r_i}. \quad (2.4)$$

τ is the time of phase relaxation, describing the time until the air parcel has reached again its original phase state. C_0 holds the start parameters and b_w, b_i and b_i^* hold thermodynamic constants. Values of the constants are given in Korolev and Mazin [2003]. Equation (2.2) is called the “quasi-steady solution”, valid only if assumed that neither liquid nor ice particles change in size and environmental conditions are constant – in general a somewhat unrealistic assumption. However, as layered clouds have a small vertical extent and consequently do not involve deep convection, Eq. (2.2) can be useful to depict basic processes within the cloud layer. For $t \rightarrow \infty$, S_{qsw} will be the equilibrium supersaturation of the air parcel. To maintain a liquid phase, S_{qsw} must be ≥ 0 . From

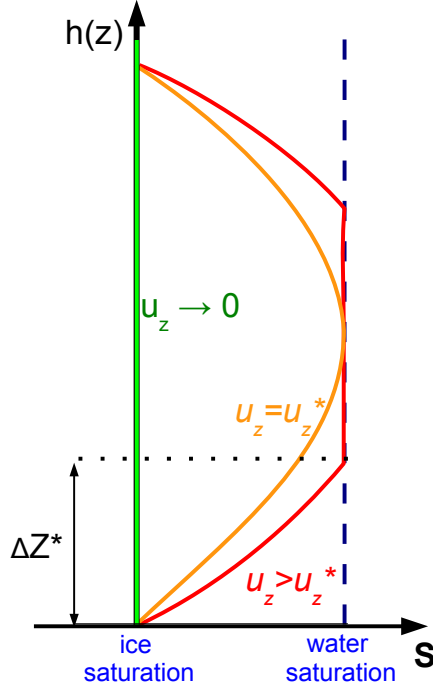


Figure 2.3: Supersaturation development in an ice-containing cloud parcel for different updraft velocities. The green line shows an infinitesimally slow ascent which leads to saturation always being at supersaturation over ice, because the ice particles have enough time to consume all surplus water vapor. The orange line shows a faster ascent with the “critical updraft velocity” u_z^* , and saturation over liquid water is reached for a moment. In the third scenario (red line) the updraft velocity is higher than u_z^* , so that supersaturation over liquid water is reached and water droplets can be activated. The growing ice crystals then consume all water vapor and later make the droplets to evaporate again. For the third scenario, the corresponding critical updraft height ΔZ^* is depicted.

Eq. (2.3), it follows that a critical vertical velocity

$$u_z^* = \frac{b_i^* N_i r_i}{a_0} \quad (2.5)$$

is necessary to maintain the liquid phase by keeping supersaturation over water positive.

Figure 2.3 shows schematically the development of the supersaturation over ice and liquid water in an ascending mixed-phase air parcel for three cases: one theoretical scenario with infinitesimally slow ascents and two realistic updraft scenarios. It is visible from Fig. 2.3 that an updraft must have a certain strength and a certain duration (red line) for the air parcel to reach saturation over liquid water. Korolev and Mazin [2003] and Korolev and Field [2008] called these two parameters the “critical updraft velocity” u_z^* and the “critical updraft height” ΔZ^* . Only if both criteria are met, liquid-droplet activation is possible. Employing the quasi-steady model of Korolev and Mazin [2003], in Fig. 2.4 the critical velocity is shown in dependence of the ratio between ice-water content (IWC) and the total condensed-water content (CWC). The CWC is the sum of

IWC and liquid-water content (LWC) and, consequently, holds all water of an air parcel which is condensed into either liquid cloud droplets or ice crystals:

$$\text{CWC} = \text{IWC} + \text{LWC}. \quad (2.6)$$

It is visible from Fig. 2.4 that for a relatively high IWC/CWC ratio of 0.1 an updraft velocity of only 0.1 m s^{-1} is large enough to activate liquid water droplets and maintain the liquid phase of the cloud. It is shown in Chapter 6 that such vertical motions are common in layered clouds. From Fig. 2.4, it can be seen that for the same IWC/CWC ratio the critical velocity increases with the number of ice crystals present. Single ice crystals that form in a supercooled liquid environment grow very fast and therefore deposit quickly from the – still predominantly liquid – cloud layer. As deposition is not even included in the model of Korolev and Mazin [2003], it means that significant ice formation is necessary before a turbulent mixed-phase cloud can glaciate completely. Indeed, particle sedimentation itself is a stabilizing factor, because it removes ice nuclei and water-vapor-consuming ice crystals.

All calculations so far assumed linear up- or downdraft motion. In reality, turbulent motion dominates the motion of particles in a cloud layer. In such a turbulent environment close to saturation over liquid water “pockets” of alternating super- and subsaturation form (see Fig. 2.5). It was shown in Korolev and Field [2008] that the resulting water and ice patterns within the cloud layer are similar to those of an air parcel oscillating harmonically. Hill et al. [2013] reproduced the phenomenon directly in a simulation.

Nevertheless, even the rough theoretical calculation presented here show that a mea-

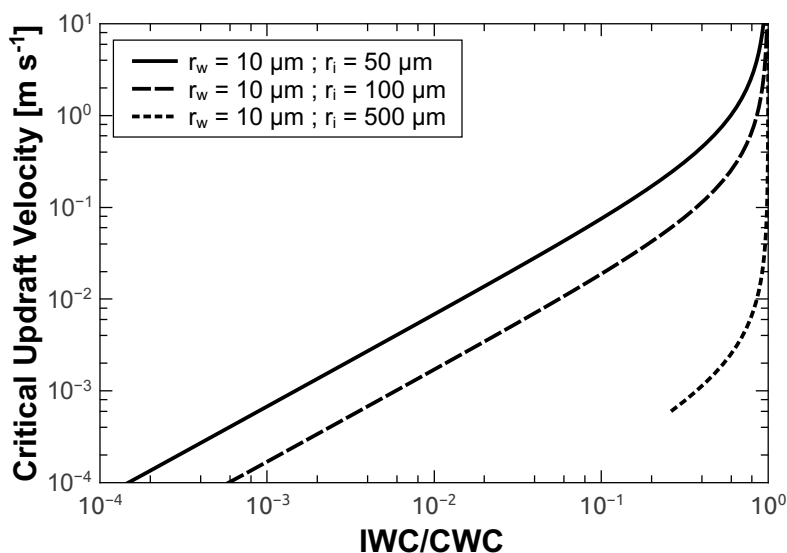


Figure 2.4: Critical updraft velocity u_z^* for the simultaneous growth of ice crystals and liquid water droplets in dependence of the IWC/CWC ratio.

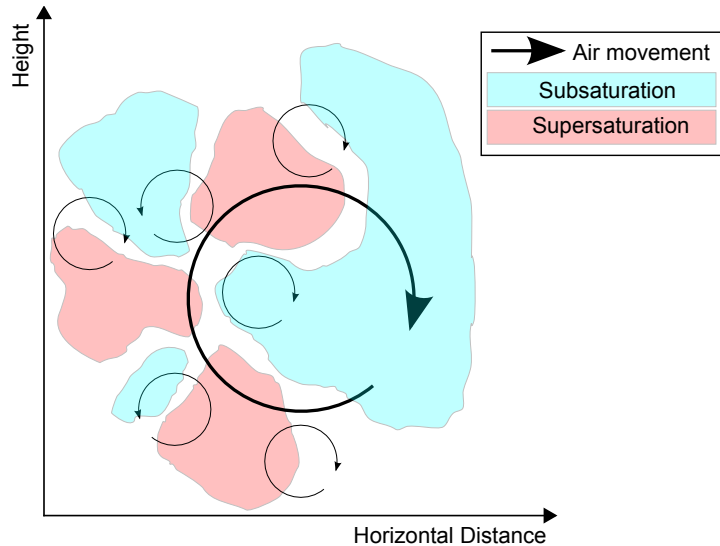


Figure 2.5: In a turbulent environment large eddies break down into smaller ones creating a distribution of super- and subsaturated regions inside the turbulent cloud layer.

surement uncertainty considerably lower than 1 m s^{-1} is required to capture the vertical air motion at cloud base. The temporal resolution of the measurements has to be high enough to record the breakdown of the turbulent eddies. At the same time, the measurements have to resolve IWC/CWC ratios lower than 10^{-3} . Therefore, in Chapters 3, 4 and 6, the ability of lidars and radars to measure and quantify IWC and LWC is explored. In Chapter 5 the velocity resolution of the employed lidar and radar systems is analyzed, together with their ability to probe turbulence.

2.4 Connecting observations with simulations

The influence of turbulence on mixed-phase layered clouds has been subject of many theoretical [Korolev and Mazin, 2003; Field et al., 2013] and modeling studies [Hill et al., 2013] recently. In the framework of the UDINE project own simulations have been carried out at TROPOS by Martin Simmel [Simmel et al., 2014]. In Fig. 2.6 an example case study of a mixed-phase layered cloud is depicted. It assumes different vertical-velocity distributions in a humid layer about 4000 m above the surface. All other environmental constraints like temperature, humidity and aerosol load are based on the measurement of a mixed-phase cloud layer over Leipzig on 17 September 2011.

It can be seen from Fig. 2.6 that the vertical velocity distribution has decisive impact on the evolution of the cloud layer. Stronger vertical motions lead to the condensation of more water vapor and thus enhance ice formation and deposition. The resulting IWC in the virga below cloud top layer is on the order of $10^{-8} \text{ kg m}^{-3}$ and varies by a factor of 2 for a vertical-velocity standard distribution σ_v between 0.3 and 0.7 m s^{-1} . Ice production is so weak that loss of water and IN scavenging due to ice deposition has no visible effect on the time scale of the simulation. Given sustained turbulent motions, such a cloud

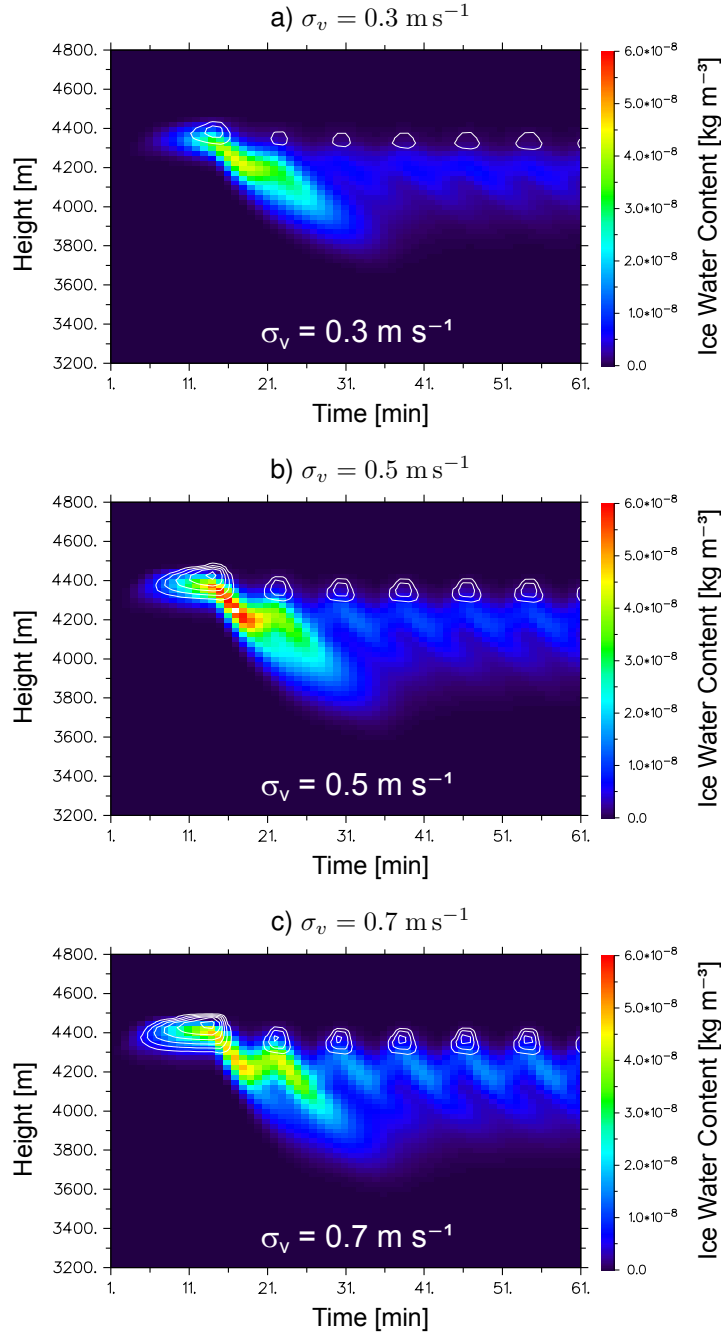


Figure 2.6: Simulation of heterogeneous ice formation in a liquid layer for different vertical-velocity standard deviations σ_v [Martin Simmel, personal communication]. The measured standard deviation of vertical velocity at cloud base was $\sigma_v = 0.44 \text{ m s}^{-1}$. An initial updraft is used to generate cloud droplets in the air parcel, then it is oscillating harmonically. A random vertical-velocity pattern is added with the amplitude of the harmonic oscillation. A similar approach was chosen by Korolev and Field [2008]. The increased ice production in the initial updraft at (b) compared with (a) and (c) may be an artifact of the simulation. 20 min after start of the simulation, the amount of ice production increases with increasing σ_v from $1 \times 10^{-8} \text{ kg m}^{-3}$ (a) to $2.5 \times 10^{-8} \text{ kg m}^{-3}$ (c). Contour lines of LWC have a constant spacing of $3 \times 10^{-5} \text{ kg m}^{-3}$ and also start at this value. A more detailed evaluation of the real cloud case is carried out in Section 6.2.

layer will be stable over hours.

2.5 Arising questions

The theoretical considerations discussed in this chapter ultimately lead to different questions to be answered:

- What ratios between liquid water and ice can be observed within mixed-phase layered clouds with respect to mass and number concentration?
- What are the statistical properties of the vertical air motions within these clouds?
- What is the critical ratio between ice and water at which the ice dominates the microphysics within the mixed-phase cloud layer and the cloud will glaciate completely?

These questions cannot be answered by measurements alone, but also require cloud modeling and laboratory work. An experiment carried out in nature can provide modelers both input parameters and values to test the results. In Section 2.4 measured vertical-wind velocity was used as input and the IWC as a reference. Such end-to-end simulations can only succeed, if the input and the reference data are quality-assured and treated to be free of artifacts. In this work, ways towards precise measurements of vertical-wind velocity at cloud base will be shown in Chapter 5, involving Doppler lidar, cloud radar and wind profiler systems. The main benefit of this combination is the simultaneous measurement at different target sizes ranging from aerosol particles to rain droplets. The synergy between the single measurement systems can be very high, but data of all instruments have first to be brought down to a common time and height grid. Chapter 4 describes such a combined data processing. Especially the cloud radar delivers much more information than only velocity measurements. From its signals one can, e.g., obtain the IWC (see Chapter 6). In future, it may be even possible to derive the ice crystal number concentrations (see Chapter 7). Bringing all these quantitative measurements together one will be able to approach the questions above on a solid basis.

3 Lidar and radar synergy. Part I: Signal strength

Combining lidars and radars is useful but also very challenging because of their great technical differences. The most prominent example may be that the signal sensitivity for a liquid water droplet with diameter D is proportional to D^2 for lidar and D^6 for radar. Such differences must be kept in mind during the evaluation of combined measurements. In this chapter, differences and similarities of both remote-sensing systems are explored on a theoretical basis [Wandinger, 2004; Peters and G6rsdorf, 2010]. It is shown in Section 3.1, what assumptions are necessary to describe the measurements of lidars and radars with a common equation. The ability of lidar and radar to probe the properties of particles in mixed-phase cloud layers is examined in Section 3.2. In Section 3.2.4 the terminal fall velocity of cloud droplets and ice crystals is analyzed to support the interpretation of Doppler lidar and cloud radar measurements.

From the physical viewpoint, lidars and radars are very similar. Both emit pulses of electromagnetic radiation through an aperture and detect the fraction of radiation scattered back. For the TROPOS Multiwavelength Atmospheric Raman Lidar for Temperature, Humidity, and Aerosol Profiling (MARTHA) [Mattis et al., 2004] and the MIRA-35 cloud radar of LACROS [Bauer-Pfundstein and G6rsdorf, 2007] surprising similarities prevail for the emitter/receiver aperture sizes ($d_r \approx 1$ m) and the average emitted power ($\overline{P} \approx 30$ W). The main difference between the two systems is the wavelength of the emitted radiation, which is 355 to 1064 nm for the lidar and 8.5 mm for the radar. To find a common description for lidar and radar, monochromatic systems operating at wavelengths $\lambda_{L/R}$ (in the following, indices L and R stand for “lidar” and “radar”, respectively) are assumed.

3.1 Description of lidar and radar backscattering

3.1.1 Generalized equation for active remote sensing

Electromagnetic radiation is diffracted by any aperture it is sent through [Goodman, 2005b]. The resulting diffraction pattern is characteristic for both emission and reception of electromagnetic radiation through that aperture. Close to the aperture, in the so-called Fresnel zone, this pattern has range and angular dependence. More far away, in the so-called Fraunhofer zone, only angular dependence remains. The distance from the aperture to the end of the Fresnel zone can be estimated by $r_{\text{FZ}} = 2d_r^2/\lambda$, where d_r is the diameter of the emitter aperture. r_{FZ} is about 250 m for the MIRA-35 cloud radar and

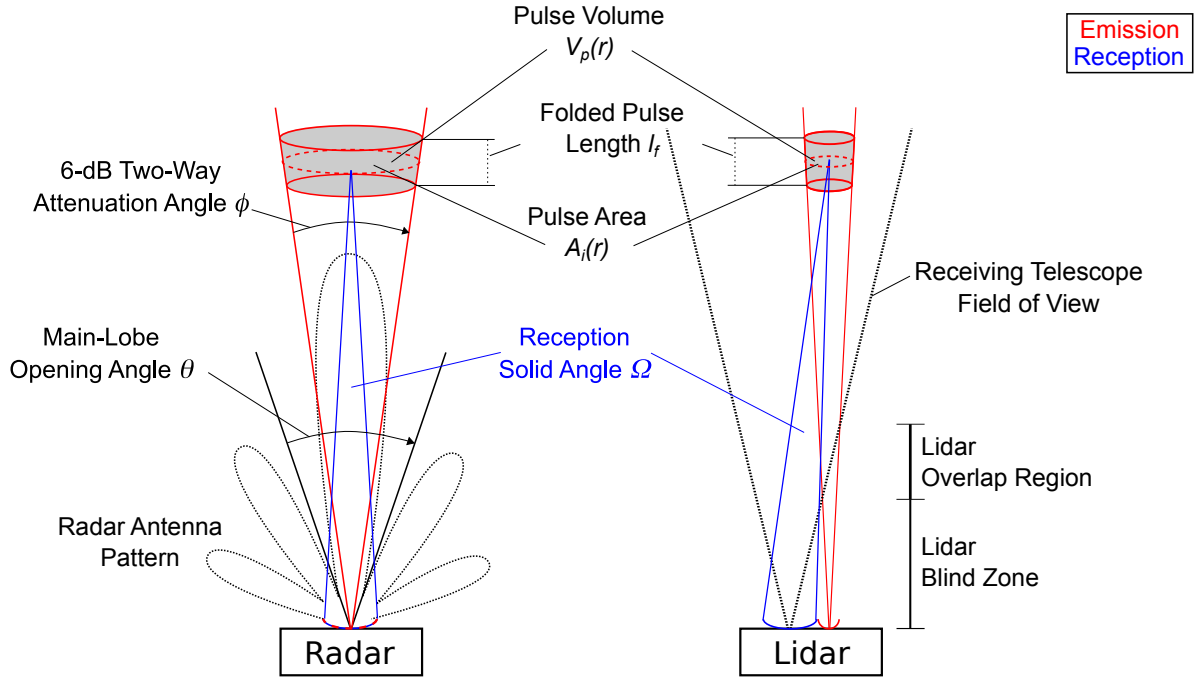


Figure 3.1: Comparison of the characteristics of radar (left) and lidar (right). The angular-dependent radar antenna pattern is depicted schematically. At $\phi/2$ from emission direction, the sensitivity of the antenna has dropped by 3 dB. Because the same antenna is used for emission and reception, the total dampening is 6 dB and ϕ is defined as the opening angle of pulse propagation. The first diffraction minimum is at $\theta/2$ from emission direction. θ then contains the whole main lobe of the emitted radiation. In this view, a lidar with separated biaxial emitter and receiver telescope is depicted (e.g., PollyXT) leading to a a blind zone and a region of incomplete overlap.

more than 300 km for the MARTHA lidar. For a circular aperture, the angular width of the main lobe (inside the first diffraction minimum) is $\theta = 2.44\lambda/d_r$. Within this main lobe, about 84% of the diffracted power are contained. θ is approximately 1.22° for the cloud radar and $7.6 \times 10^{-5}^\circ$ for the MARTHA lidar. Fig. 3.1 illustrates the different propagation characteristics for lidars and radars.

For lidars, the receiving telescope can be designed in such a way that its field of view is considerably bigger than the divergence of the propagating laser pulse. If this is the case, any angular dependence of the receiver can be neglected, as long as the laser pulse has left the overlap zone (see Fig. 3.1). For monostatic radars like the MIRA-35, radiation is always emitted into and received from the half-space. The same antenna is used for emission and reception, so the field of view of the antenna matches its emission characteristics. At $\phi/2$ from emission direction, the received signal has decreased from 0 dB (beam center) to -6 dB. For simplicity, it is assumed that the radar only emits radiation within the opening angle ϕ [Peters and G6rsdorf, 2010]. The volume of one radar pulse is then defined as

$$V_{p,R}(r) \stackrel{!}{=} \frac{l\pi(\phi r)^2}{4}, \quad (3.1)$$

with pulse length $l = c_l \tau$ (c_l the velocity of light and τ the temporal pulse length). The so defined pulse volume has a nearly cylindrical shape and is proportional to r^2 . For the MIRA-35 cloud radar of LACROS, ϕ is about 0.5° which corresponds to a pulse diameter of approximately 10 m in a range of 1 km. The emitted power inside this (theoretical) pulse volume has to be determined experimentally. This calibration is one major issue of cloud radar research [Hogan et al., 2003]. It has to be kept in mind that the defined signal drop to -6 dB at $\phi/2$ is only a factor of about 0.25. Hence, in an atmospheric scene with high spatial variabilities, the signal will be mixed with signals from adjacent scatterers from outside the defined pulse volume $V_{p,R}(r)$. This problem is especially relevant for AC clouds. In this case, the radar can only deliver averaged cloud properties. The signal of a lidar is received from a much more restricted volume.

With the assumptions made above, it is possible to formulate a common equation for the signal received by lidar and radar. The power $P_c(r)$ collected by a receiver with aperture (telescope mirror) area A_t from an atmospheric volume at range r scattering back electromagnetic radiation of power P_Ω into the solid angle Ω is

$$P_c(r) = \int_{\Omega(r)} P_\Omega(r) T(r) d\Omega. \quad (3.2)$$

r is the range between the aperture and the illuminated volume, Ω is the solid angle under which the aperture appears from distance r and $T(r)$ is the transmission term which describes the range-dependent signal extinction between the emitter and distance r . In a remote-sensing application, $P_\Omega(r)$ is proportional to the intensity I_i of the radiation incident on the observed volume and the total scattering cross section S_Ω of the observed volume. Hence, the expression of $P_c(r)$ further expands to

$$P_c(r) = \int_{\Omega(r)} S_\Omega(r) I_i(r) T(r) d\Omega = \int_{\Omega(r)} S_\Omega(r) \frac{P_0}{A_i(r)} T^2(r) d\Omega. \quad (3.3)$$

P_0 is the power of the emitted pulse and $A_i(r)$ is the mean cross section of the illuminated volume (see Fig. 3.1). The scattering properties within the illuminated volume $V_i(r)$ can be expressed as

$$S_\Omega = B(r) V_i(r), \quad (3.4)$$

if a backscattering geometry is assumed (see Fig. 3.1). $B(r)$ describes, how the objects within V_i scatter back radiation into the solid angle Ω . If the aperture size A_t is small against r^2 , Eq. (3.3) becomes

$$P_c(r) = P_0 \frac{B(r) V_i(r) T^2(r) A_t}{A_i(r) r^2}. \quad (3.5)$$

The receiver may actually not be able to completely see the illuminated volume V_i . This can be the case, e.g., in the overlap zone of the lidar, where the laser pulse is still outside the field of view of the telescope (Fig. 3.1). Thus, the illuminated volume $V_i(r)$

is replaced by $A_i l_f$ multiplied by a function $O(r)$:

$$P_c(r) = P_0 O(r) \frac{B(r) A_i(r) l_f T^2(r) A_t}{A_i(r) r^2}. \quad (3.6)$$

Here $l_f = c_l \tau / 2$ is the folded pulse length. In this way, Eq. (3.6) reduces to the generalized active-remote-sensing equation

$$P_c(r) = P_0 l_f A_t O(r) B(r) T^2(r) \frac{1}{r^2}. \quad (3.7)$$

The meaning of the single terms is explained in the next section. Equation (3.7) describes the power that reaches the receiving telescope. To derive the power that actually reaches the receiver, the efficiency of the receiver unit has to be taken into account. It is usually collected in a system constant $C_{R,L}$, including also P_0 , l_f and A_t and determined experimentally.

3.1.2 Detailed description of all terms

3.1.2.1 Pulse power P_0 and effective pulse length l_p

For both lidar and radar, a temporally rectangular pulse is assumed with the mean energy P_0 . The folded length of the pulses is $l_f = c_l \tau / 2$, which is half of the physical pulse length due to folding of the pulse in backscatter observations.

3.1.2.2 Receiver aperture A_t

The aperture area of the lidar telescope corresponds to the effective aperture of the radar antenna. The latter is defined as $A_e = \lambda_R^2 / (4\phi^2)$ and has the unit m^2 . For the MIRA-35 cloud radar of LACROS $A_e = 0.23 \text{ m}^2$. This value compares to the MARTHA lidar with 0.5 m^2 and the PollyXT lidar with 0.07 m^2 telescope area.

3.1.2.3 Overlap function $O(r)$

The receiving telescope of a lidar does usually not completely see an emitted laser pulse up to a certain height. The overlap function $O(r)$ describes the resulting influence on the received signal. Depending on the system, it approaches 1 within the first few hundred (PollyXT) or thousand meters (MARTHA). Doppler lidars like WiLi always have a perfect geometric overlap, because the telescope is transmitter and receiver at once (transceiver). Regardless, the introduction of a function like $O(r)$ makes sense for WiLi, because in the lowest 500 m the receiver of the atmospheric signal shows non-linear effects by overload from straylight during pulse emission and defocus of the atmospheric signal.

The radar receiver/emitter system shows similar behavior. Close to the emitter, the signal is received at full strength, but may not be useful for atmospheric measurements. $O(r)$ cannot be described easily analytically but it approaches 1 at the end of the Fresnel

zone of the radar. In a mathematical sense, $O(r)$ can also be useful to remind that Eq. (3.7) is not valid for $r \rightarrow 0$, due to the assumption of small solid angles.

3.1.2.4 Volume backscatter properties $B(r)$

$B(r)$ holds the backscatter properties of the particles within the pulse volume and is the main measurement goal. In general, it holds the volume-averaged backscatter properties, i.e.,

$$B(r) = \sum_n \int_0^\infty N_n(r, D) \left. \frac{\partial s_n(r, D)}{\partial \Omega} \right|_{180^\circ} dD \stackrel{!}{=} \sum_n \int_0^\infty N_n(r, D) s_{n,180^\circ}(r, D) dD, \quad (3.8)$$

with the number concentration $N_n(r)$ of the n -th particle type in the scattering volume and the particles' differential backscattering cross section $s_{n,180^\circ}$.

The ice and water particles observed in the context of this work are in the size range of 10 μm to 1 mm. The millimeter waves of the radar will, therefore, experience Rayleigh scattering and

$$s_{180^\circ}^R = \frac{1}{4\pi} \frac{\pi^5}{\lambda^4} K_{w,i}^2 D^6. \quad (3.9)$$

$K_{w,i}$ is the material-dependent dielectric factor at 35 GHz, which is $K_w^2 = 0.93$ for liquid water and $K_i^2 = 0.174$ for ice. The volume-equivalent diameter D is connected with the mass m_p of a particle:

$$D = \left(\frac{6}{\pi \rho_{w,i}} m_p \right)^{1/3}, \quad (3.10)$$

where $\rho_{w,i}$ is the density of liquid water or ice. D matches the geometric diameter for spherical particles. A mixture of liquid water droplets and one type of ice crystals in the scattering volume leads to

$$\begin{aligned} B_R(r) = \frac{\eta(r)}{4\pi} &= \frac{1}{4\pi} \frac{\pi^5}{\lambda_R^4} \left(K_w^2 \int_0^\infty N_w(r, D) D^6 dD + K_i^2 \int_0^\infty N_i(r, D) D^6 dD \right) \\ &= \frac{1}{4\pi} \frac{\pi^5}{\lambda_R^4} Z(r), \end{aligned} \quad (3.11)$$

with the radar scattering cross section $\eta(r)$ and the particle number concentrations $N_{w,i}$ for liquid water (w) and ice particles (i). $Z(r)$ is the radar reflectivity factor

$$Z(r) = K_w^2 \int_0^\infty N_w(r, D) D^6 dD + K_i^2 \int_0^\infty N_i(r, D) D^6 dD. \quad (3.12)$$

The physical unit of Z is $1 \text{ m}^6 \text{ m}^{-3}$ in this notation. Z is usually normalized by the signal $Z_0 = 0.93 \times 0.001^6 \text{ m}^6 \text{ m}^{-3}$, which is the radar reflectivity factor of a volume filled with droplets with $D = 1 \text{ mm}$ and $N = 1 \text{ m}^{-3}$. Z is usually depicted on a decibel scale as $Z_{\text{dBZ}} = 10 \log(Z/Z_0)$. The corresponding unit is denoted dBZ.

The backscatter signals for lidars can be calculated easily in the limits of geometrical

optics. In this case,

$$s_{180^\circ}^L = \frac{2A_p}{L}. \quad (3.13)$$

A_p is the particle area projected to the fall direction, L is the extinction-to-backscatter ratio (lidar ratio). In the visible wavelength range, the lidar ratio $L_w \approx 18$ sr for liquid droplets and $L_i = 20\text{--}30$ sr for ice particles. The lidar ratio of ice crystals can be determined with numerical methods [e.g., Macke et al., 1996]. Taking into account Eq. (3.13), the backscatter term for lidar in Eq. (3.7) becomes

$$B_L(r) = \beta(r) = \sum_n \int_0^\infty N_n(r, D) \frac{2A_{p,n}(D)}{L_n} dD. \quad (3.14)$$

β is called the volume backscatter coefficient. For lidars in the optical wavelength range, molecular scattering adds to $B_L(r)$, but this additional scattering can be removed [Ansmann et al., 1990]. For both lidar and radar, the function $B(r)$ can depend on more characteristic parameters. For Doppler lidars and radars, e.g., the particle velocity v can be included and particle number concentration $N(r, v)$ can be defined. The received power $P_c(r)$ then becomes a two-dimensional function $P_c(r, v)$, which is represented in height-resolved Doppler spectra. The treatment of such spectra is discussed in Chapter 5, cloud-radar spectra are subject of analysis in Chapter 7.

3.1.2.5 Transmission term $T(r)$

The transmission term $T(r)$ defines the extinction of electromagnetic radiation by absorption and scattering. For monochromatic lidars and radars, the extinction on the way to the target is the same as on the way back. Thus, the Lambert-Beer law describes the transmission as

$$T(r) = \exp\left(-2 \int_0^r \alpha(r') dr'\right), \quad (3.15)$$

with α being the electromagnetic extinction coefficient at a certain range. For lidars, the extinction coefficient is connected with the backscatter coefficient via the extinction-to-backscatter ratio $L = \alpha/\beta$ (lidar ratio). Assuming a homogeneous particle population, the extinction can be estimated for known particle types. With Raman lidars like MARTHA this quantity can be derived together with the backscatter coefficient. Standard methods to derive $\beta(r)$ and $\alpha(r)$ from lidar measurements are given by Klett [1981] (elastic backscatter lidar) and Ansmann et al. [1990] (Raman lidar).

In the layered clouds, which are treated in this work, particle extinction is very low for a 35-GHz radar. At this high radar frequency also gas attenuation in the free atmosphere can play a role. This attenuation depends, e.g., on the water vapor path between the radar and the observation volume and is usually smaller than 1 dB in the whole troposphere for observations at Leipzig. Radar attenuation is therefore not further considered in the scope of this work, if radar data is evaluated manually. All values derived with the help of Cloudnet [Illingworth et al., 2007] (introduced in the next chapter) are automatically corrected for gas attenuation.

3.2 Detection of spherical and non-spherical particles with lidar and radar

Cloud droplets and ice crystals can both be detected with lidar and radar. For studies of heterogeneous freezing in the atmosphere, it is important to know the detection limits of the different systems. The main difference between lidar and radar is the dependence of the backscatter term $B_{L,R}$ in Eq. (3.7) on the particle properties. For lidar, mostly geometric scattering is involved, so that the particle backscatter coefficient is proportional to A_p . The radar operates in the Rayleigh scattering regime and the radar reflectivity factors of liquid droplets or ice crystals are proportional to D^6 or to the square of particle mass m_p^2 .

3.2.1 Linear depolarization ratio

Equation (3.12) shows that the meaning of Z is ambiguous, if no additional information about phase, shape and spectral distribution of the scattering particles is available. Pure detection of particles is, therefore, not sufficient. The polarization state of the electromagnetic radiation received from the target volume can be used to decide between (spherical) water droplets and non-spherical targets like ice crystals. The latter induce a depolarization on both lidar and radar signals. To measure this polarized radiation, the backscattered signal is received in two channels simultaneously, with perpendicular polarization sensitivity. One way to calculate the linear depolarization ratio δ is to divide the signals received in the perpendicular and the parallel channel and to derive the depolarization ratio $\delta = P_{\perp}/P_{\parallel}$. δ can be about 0.5 for lidars, when observing ice crystals [Mishchenko and Sassen, 1998; Sassen, 2004]. In contrast, δ rarely exceeds 0.01 or $10 \log(0.01) \text{ dB} = -20 \text{ dB}$ for 35-GHz radars, where this measurement quantity is usually designated LDR (for linear depolarization ratio) and measured in decibel [Reinking et al., 1997; Matrosov et al., 2012]. The identification of liquid water and ice particles in layered clouds with the help of the depolarization ratio is further treated in Chapter 4.

3.2.2 Area and mass parameterizations

Area A_p and mass m_p of ice and water particles have to be known in order to estimate their backscatter properties. Especially for ice crystals this estimation is difficult, because their geometry is complex and changes significantly during growth. Mandelbrot [1982] showed that the shapes of some naturally formed objects, like ice crystals, can be described by fractal geometry over large size ranges. Mitchell [1996] used this idea to describe area A_p and mass m_p of ice particles by fractal power-laws, depending on the ice particles' maximum diameter D_m (the diameter encircling the area projected to flow

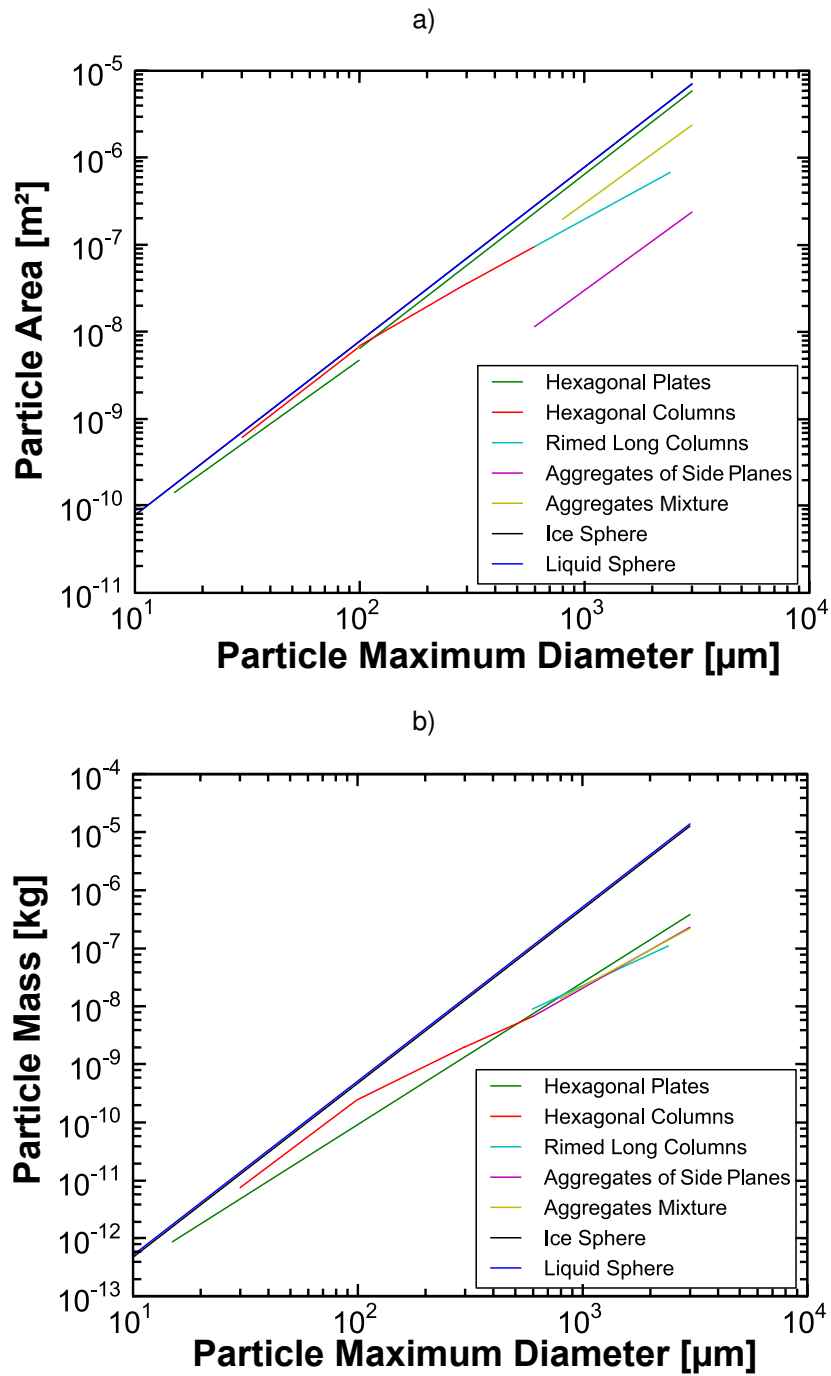


Figure 3.2: Selected parameterizations of particle area A_p (a) and particle mass m_p (b) from Mitchell [1996], depending only on the particles' maximum diameter D_m . All values are shown in their ranges of validity. Hexagonal plates are parameterized unsteadily at $D_m = 100 \mu\text{m}$. For hexagonal columns the continuation is steady at this diameter, but bends sharply.

direction) in the form

$$A_p(D_m) = aD_m^b, \quad (3.16)$$

$$m_p(D_m) = cD_m^d. \quad (3.17)$$

The coefficients a, b, c and d can be determined experimentally. Mitchell [1996] lists their numerical values and ranges of validity for a broad spectrum of ice crystal species. The maximum diameter D_m does not have a direct influence on the calculation of signal strength. It is only a characteristic length to connect the area and mass parameterizations. Figure 3.2 shows some parameterizations from Mitchell [1996] for particle species that are used in this work. For hexagonal columns $b = 2.0 \dots 1.4$ (from small to large particles) and $c = 2.9 \dots 1.74$. For aggregates of side planes $b = 1.88$ and $c = 2.2$.

3.2.3 Particle detection thresholds

For a simplified monodisperse size distribution of spherical particles, the critical particle number concentration can be calculated, which is needed to surpass the detection limits of lidar or radar. The minimum detectable backscatter signals β_{\min} and η_{\min} are divided by the single-particle returns from Eqs. (3.9) and (3.13), so that the critical number concentrations for radar and lidar can be defined as

$$N_{\text{crit}}^L = \frac{\beta_{\min}}{s_{180^\circ}^L} = \frac{2L\beta_{\min}}{A_p} \quad (3.18)$$

and

$$N_{\text{crit}}^R = \frac{\eta_{\min}}{4\pi s_{180^\circ}^R} = \frac{(\pi\rho_{w,i})^2 Z_{\min}}{18K_{w,i}^2 m_p^2}. \quad (3.19)$$

The particle diameter D_{es} , for which lidar and radar are equally sensitive, can be derived by demanding $N_{\text{crit}}^R \stackrel{!}{=} N_{\text{crit}}^L$ and inserting Eqs. (3.16) and (3.17), so that

$$D_{\text{es}} = \left(\frac{a(\pi\rho_{w,i})^2 Z_{\min}}{18c^2 K_{w,i}^2 L_{w,i} \beta_{\min}} \right)^{\frac{1}{2d-b}}. \quad (3.20)$$

For liquid water droplets $a = \pi/4$, $b = 2$, $c = \rho_w \pi/6$ and $d = 3$ and Eq. (3.20) reduces to

$$D_{\text{es}} = \left(\frac{\pi Z_{\min}}{2K_w^2 L_w \beta_{\min}} \right)^{\frac{1}{4}}. \quad (3.21)$$

Below D_{es} , the lidar can detect particles at lower number concentrations than the radar, above vice versa. Figure 3.3 presents the trend of $N_{\text{crit}}(D_m)$ over the range $1 \mu\text{m} < D_m < 3 \text{mm}$ for these minimum detectable signals. It shows that lidar and radar complement each other in the size range of very small and very large particles. From Fig. 3.3 it becomes obvious that the MIRA-35 cloud radar is in principle capable of detecting AC clouds, but it will largely miss activation of small droplets at the cloud base where $D \approx 2..10 \mu\text{m}$ (D and D_m are equivalent for small cloud droplets). For this purpose, the

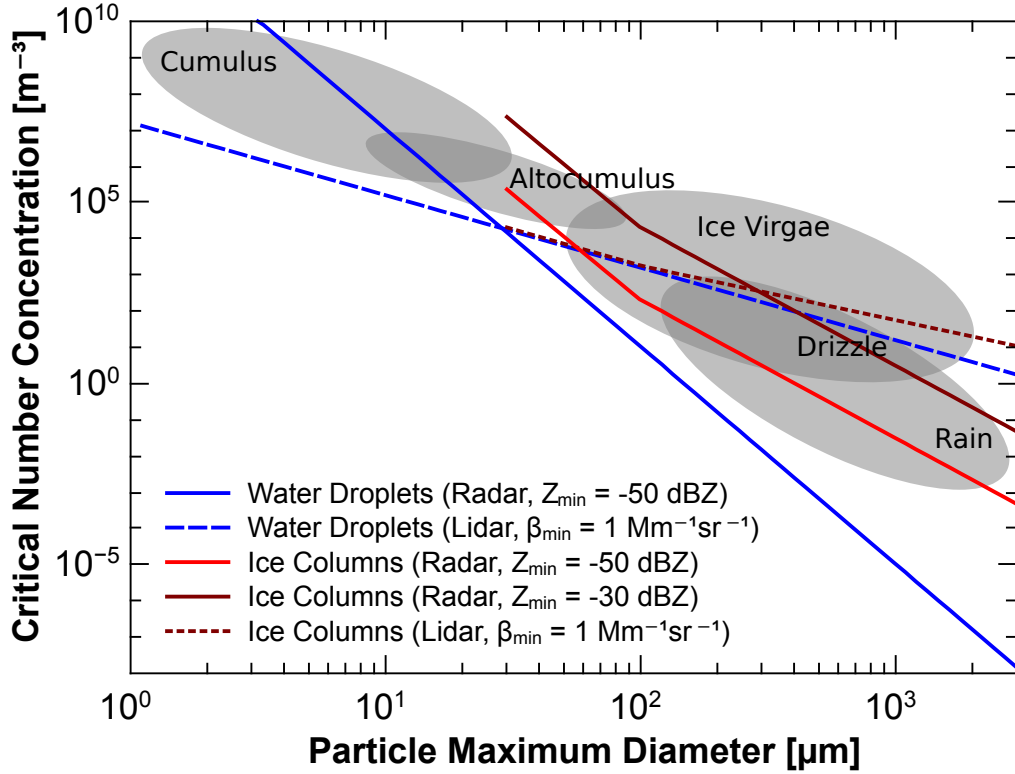


Figure 3.3: The critical particle number concentration N_{crit} is shown for radar (solid lines) and lidar (dashed lines). Any monodisperse particle concentration lower than N_{crit} does not produce a detectable signal for the corresponding system. Assumptions on minimum signals were $Z_{\text{min}} = -50$ dBZ and $\beta_{\text{min}} = 1 \text{ Mm}^{-1} \text{ sr}^{-1}$. Lidar ratios were assumed to be $L_w = 18$ sr (water droplets) and $L_i = 25$ sr (ice crystals). Therefore, L_i is at least 20% accurate for all particles. Blue curves indicate water droplets. The line for hexagonal columns (bright red curves) is assembled from different parameterizations in the appropriate size ranges from $30 \mu\text{m}$ to $600 \mu\text{m}$. Above, the parameters of rimed long columns are applied. It is visible that for small maximum diameters, the curve of hexagonal columns approaches the theoretical curve of spherical particles (solid blue line). In the background, expected ranges of droplet and ice-particle number concentrations in clouds, virgae and rain are shown.

lidar is better suited. On the other hand, the radar can detect columnar ice particles with $D_m \approx 300 \mu\text{m}$, if their number concentration is only 1 m^{-3} . At the same maximum diameter, the critical number concentration for lidars is about two orders of magnitude larger.

In the mid-troposphere, the MIRA-35 cloud radar is designed to detect $Z_{\text{min}} \approx -50$ dBZ. In Chapter 6 the minimum detectable backscatter signal of PollyXT and MARTHA lidars is statistically determined to be $\beta_{\text{min}} = 1 \text{ Mm}^{-1} \text{ sr}^{-1}$ for an integration time of 30 s. These values yield $D_{\text{es}} = 31 \mu\text{m}$ for liquid water droplets. In the case of columnar ice particles and the same signal thresholds $D_{\text{es}} = 57 \mu\text{m}$. It is visible from Fig. 3.3 that for small D_m the curves of hexagonal columns run parallel to those of spherical water droplets.

Pure particle detection alone is not the only goal of remote sensing, the particle type

is also of great interest. Depolarization can help to unambiguously decide between liquid water and ice particles. However, particle classification by depolarization needs higher signal strengths than particle detection alone. If $Z_{\min} = -50$ dBZ is assumed and an observed volume is filled with ice crystals, which induce a depolarization $\delta \approx -20$ dB, the signal received from this volume has to be larger than -30 dBZ, until a depolarization can be detected. The dark red curves in Fig. 3.3 show the critical number concentrations, obtained for the signal thresholds $Z_{\min} = -30$ dBZ and $\beta_{\min} = 1$ Mm⁻¹ sr⁻¹, shifting D_{es} to about 338 μm . Lidars measure the depolarization more easily, because with $\delta \approx 0.5$ the signal received in the depolarization channel is on the same order of magnitude as the total signal. In Section 4.5 of the next chapter, combined particle classification by lidar and radar is treated in more detail.

3.2.4 Terminal fall velocities

The terminal fall velocity of ice and water particles has to be taken into account carefully, when dealing with vertical-velocity measurements from Doppler lidars and cloud radars. On the one hand, falling particles can disturb and offset measurements. On the other hand, the terminal fall velocity yields information about particle size and shape. The latter will be exploited in Chapter 7 to derive number concentrations of falling particles from cloud radar spectra. In the following, vertical velocities derived from moving cloud particles are denoted v , in contrast to the vertical air velocity u_z introduced before.

According to Heymsfield and Westbrook [2010] the calculation of a particle's terminal fall velocity is a three-step process. First, the so-called Best number X^* is calculated, which contains the basic information about the particle (mass m_p and area ratio $A_r = A_p/(\frac{\pi}{4}D_m^2)$) and the surrounding air (density ρ_{air} , dynamic viscosity of air η_{air} , acceleration of gravity g):

$$X^* = \frac{8m_p g \rho_{\text{air}}}{\pi \eta_{\text{air}} A_r^{(1-k)}}. \quad (3.22)$$

k is a dimensionless empiric parameter introduced to achieve better agreement with laboratory studies. Heymsfield and Westbrook [2010] found that the Reynolds numbers Re fit best the laboratory measurements, if $k = 0.5$ and

$$\text{Re} = \frac{\gamma_0^2}{4} \left[\left(1 + \frac{4\sqrt{X^*}}{\gamma_0^2 \sqrt{\gamma_1}} \right)^{0.5} - 1 \right]^2, \quad (3.23)$$

with $\gamma_0 = 8.0$ and $\gamma_1 = 0.35$. The terminal fall velocity is then computed by

$$v_t = \frac{\eta_{\text{air}} \text{Re}}{\rho_{\text{air}} D_m}. \quad (3.24)$$

In Fig. 3.4 the terminal fall velocities are calculated for different particle species, assuming pressure $p = 650$ hPa and temperature $T = 260$ K.

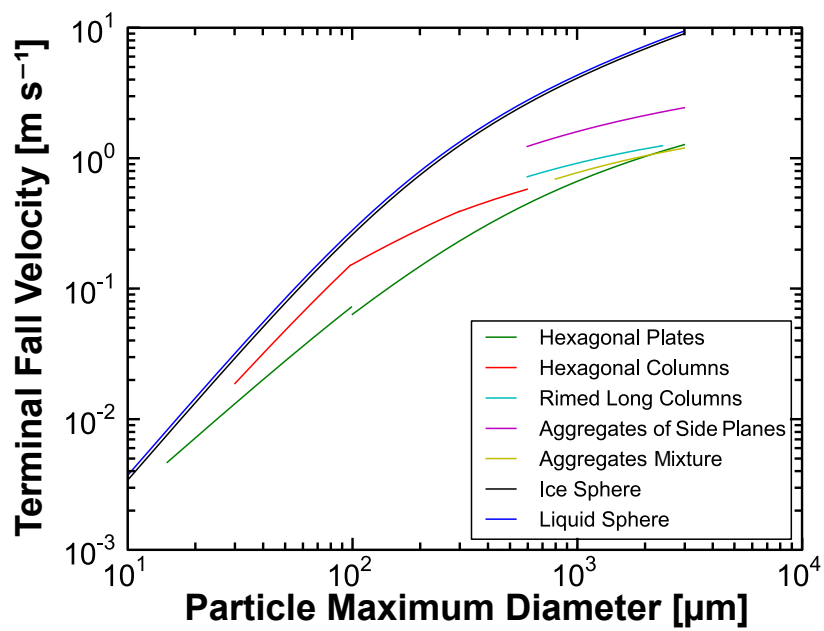


Figure 3.4: Terminal fall velocities of different particle species calculated with the method of Heymsfield and Westbrook [2010] for $T = 260$ K and $p = 650$ hPa. The gap in the curve for hexagonal plates originates from the unsteadiness in the area parameterization described in Fig. 3.2.

4 TROPOS remote-sensing facility for simultaneous profiling of aerosols, clouds and meteorological parameters

Investigation of cloud processes involves a huge variety of length scales [Bodenschatz et al., 2010], ranging from aerosol particles of some nanometer in diameter to cloud fields, hundreds of kilometers wide. This wide scale range poses a great challenge to remote-sensing methods, because the sensitivity of any instrument is restricted to a certain target size range. Only a combination of different measurement systems can map all facets of a cloud system. The Leipzig Aerosol and Cloud Remote Observations System (LACROS) is a set of remote-sensing and in-situ measurement systems of TROPOS, dedicated to the continuous observation of clouds and aerosols. The integration into observation networks like Cloudnet [Illingworth et al., 2007], EARLINET (European Aerosol Research Lidar NETwork) and AERONET (AErosol ROBotic NETwork) opens a great diversity of possible scientific applications. LACROS combines the strengths of lidar, radar and radiometer techniques and employs auxiliary systems like a meteorological ground station and an advanced all-sky imager. The span of observation wavelengths ranges from 355 nm (Raman lidar) to centimeters (cloud radar and microwave radiometer).

4.1 Instrument overview

A schematic overview about all instruments gathered around the TROPOS main building is given in Fig. 4.1. It has been one major goal of this work to bring together the measurements recorded by the different systems.

For active vertical profiling of the atmosphere different active remote-sensing instruments are employed:

- PollyXT Raman/polarization lidar,
- WiLi coherent Doppler wind lidar,
- MIRA-35 cloud radar,
- CHM 15kx ceilometer.

Those are the active remote sensing instruments of LACROS. The operational parameters of the main instruments are shown in Table 4.1. In Fig. 4.2 their capabilities for particle detection is highlighted.

Table 4.1: Properties of the main active remote-sensing instruments within LACROS.

Designation	WiLi	PollyXT	MIRA-35
System type	Coherent Doppler lidar	Raman/polarization lidar	Cloud radar
Wavelength	2022 nm	355, 532, 1064 nm	8.3 mm
Range gate length	75 m	60 m	30 m
Integration time	2 s	30 s	10 s
Receiver field of view	0.05 mrad	0.3 mrad	10 mrad
Pulse repetition rate	750 Hz	30 Hz	5000 Hz
Average emitted power	1.5 W	5 W	30 W

There are also several passive remote-sensing and in-situ instruments included in LACROS:

- HATPRO (Humidity And Temperature PROFiler) microwave and infrared radiometer,
- AERONET sun photometer,
- SAEMS (Spectral Aerosol Extinction Monitoring System) [Skupin et al., 2014],

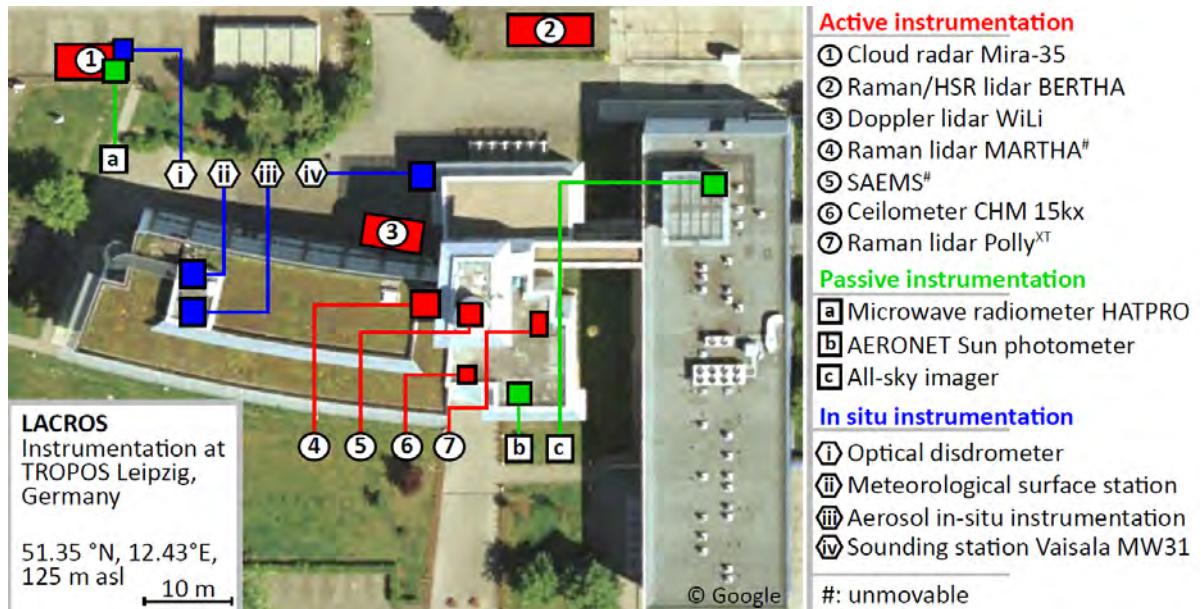


Figure 4.1: Overview of the LACROS instruments located at TROPOS, Leipzig.

- Photographic all-sky imager (vertically looking camera with 180° fisheye lens),
- Disdrometer for sensing size and fall speed of raindrops.

4.2 Measurement example

Figure 4.3 shows an example of a LACROS measurement on 30 May 2012 around 18:00 UTC. An AC cloud approached Leipzig from northwest with a horizontal wind speed of 16 m s^{-1} . The cloud-camera image is depicted together with the Cloudnet target classification product. The lidars show clear signals at about 3200 m height, while the radar only partially senses the liquid cloud top. However, the radar senses falling particles nearly everywhere in the virga, while the lidar only detects a short precipitation event at 18:30 UTC.

In Fig. 4.4, the vertical velocity measurement from a timespan of only about 2 min

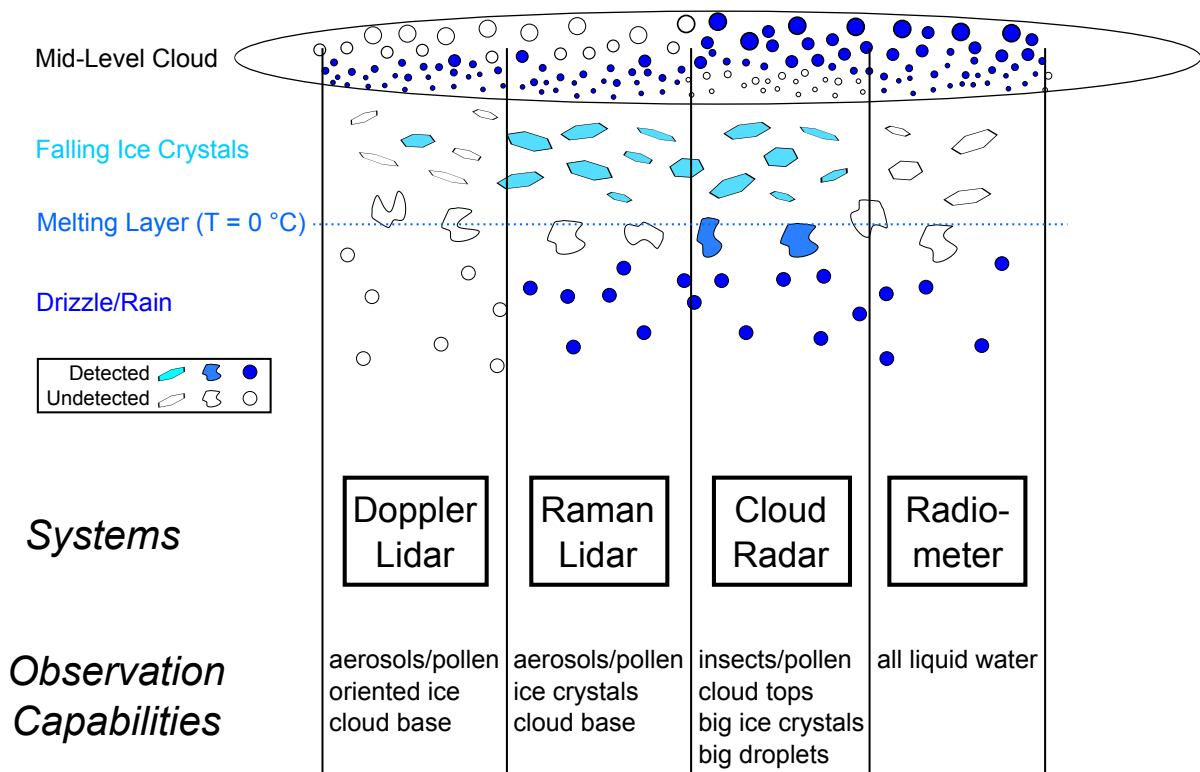


Figure 4.2: Comparison of the different particle detection capabilities of four LACROS systems. Detected particles are depicted in color, others are left blank. The lidars detect the particles at cloud base and some of the falling ice crystals. The PollyXT is powerful enough to detect all kinds of particles, the Doppler lidar has a much weaker emitter and only detects ice particles if they are oriented parallel to the ground. The cloud radar can detect the falling particles very well, but cannot detect the small, freshly activated particles at cloud base. The microwave radiometer gives an integral value of liquid water path and total atmospheric water vapor content. It is visible that the four systems complement each other so that all particles types are resolved.

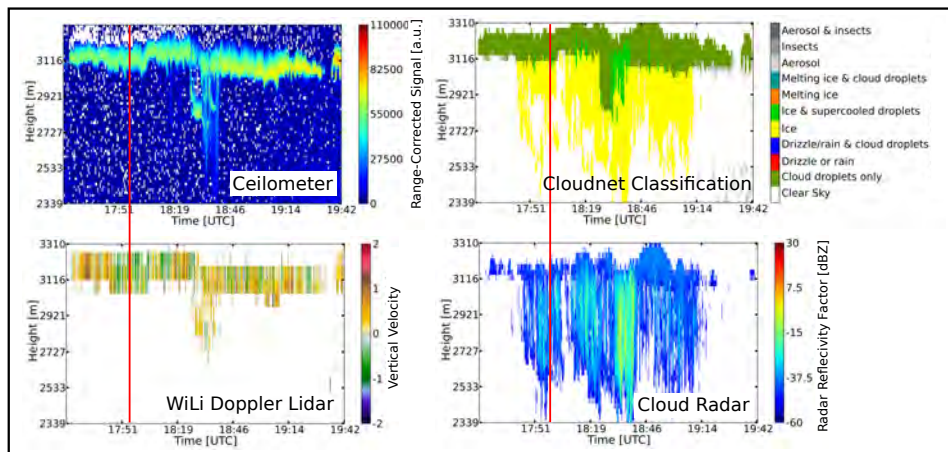
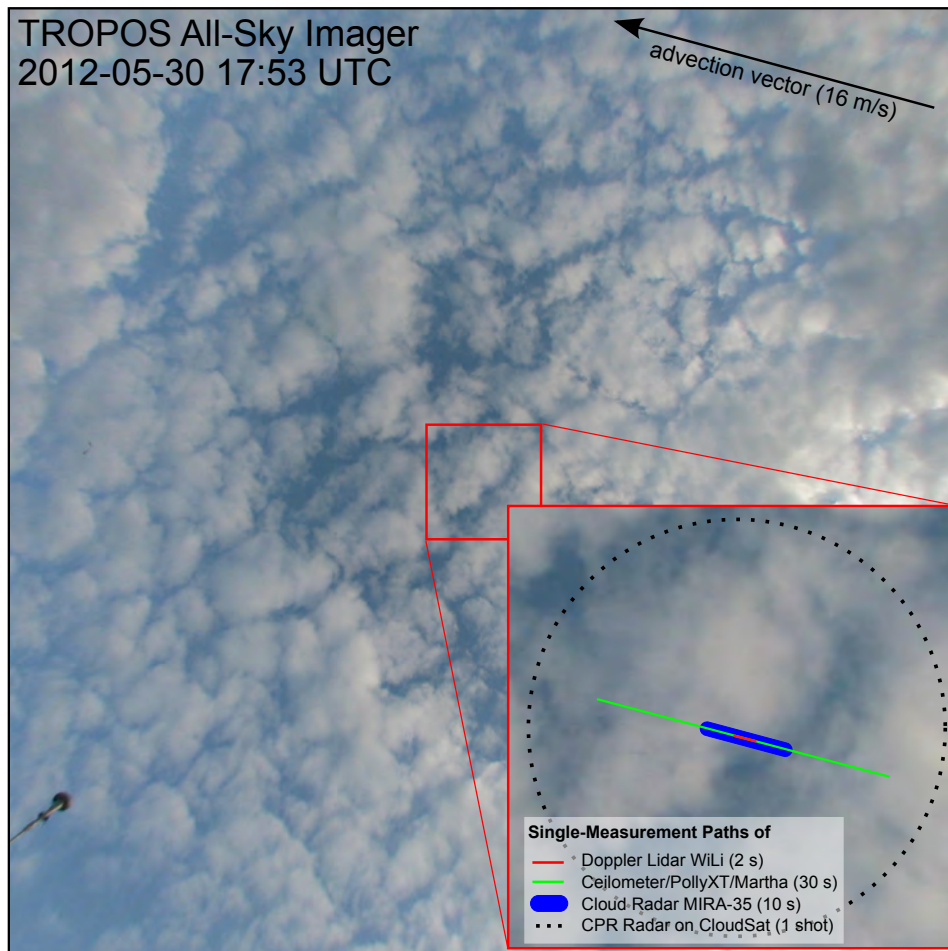


Figure 4.3: Photo from the all-sky imager of an altocumulus cloud depicted together with time series of lidar backscatter (ceilometer), vertical velocity (WiLi), radar reflectivity factor (MIRA-35 cloud radar) and the Cloudnet target classification product. The red line indicates the time of the photo. In the magnified portion of the photo the size of the observation areas of the LACROS remote sensing instruments and, additionally, the footprint of the Cloud Profiling Radar (CPR) on the CloudSat Satellite are shown.

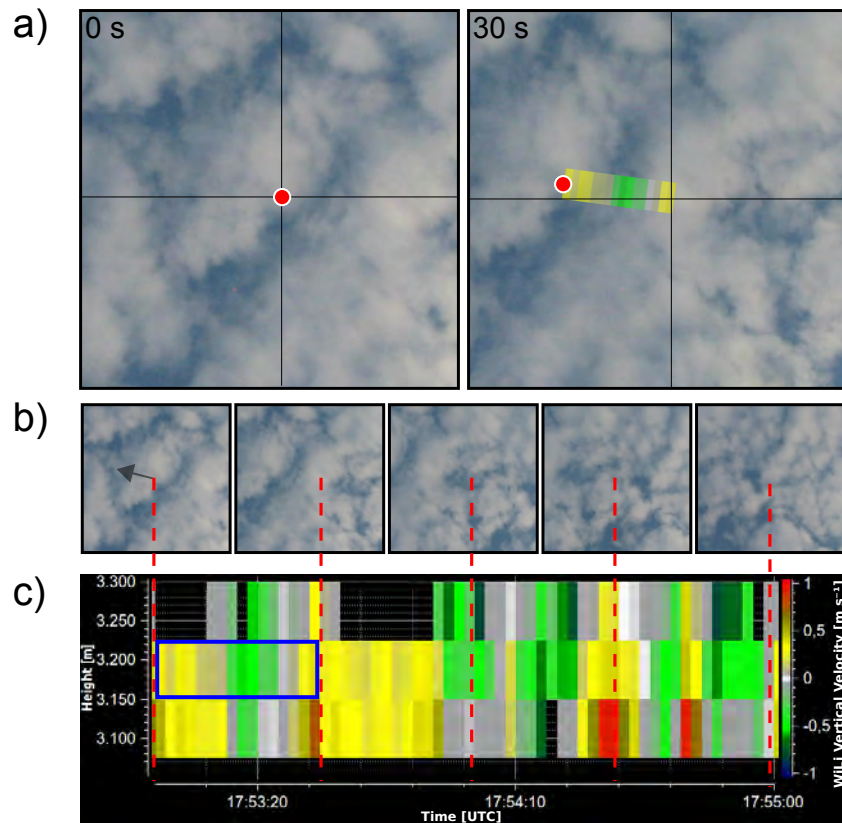


Figure 4.4: Comparison between vertical velocity measured by the Doppler lidar and photographs from the all-sky imager ($\pm 15^\circ$ around zenith) taken simultaneously. Time of the photographs is ± 1 min around 17:54 UTC (like in Fig. 4.3). Panel a) shows two cloud-camera images taken 30 s apart. In this time period the change in the image is governed by the movement of the total cloud field, changes in the visible cloud pattern itself are negligible. By overlaying the corresponding vertical-velocity measurements from WiLi (for velocity scale and height see (c)) at cloud base, one can see cloud formation in the updraft regions (yellow) and cloud evaporation where downdrafts prevail (green). Panel b) shows a series of images and panel c) the simultaneously recorded Doppler-lidar measurements over about 2 min.

is depicted. It shows that updrafts (yellow and red color) are mainly connected with the visible parts of the cloud, while downdrafts (green and blue) are mainly seen where there are visible gaps in the broken cloud pattern.

4.3 Measurement strategy for the UDINE campaign at Leipzig (2010–2013)

LACROS has been run operationally since August 2011. It was a goal of the UDINE project to integrate Doppler Wind Lidar “WiLi”, developed at TROPOS from 2002 to 2005, into the measurement platform LACROS. To enable unattended long-duration measurements with WiLi, remote supervision and control software was developed and

installed together with additional hardware. WiLi was set to measure vertically with high temporal resolution (2 s per profile). Simultaneously, Cloudnet derived microphysical properties like LWC and IWC with ceilometer, cloud radar and microwave radiometer. From the PollyXT lidar mainly the polarization information has been used to decide whether falling particles are ice crystals or liquid water droplets. To get more insight into the nature of falling particles, four times an hour WiLi performed a 1 min long “rocking over the zenith” (ROZ) scan to search for specular reflections of oriented ice particles in cloud virgae [Westbrook et al., 2010]. In this observation mode, the scanner is tilted $\pm 2^\circ$ off-zenith in 0.25° steps. If in such a scan a drop in signal strength between the zenith and the off-zenith measurement is detected, the presence of oriented ice particles is probable [Westbrook et al., 2010]. Such observations are used in the LACROS particle classification scheme presented in Section 4.5.

During a ROZ scan an error is introduced into the vertical-velocity signal by the advection speed, because the lidar does no longer point perpendicular to it. One can estimate the maximum error introduced into vertical-velocity measurements at cloud base to $\sin(2^\circ) \times 15 \text{ m s}^{-1} = 0.52 \text{ m s}^{-1}$ (assuming an advection speed of 15 m s^{-1}). This error affects about 6% of the measurement time of WiLi between 2011 and mid 2012. To keep this error out of the vertical-velocity statistics, off-zenith profiles are omitted when assembling the vertical-velocity statistics in Chapter 6.

4.4 LACROS data storage and processing

Under normal conditions, the amount of raw data recorded by the main instruments of the LACROS platform is on the order of 20 Gigabyte per day. Hence, significant effort is necessary to process data and make it available to users. For that purpose, LACROS makes great use of the data collecting, sorting and processing abilities of the Cloudnet software. The Cloudnet algorithms can handle a wide variety of remote-sensing instruments, especially the MIRA-35 cloud radar. Recorded data is processed in near-real time, however, still depending on the availability of weather-model input data. After processing, data products are available on a fixed 30-s timegrid.

For immediate and direct access to the raw data of the LACROS instruments, the **LACROS Research Data Application** (LARDA) software suite has been developed. It can process and display data of any LACROS instrument on a common time and height grid, independent of the original time or height interval of the instruments. Large-scale meteorological information from the GDAS (Global Data Assimilation System) dataset can also be accessed. The LARDA software allows to quickly access, analyze and compare data from the numerous LACROS systems. Interesting time-height sections can be marked as cases with a special visualization software. The cases are then stored in a simple database and can be recalled and processed later at any time. An overview about the software and the data processing chain is given in Fig. 4.5. An overview about the usage of the data products is given in Fig. 4.6.

So far, one program for fast visualization and case selection (LARDA Explorer) and one program for advanced data evaluation (pyLARDA) have been developed in the

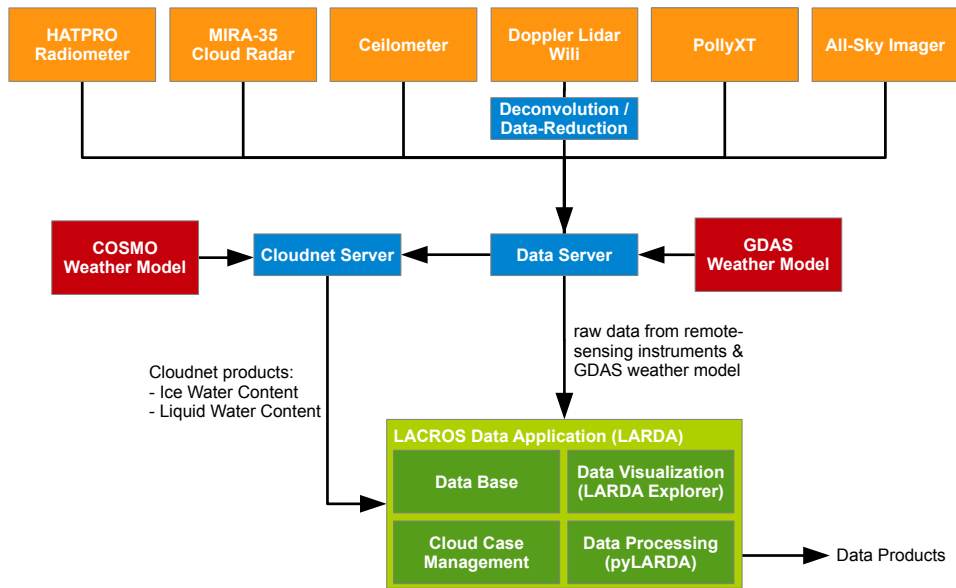


Figure 4.5: Overview about the data acquisition chain.

	Radar	Lidar	Models	Cloudnet
Measurement Values	Radar Reflectivity	Backscatter Coefficient	Pressure	Ice-Water Content
	Vertical Velocity	Vertical Velocity	Temperature	Liquid-Water Content
	Linear Depolarization Ratio	Volume Depolarization Ratio	Advection Speed	
Data Products	LACROS Target Classification (Separating Mixed-Phase and Liquid Clouds)			
	Eddy Structure Analysis			
	Vertical Velocity Statistics at Cloud Base and in Virga (Lidar & Radar)			
	Mixed-Phase Cloud Statistics / Quantification of Heterogenous Ice Formation			

Figure 4.6: Overview about the data processing leading to the products used in this work.

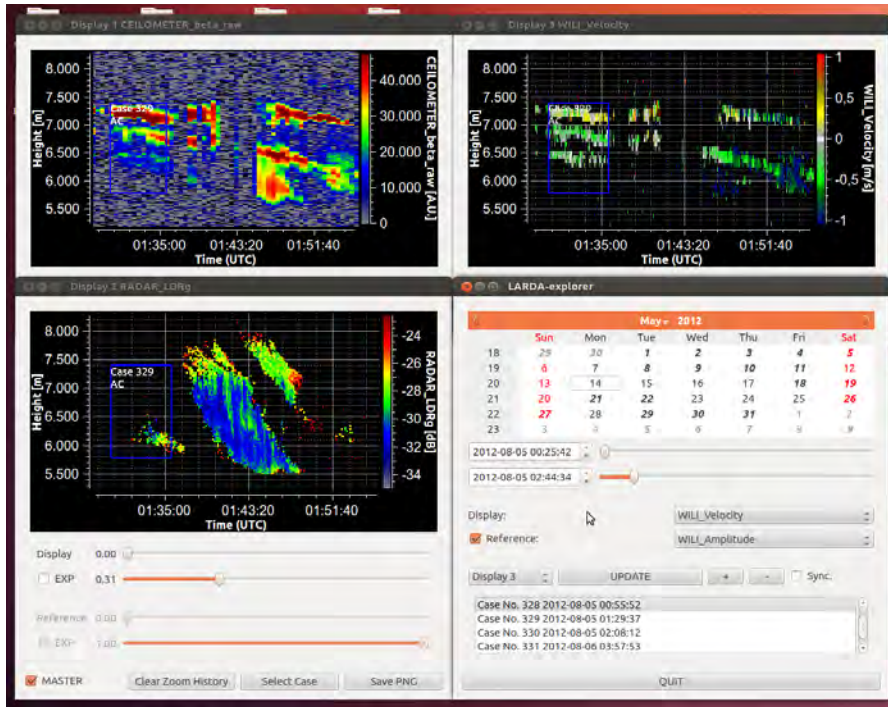


Figure 4.7: Screenshot of the LARDA Explorer computer program. Desired time frame and measurement values are selected in the lower right window and consecutively shown in the display windows. The user can then zoom into any display window and select a time-height frame as a “case”. The selected cases are stored on harddisk and processed by the pyLARDA software (see flowchart in Fig. 4.5).

popular programming languages C++ and Python, respectively. A screenshot of the LARDA Explorer is shown in Fig. 4.7. Only such a generalized approach gives the possibility to efficiently handle the large amount of data analyzed in the context of this work.

4.5 Mixed-phase cloud classification scheme

One of the most important tasks within the data evaluation process is to decide reliably, whether a cloud layer is mixed-phase or liquid only. To answer this question in a reproducible way, a fixed cloud-phase classification scheme is used for all clouds under study. Figure 4.8 presents a flowchart of the decision process. The decision scheme is constructed in such a way that it can be used for different configurations of LACROS. During the UDINE campaign the LACROS measurement system was in a build-up phase. Thus, not all cases could be recorded with all systems. Especially the PollyXT lidar was not available all the time due to deployment in other projects. During the SAMUM-2 campaign the cloud radar was not yet present.

The classification process starts with selecting a layered cloud (AC, stratocumulus (SC), altostratus (AS)) in the LARDA Explorer. Basic selection criteria comprise, e.g.,

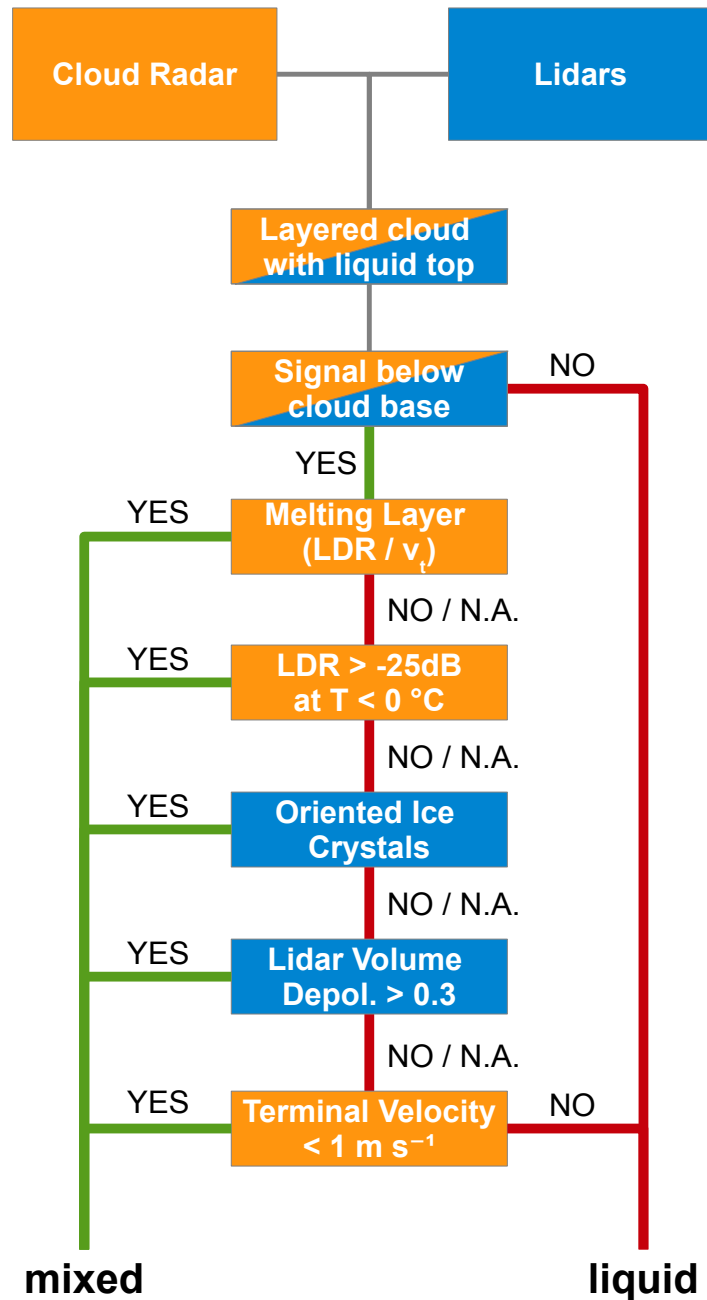


Figure 4.8: LACROS Cloud Phase Classification Scheme. The scheme is created for different configurations of LACROS. A combination of a ceilometer and a cloud radar is required. Additional polarization lidar is optional, but strongly recommended. Reliable detection of oriented ice crystals is only possible with a scanning lidar (WiLi) or a combination of vertically pointing and off-zenith pointing lidars. If any of these systems is not available (N.A.), the decision step is skipped. This lowers the rate of unambiguously classifiable clouds. Terminal fall velocity is only used as a last option. For the UDINE cloud classification, terminal fall velocity is used in less than 5% of the cases and has only to be applied at high clouds with low signal. At lower levels, the signal of the lidar and radar are usually strong enough to apply one of the other criteria.

a homogeneous liquid-cloud top, a layer thickness of smaller than 500 m and a length of at least 5 min. The selection process is further described in Section 6.1. If no particles are detected below the liquid-cloud top, the cloud is classified as liquid. If any falling particle is detected, the particle’s phase is determined in five steps by referring to the polarization measurements of lidar and radar and particle fall velocity:

- The presence of a melting layer around $T = 0\text{ }^{\circ}\text{C}$ unambiguously indicates the presence of ice particles. In this layer particles wet, clump and form big aggregates, before melting into drizzle or rain droplets [Di Girolamo et al., 2012]. The melting layer can be easily identified in the radar measurements due to the extremely high radar reflectivity (0 dBZ) and depolarization ratio ($-10\dots-5$ dB). Also a rapid change in terminal fall velocity from $v_t < 1\text{ m s}^{-1}$ to $v_t > 3\text{ m s}^{-1}$ is usually visible.
- If no melting layer is present, the particles dissolve at $T < 0\text{ }^{\circ}\text{C}$ and the volume depolarization ratio δ_p of the particles has to be considered. For ice particles, lidar or radar should show a considerable volume depolarization ratio of at least 20% or -25 dB, respectively.
- If no polarization lidar is present and the radar does not show any sign of depolarization, it is still possible that ice particles are present. Hence, the final decision between drizzle droplets and ice crystals is made by considering the fall velocity of the particles. Those will be ice with high certainty, if they show terminal fall velocities below 1 m s^{-1} .

The ice crystals’ ambient temperature is intentionally not taken into account in the classification scheme, because the temperature dependence of ice nucleation is subject of analysis. In contrast, the current Cloudnet target classification scheme relies on the ambient temperature and, therefore, does not yield independent information about ice freezing behavior. In the context of this work, the classification scheme presented here is applied manually for each cloud case, which ensures high data quality. The scheme may have the potential to be automatized, e.g., in the framework of Cloudnet.

5 Lidar and radar synergy. Part II: Vertical-velocity measurement with Doppler lidar, cloud radar and wind profiler

The characterization of vertical motions in the atmosphere needs dedicated instruments and measurement strategies. In this work, the main focus lies on the measurement of vertical air motions at and around cloud bases. Doppler lidars deliver a strong signal from liquid cloud-bases and seem to be ideally suited for that purpose. In the following chapter it is shown that this strong signal gradient can, however, pose problems for Doppler lidars with chirped laser pulses. A new method to correct the laser chirp effect in Doppler lidar spectra is presented and, therefore, a thorough description of the Doppler lidar data processing and the correction method is given. Consecutively, the cloud-radar data processing scheme is introduced. Connections between simultaneous co-located Doppler-lidar and cloud-radar vertical-velocity measurements are established and the ability of both instruments to measure turbulence at cloud base is investigated.

All methods, presented up to this point, are applied to measurements taken solely by instruments of LACROS. The information collected by these measurement systems is sufficient to get insight into the air movements in cloud layers. However, from the vertical movement inside the cloud layer one can draw only indirect and ambiguous conclusions about the clear-air movements surrounding the cloud layers. This information can be acquired directly by powerful radar wind profilers. Motivated by the results of this work, measurements were carried out with a wind profiler at MOL. Similar to the LACROS configuration, the wind profiler at MOL is accompanied by a co-located Streamline Doppler lidar and a MIRA-35 cloud radar. This combination of instruments is unique and its potential is explored in this work. First results of this small measurement campaign are presented at the end of this chapter.

5.1 Doppler wind lidar

The following section is based on Bühl et al. [2012]. Symbols have been adapted to this work.

5.1.1 Introduction to the Doppler-lidar principle

In the last decades, coherent Doppler lidars (CDL) have proven to be important tools for atmospheric wind research [Henderson et al., 2005]. They have been used to measure boundary-layer convection [e.g., Frehlich et al., 1998; Ansmann et al., 2010], vertical wind velocities at cloud bases [Lottman et al., 2001; Grund et al., 2001], fluxes of latent heat [Giez et al., 1999; Kiemle et al., 2007] and fluxes of aerosol particles [Engelmann et al., 2008]. Recently, the application of Doppler lidars was studied to improve the energy output of wind power plants [Harris et al., 2006; Käsler et al., 2010]. They are also regularly employed on research aircraft [Weissmann et al., 2005; Reitebuch et al., 2003].

A CDL emits a laser pulse of narrow bandwidth and measures the relativistic Doppler shift f of the light backscattered from atmospheric particles. The velocity v of the particles and thus of the surrounding air is then calculated by

$$v = \frac{\lambda}{2} f, \quad (5.1)$$

with λ being the wavelength of the emitted pulse. A minimum pulse length is necessary for a precise determination of the Doppler frequency shift because of the time-bandwidth product

$$\delta f \times \tau = \delta f \times \frac{l}{c_l} = \gamma. \quad (5.2)$$

δf is the bandwidth, τ is the duration of the laser pulse, l the pulse length and c_l the speed of light [Paschotta, 2008]. γ is a constant that depends on the pulse shape. In this context $\gamma = 0.44$ for a Gaussian-shaped pulse.

For wind lidars, a trade-off between range and frequency resolution has to be found. For example, the CDL used in the context of this work has a pulse length of about $l = 175$ m which leads to a bandwidth of $\delta f \approx 750$ kHz for one laser shot. The uncertainty introduced by the pulse bandwidth can be partly overcome by averaging over many laser shots [Frehlich, 2001; Smalikho et al., 2005], but there are other important influences that determine the measurement error of wind velocity measurements. Examples are the lidar pointing accuracy, turbulent spectral broadening [Banakh and Werner, 2005] and the chirp of the laser pulse of solid-state and CO₂ lasers. A laser pulse chirp is a gradual change in the frequency of the laser light during pulse emission (see Fig. 5.1). For solid-state lasers it can result from nonlinear optical effects within the active medium (e.g., inversion-dependent change of refractive index). For WiLi, the frequency deviation of the laser pulse is shown in Fig. 5.1. In Section 5.5.1.1 a similar laser chirp effect is identified in the commercial Streamline Doppler lidar of HALO Photonics company.

Around strong signal gradients (e.g., at cloud bases) the chirp effect leads to the detection of artificial velocities (Fig. 5.2), but it also affects continuous signals of boundary-layer aerosol, optically thin clouds, virgae, etc. (see Fig. 5.3). Within such continuous signals, the measured velocity is shifted by a constant factor, if the light emitted before and after the pulse peak is shifted towards the same side of the spectrum or, in general, when the chirp is nonlinear [Dabas et al., 1998]. Hence, light scattered back by an air

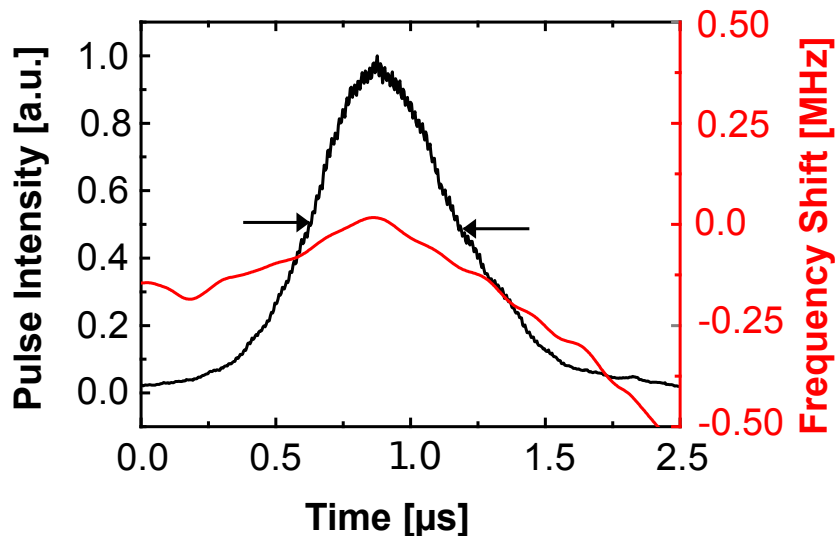


Figure 5.1: One laser pulse recorded with the heterodyne reference detector. On the left axis the intensity (temporal average of the squared raw heterodyne amplitude) is depicted. The arrows indicate the intensity FWHM to be about 590 ns. The right axis shows the shift in the main frequency of the raw heterodyne signal determined by a sliding Fourier transform. The pulse chirp is about $+0.25 \text{ MHz } \mu\text{s}^{-1}$ before and $-0.5 \text{ MHz } \mu\text{s}^{-1}$ after the pulse maximum.

volume is overlaid by frequency-shifted light from uprange and downrange air volumes leading to a shift of the spectral peak and, therefore, to the detection of biased wind velocities. This bias and the distortions in the velocity profile have to be taken into account especially when dealing with vertical velocities. Korolev and Isaac [2003] showed that up- or downdrafts of only a few centimeters per second can already decisively influence the meteorological processes within an air parcel.

Up to now, a lot of effort has been put into the improvement of laser designs and hardware chirp correction [Wulfmeyer et al., 2000]. If hardware changes are not desired or not applicable, the correction of the chirp effect can also be done on software basis by deconvolution techniques [Gurdev and Dreischuh, 2003, 2008; Zhao and Hardesty, 1988]. The techniques which were presented up to now mostly involve the direct deconvolution of the raw heterodyne signal. In this work, however, a two-dimensional deconvolution is applied on the averaged spectra, in order to correct the chirp-induced velocity bias while simultaneously improving the range and frequency resolution of WiLi. The processing of the recorded heterodyne signal is kept very simple: the digitally recorded raw heterodyne signal is split into overlapping range gates and the Fourier spectrum is calculated for each of them.

These averaged, height-resolved Doppler spectra are treated like an image blurred by a certain point-spread-function (PSF). The PSF corresponds to the spectra of the reference laser pulse, recorded at the beginning of the dataset. It is shown in this section that it is possible to apply two-dimensional deconvolution techniques, known from image restoration and enhancement, to remove the influence of the chirped laser pulse from the datasets. A major difference of this approach compared with other deconvolution

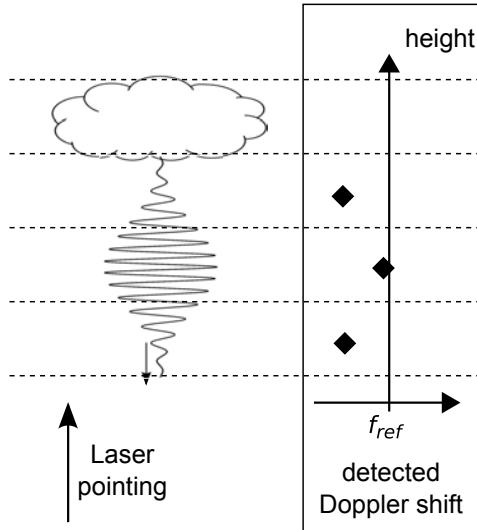


Figure 5.2: Sketch of the chirp effect in vertical-wind velocity observation at cloud bases: An optically thick cloud effectively returns a copy of the laser pulse which is recorded by the data acquisition software. The Fourier analysis yields a lower Doppler shift at the beginning and at the end of the laser pulse which could be mistaken as negative vertical velocities. The dashed lines represent the height bins of the data acquisition. For simplicity it is shown here without any interpolation.

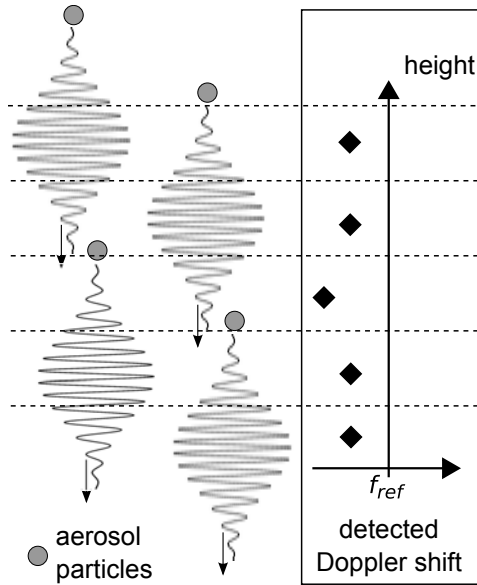


Figure 5.3: Sketch of the chirp effect in vertical-wind velocity observation within the boundary layer: An ensemble of particles returns overlapping copies of the laser pulse. Hence, the strong signal of the center frequency overlaps with chirped lower-frequency signals which effectively shifts the frequency peak of the spectra towards lower frequencies. For WiLi, a shift in the detected vertical velocity of the order of -0.25 ms^{-1} is introduced. In the case of a Gaussian pulse with only a chirped tail the effect is the same, for a completely symmetrical chirp however the effect cancels out. The dashed lines represent the height bins of the data acquisition.

techniques is that it does not need to be employed in real time during data acquisition and does not need access to the raw heterodyne data. It can be applied to the averaged Doppler spectra, which significantly reduces both the complexity of the data acquisition software and the amount of data to be stored. In Section 5.1.2, the CDL system WiLi is presented and the laser pulse characteristics are discussed. Subsequently, the two-dimensional deconvolution is introduced (Section 5.1.3.1) and applied to atmospheric data (Section 5.1.3.2). To further estimate the performance of the two-dimensional deconvolution technique, it is applied to a simulated dataset in Section 5.1.4.

5.1.2 Coherent Doppler lidar WiLi

The CDL WiLi of TROPOS is described in detail in Engelmann et al. [2008], so that only a brief overview is given here. The lidar is equipped with a master-oscillator-power-amplifier (MOPA) design, operating at a wavelength of 2022 nm. The bandwidth of the master oscillator (MO) is 150 kHz. The pulse energy of the power oscillator (PO) is 2 mJ at a pulse repetition frequency of 750 Hz. In Fig. 5.1, the signal intensity of a recorded laser pulse is depicted. The change in frequency was determined with a sliding-window Fourier transform and is overlaid in the figure. The trend to negative frequency shifts at the beginning and at the end of the laser pulse is visible. The pulse chirp is about $+0.25 \text{ MHz } \mu\text{s}^{-1}$ before and $-0.5 \text{ MHz } \mu\text{s}^{-1}$ after the pulse maximum.

The laser pulse shown in Fig. 5.1 has a length (intensity at full width at half maximum (FWHM), see description of Fig. 5.1) of 590 ns and a spectral width of $720 \pm 20 \text{ kHz}$ which is determined from its Fourier spectrum. The spectral width is slightly smaller than the theoretical bandwidth of 750 kHz (see Eq. (5.2)). This deviation can be explained, if one considers that the pulse may not be completely Gaussian. It may rather have a slightly asymmetric shape, typical for Q-switched lasers. Yet, for the deconvolution method presented here, the exact pulse length and spectral shape is not important, because the averaged pulse spectrum itself is the reference for the determination of the wind velocities. The measured bandwidth of the laser pulse corresponds to a velocity uncertainty of about $\pm 0.73 \text{ m s}^{-1}$ for one laser shot (Eq. (5.1)). However, after averaging over 1000 laser shots the standard deviation of the reference peak's frequency fluctuation has reduced to less than $0.73/\sqrt{1000} \approx 0.02 \text{ [m s}^{-1}]$. Thus, the measurement uncertainty for the atmospheric wind velocity is no longer determined by the bandwidth of the outgoing laser pulses, but by the pointing stability of the scanning unit which is about 5 mrad for WiLi. For the error estimation, a maximum horizontal wind speed of 20 m s^{-1} is assumed, which leads to the maximum velocity uncertainty of about 0.10 m s^{-1} for vertical-wind measurements.

While the laser pulse is emitted by the power amplifier, a small fraction is coherently mixed with the light of the master laser at a reference detector. The intermediate frequency of a laser pulse (i.e., the frequency offset between the MO and the PO) is -80 MHz and introduced by an acousto-optical modulator (AOM). The generated heterodyne signal is recorded with 250 MHz. The light scattered backward from atmospheric particles is consecutively detected on another heterodyne detector. For signal switching, a low-noise high-frequency integrated circuit is used. The two receivers use

photodiodes of the same type, have similar amplifiers and their signals are recorded consecutively by the same data acquisition system. The equal detection and data processing of the laser pulse and the atmospheric signal is very important for the deconvolution method explained here.

The heterodyne signal is recorded for 100 μs after the release of the laser pulse, which corresponds to a distance of 15 km in the atmosphere. For one laser shot, the data acquisition system records 25000 data points which are cut into 200 range gates of 250 data points (1 μs), each with an overlap of 125 data points. A Hanning window is applied in order to suppress sidelobes from discontinuities in the signal. In this way, one range gate is of 150 m length at interpolated height steps of $\Delta r = 75$ m. On each range gate a Fast Fourier Transform (FFT) is performed by extending the dataset to 256 points with zeros. Therefore, the width of one frequency bin is $\Delta f = \frac{250 \text{ MHz}}{256} = 0.977$ MHz. With Eq. (5.1) this corresponds to $\Delta v = 0.987 \text{ m s}^{-1}$ for one velocity interval. The processing is done in exactly the same way for both the atmospheric signal and the recorded laser pulse, i.e. the laser pulse is also sampled in a range gate with a length of 1 μs . In Fig. 5.1 it is visible that even a range gate size of two times the FWHM of the pulse does not include the whole pulse. The chirped tail of the pulse is recognized in the next two range gates, too (see also magnification of laser pulse in Fig. 5.4a).

The power spectra are calculated for each range gate of every emitted laser pulse and summed for an integration time of 1 to 5 s, before they are stored on harddisk. This approach greatly reduces the amount of data from 80 Mbytes $^{-1}$ to about 100 kbytes $^{-1}$ but, of course, prohibits any re-analysis of the raw heterodyne signal. The further analysis is done by independent software, which searches for the peaks within the averaged

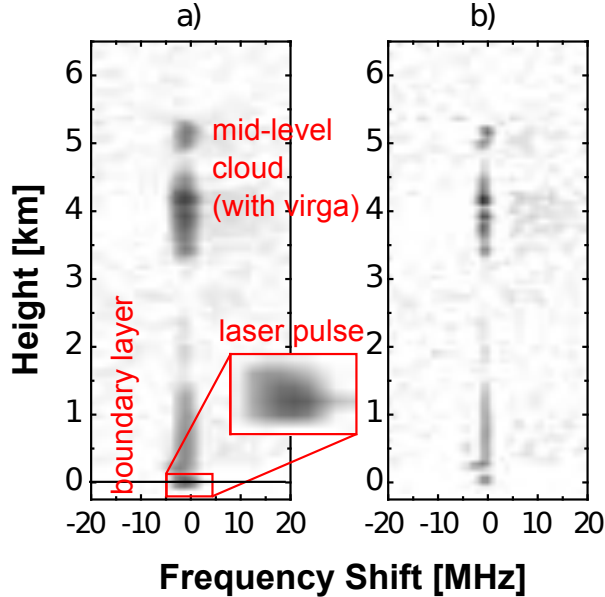


Figure 5.4: An example of Doppler lidar spectra is shown before (a) and after (b) deconvolution. The data was averaged over 1500 laser shots. Atmospheric features and the laser pulse are labeled. The atmospheric measurement from which this profile is taken is shown in Fig. 5.7 at 17:40 UTC.

spectra and computes their first moments for velocity estimation. Consecutively, the mean velocity in each range gate is calculated with Eq. (5.1).

If the range gates are long enough to include a whole laser pulse (including the chirped tail, not only the FWHM), the chirp effect does not play a major role. But when the heterodyne signal is interpolated with range gates smaller than the laser pulse itself, chirp-induced artifacts as described in Section 5.1.1 will appear. Indeed, the bias for continuous signals could be avoided by using the average frequency of the whole outgoing laser pulse as reference frequency. This averaging would largely compensate for the bias, but would in turn shift the velocities at cloud bases into the opposite direction towards positive velocities. Also, the range resolution would be decreased. Therefore, the only possibility to have at the same time correct values at cloud bases and within the boundary layer is to resolve the frequency chirp of the laser pulse in different range gates and use this information to remove the chirp artifacts. In the following section, a deconvolution technique is presented that is capable of removing the chirp artifacts from cloud bases and continuous signals at once.

5.1.3 Application of two-dimensional deconvolution to atmospheric Doppler spectra

5.1.3.1 Method

Let $D^*(\rho = 0 \dots N_\rho, \nu = 0 \dots N_\nu)$ contain the pure and undisturbed information about the intensity scattered back from each element of the discrete range–frequency space. The discrete coordinates are connected with the continuous coordinates like $r = \rho\Delta r$ and $f = \nu\Delta f$.

The formation of the atmospheric power spectra $P_c(\rho, \nu)$ (see Eq. (3.7)) in the receiver can be described by a convolution of $D^*(\rho, \nu)$ with a suitable PSF $P_{\text{PSF}}(\rho, \nu)$. In this context, the PSF consists of the averaged power spectra of the chirped laser pulse at the beginning of the datasets (from $\rho = 0 \dots 4$):

$$P_c(\rho, \nu) = \sum_{i=-N_i}^{N_i} \sum_{j=-N_j}^{N_j} D^*(\rho - i, \nu - j) P_{\text{PSF}}(i, j). \quad (5.3)$$

$(2N_i + 1)$ and $(2N_j + 1)$ are the frequency and the range extent of the PSF, respectively. Application of the convolution theorem [Goodman, 2005a] on Eq. (5.3) yields

$$\text{DFT}[P_c(\rho, \nu)] = \text{DFT}[D^*(\rho, \nu)] \text{DFT}[P_{\text{PSF}}(\rho, \nu)], \quad (5.4)$$

with the Discrete Fourier Transformation DFT. For this case, of course, $P_{\text{PSF}}(\rho, \nu)$ has to be extended with zero values to be of the same size as $D^*(\rho, \nu)$.

Removing the effect of the chirped laser pulse from the dataset requires to undo the convolution operation in order to recover the original atmospheric information $D^*(\rho, \nu)$. Theoretically, it is possible to divide Eq. (5.4) by $\text{DFT}[P_{\text{PSF}}(\rho, \nu)]$ and to apply an inverse Fourier transformation afterwards. However, this approach usually fails, because

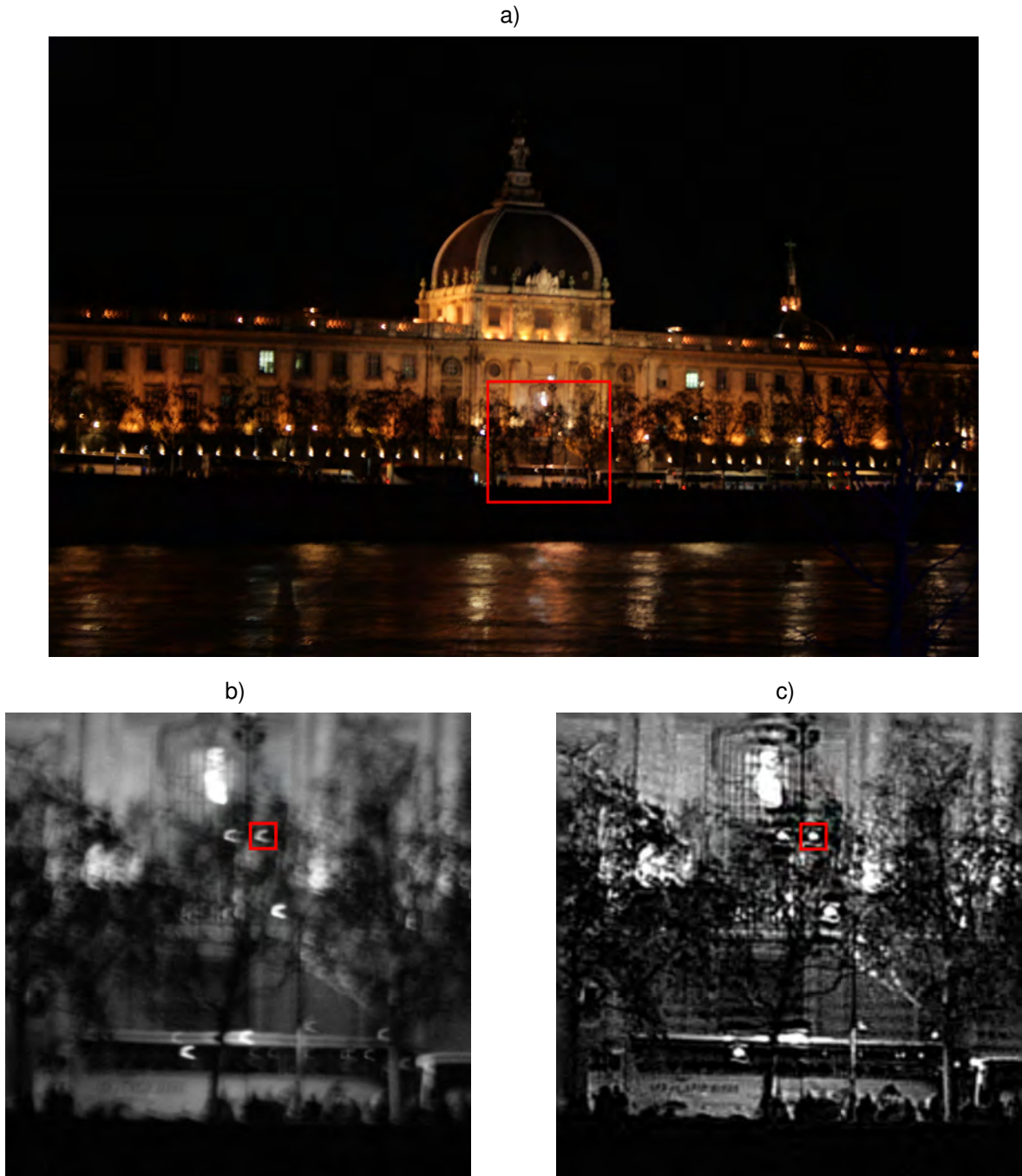


Figure 5.5: Example of two-dimensional deconvolution. The image of the *Hôtel-Dieu de Lyon* in (a) is blurred, because the camera was moved during exposure. From the street lights that are pictured in front of a darker background, it is visible that the camera was moved in a half-circle. The undisturbed image of such a street light can be assumed point-like, so that its blurred image can be used as a PSF for deconvolution (b). The resulting deconvolved image is shown in (c). The image was taken at Lyon, France on 8 December 2007.

of noise amplification. The direct inversion of the deconvolution by solving the equation system presented by Eq. (5.3) is also not possible, because the equation system is underdetermined. Therefore, an iterative deconvolution algorithm has to be applied in order to retrieve an approximation of the input information $D^*(\rho, \nu)$.

Iterative two-dimensional deconvolution algorithms are best known from confocal microscopy [Baddeley et al., 2006] and astronomy. For the application presented here, the Richardson–Lucy (RL) algorithm is used [Richardson, 1972; Lucy, 1974]. It is famous for its application on blurred images of the Hubble Space Telescope [Stobie et al., 1994]. But this algorithm is not the only one available. There exist various other algorithms which could be applied here, too. Most of them are already available in ready-to-use software packages. An example of a deconvolution applied on a blurred photographic picture is shown in Fig. 5.5. A flowchart of the deconvolution operation is given in Fig. 5.6.

The RL algorithm is an iterative algorithm, which tries to reproduce the function $P_c(\rho, \nu)$ (Eq. (5.3)) by making an initial guess of $D^*(\rho, \nu)$ and then convolving this guess with a provided point spread function $P_{\text{PSF}}(\rho, \nu)$. The initial guess can, e.g., be provided by directly solving Eq. (5.4) as explained above, or it can be the disturbed dataset itself. The disparity between the resulting dataset $P_c^*(\rho, \nu)$ and $P_c(\rho, \nu)$ is then used to make a better estimate of $D^*(\rho, \nu)$ in the next iteration step. The iteration is stopped after a defined number of steps, or when the difference between $P_c^*(r, f)$ and $P_c(r, f)$ has become smaller than a defined threshold. In order to increase the convergence speed of the RL algorithm, a vector-extrapolation-based acceleration technique is used here [Biggs and Andrews, 1997; Remmele and Hesser, 2009]. $P_c^*(r, f)$ can serve as a test function

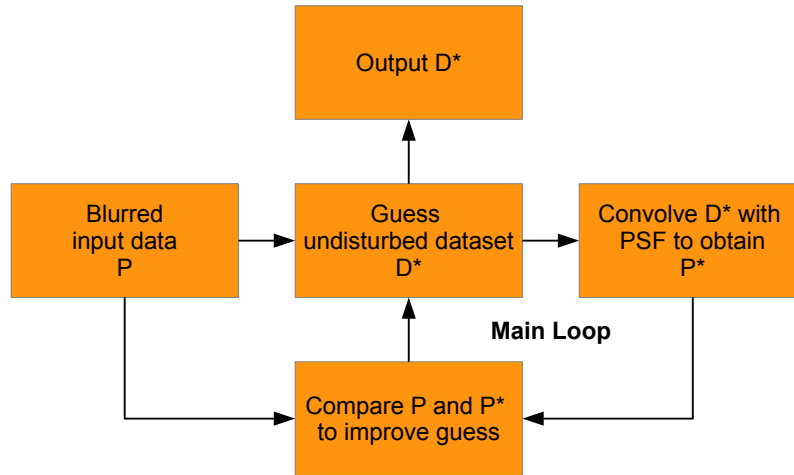


Figure 5.6: Illustration of the forward-iteration procedure for two-dimensional deconvolution. The main step is the guessing of the unknown function D^* and the consecutive convolution with the known PSF. The deviations between P and P^* are then used to make a better guess in the next step.

to determine whether the deconvolution was successful or not. If $P_c^*(r, f)$ converges towards a shape strongly different from $P_c(r, f)$, it may, e.g., indicate that an incorrect PSF was used. This test will be applied later in this work during the deconvolution of radar spectra in Chapter 7.

A lot of different software solutions exist which can perform an iterative two-dimensional deconvolution. For this work, the implementation of the RL algorithm of the image restoration software “BiaQIm” [Tadrous, 2011] was used. It was favorable, because it has command-line access and can read arbitrary floating-point data. On a desktop computer the software needs less than one second for the deconvolution of one dataset with 196 range gates. Since the acquisition time for one dataset is at minimum 1 s, for WiLi the operation can be performed in real time during measurements, but it can also be applied afterwards on the stored spectra. Both types of operation have been implemented in the context of this work.

5.1.3.2 Improvement of the velocity estimation for atmospheric data

Figure 5.7 shows an example of an atmospheric measurement with the vertically pointing WiLi at Leipzig on 13 March 2011. The top two panels show the signal intensity (in the following, the term “intensity” is used to describe the estimated amplitude of a signal peak after background subtraction), the vertical velocity within the planetary boundary layer (0 to 3 km height) and the terminal velocity of ice particles and water droplets in the virgae of altocumulus clouds (3 to 6 km height). The spectra were averaged over 1500 laser shots (2 s). The chirp effect is visible above and below clouds (e.g., in the magnified portion) and at positions where the intensity is very high. At the bottom and at the top of those structures negative velocities seem to appear, which could be mistaken as falling particles or downdrafts. These artifacts originate from backscattered light from the beginning (bottom chirp effect) and from the end (top chirp effect) of the laser pulse.

To correct the chirp effect in the entire measurement of Fig. 5.7, the RL algorithm was applied on each 2-s dataset independently with ten iteration steps. The result is shown in Fig. 5.7c and 5.7d. The velocities within the optically thin cloud layers and the boundary layer are shifted and there is no longer an overall trend to negative vertical-velocity values. The removal of the velocity bias is nicely visible in the boundary layer from 17:30 to 18:00 UTC. The deconvolution shifts the detected wind velocities by about 0.25 m s^{-1} towards positive values. Artificial velocities at the cloud bases and the cloud tops are no longer present. The method works equally for weak and strong signals.

Figure 5.4a presents an example profile, marked with a dotted line at 17:40 UTC in the atmospheric measurement of Fig. 5.7. The chirped laser pulse is magnified. The dataset was deconvolved with the accelerated RL algorithm (10 iterations) using the recorded laser pulse at the beginning of the dataset as a PSF. Fig. 5.8 shows a comparison between the vertical velocities estimated from the untreated (Fig. 5.8a) and the deconvolved dataset (Fig. 5.8b). In Fig. 5.4b it is visible that the recorded reference laser pulse has been reduced to nearly one bin in range and frequency dimension. That means that now the resolution of the dataset matches the grid and is close to its theoretical maximum.

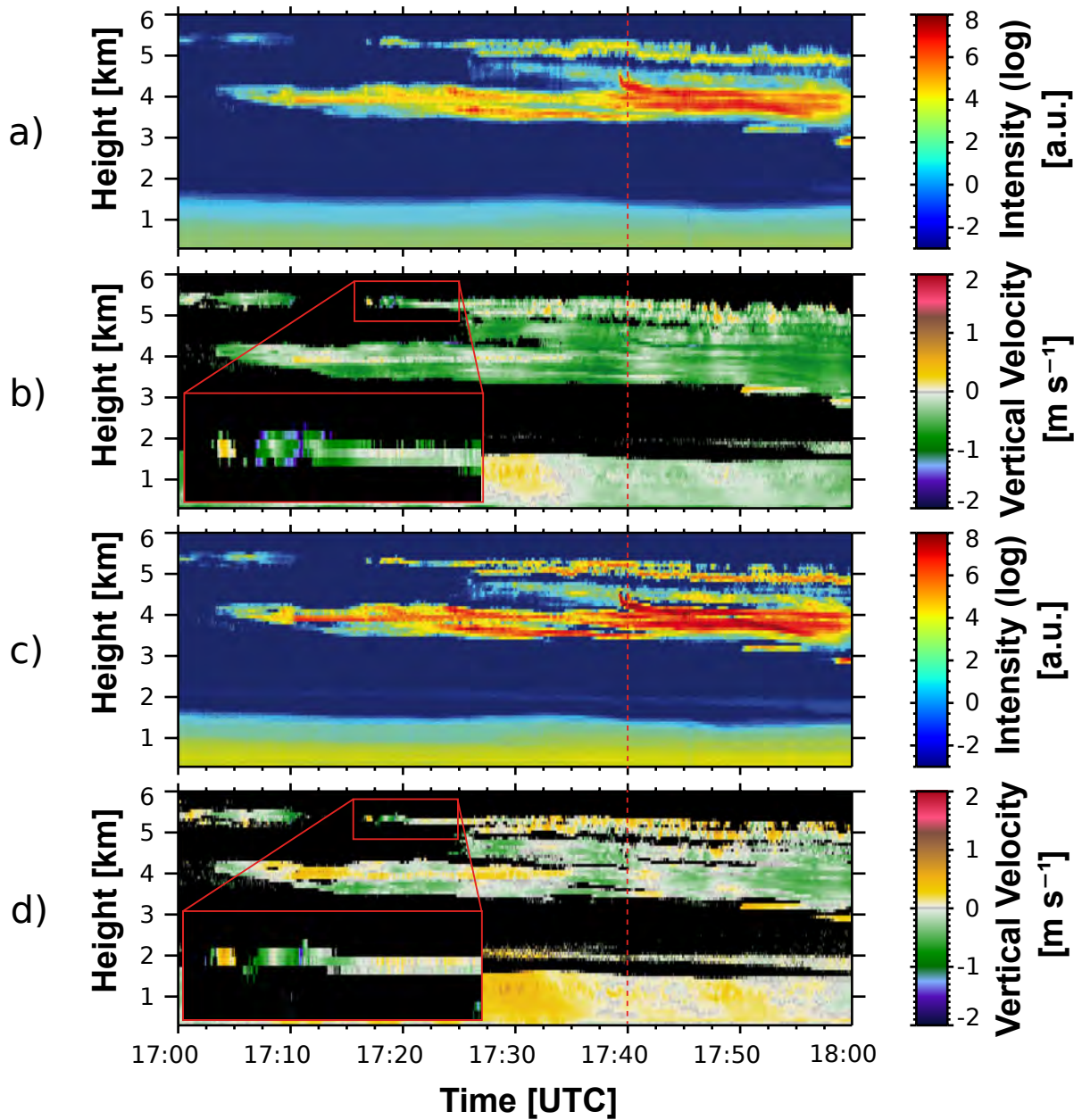


Figure 5.7: Application of the deconvolution technique on a measurement of WiLi performed at Leipzig on 11 March 2011. In a) and b) the signal intensities and the vertical velocity distribution of an atmospheric measurement of the boundary layer and mid-level cloud layers are depicted. In the red box the chirp effect is visible above and below the cloud as artificial negative velocities (green color). c) and d) show the same measurement after correction of the chirp effect by deconvolution. The dashed red line at 17:40 UTC indicates the position of the example measurement shown in Fig. 5.4. The chirp effect is visible above and below the cloud layers in the magnified portions of the velocity plots.

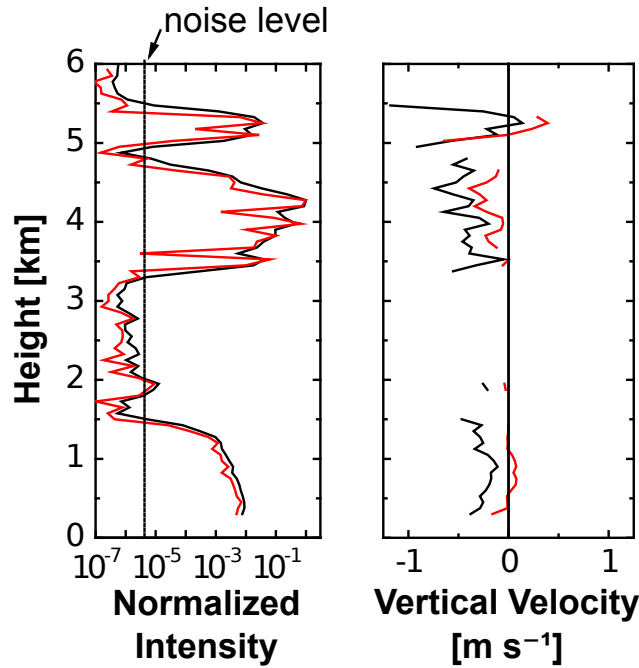


Figure 5.8: Signal intensities (left) and velocities (right) calculated by means of the peak-finding software from the raw atmospheric dataset (black line) and from the deconvolved dataset (red line). The input data is depicted in Fig. 5.4a and b.

5.1.3.3 Improvement of the range resolution

The deconvolution technique presented in this work does not only correct the chirp effect. It also simultaneously improves the range and the frequency resolution of the spectra. The improvement of the range resolution is visible, e.g., in Fig. 5.4 between 3 and 6 km height. The single layers are much better separated after the deconvolution method has been applied. In Fig. 5.7c the features within the cloud layers are also much more distinct than in Fig. 5.7a. The qualification of the resolution improvement is given in Section 5.1.4.

5.1.3.4 Improvement of the frequency resolution

In most cases, a frequency resolution improvement is not needed because only one spectral peak is present (e.g., Fig. 5.7). But there are certain conditions under which an improvement of the frequency resolution can be of advantage. Fig. 5.9a shows spectra averaged over 5 s (3600 laser shots) that were observed on 29 March 2006, when the onset of rainfall was recorded in low-level clouds at 750 m height. At that height, the spectra split and two peaks appear. Here, water drops (likely drizzle) fall with -3.5 m s^{-1} out of the cloud, which itself is composed of smaller droplets which move slowly upwards at 0.2 m s^{-1} . Fig. 5.10 shows the Doppler frequency shift between the arrows in Fig. 5.9a and 5.9b. After deconvolution the peaks are much better separated. This case also highlights that it is possible to apply the deconvolution procedure on historic datasets.

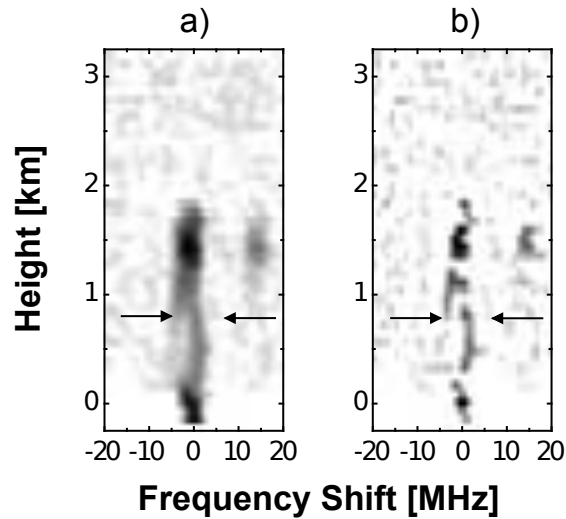


Figure 5.9: Comparison between (a) the raw atmospheric and (b) the deconvolved Doppler spectra recorded during rainfall at Leipzig on 29 March 2006. Double peaks resulting from upwards driven aerosol particles and falling raindrops, respectively, are visible in the spectra at about 750 m height. The two spectra marked by arrows are shown in Fig. 5.10. (The structure at 1.5 km height and 15 MHz is an artifact, presumably resulting from a weak parasitic laser line of the MO. Yet, this does not affect the central part of the spectrum.)

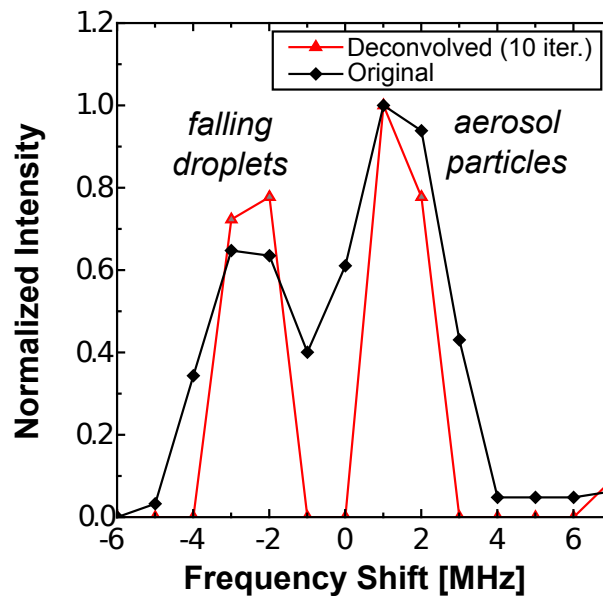


Figure 5.10: Atmospheric Doppler spectra during the rainfall event of Fig. 5.9. The improvement of frequency resolution between the original dataset (black line) and the deconvolved dataset (red line) is visible.

5.1.4 Iterative deconvolution of modeled spectra

In order to characterize the performance of the deconvolution technique, a test dataset was created by convolution of artificial input data with the spectra of a real laser pulse from WiLi. Consequently, the modeled spectra and the real datasets are on the same grid. The simulation indicates the magnitude of the velocity deviations introduced by the chirp effect of WiLi.

The discrete input spectra $D^*(\rho, \nu)$ created for this simulation are shown in Fig. 5.11a. They are intentionally similar to the spectra in Fig. 5.4a. Between 0 and 2 km a planetary boundary layer is simulated with a continuously decreasing intensity at the 0-MHz frequency bin. On the top of the boundary layer two cloud layers separated by one range step of $\Delta r = 75$ m were added. In the free troposphere between 3 and 6 km AC clouds with virgae are modeled. All modeled air volumes have a simulated Doppler shift of 0 MHz, which also corresponds to 0 m s^{-1} vertical velocity. Only the virgae of the AC clouds have a Doppler shift of -0.977 MHz, which corresponds to a terminal velocity of -0.987 m s^{-1} . These modeled ideal spectra $D^*(\rho, \nu)$ were then convolved with the recorded PSF from Fig. 5.4a according to Eq. (5.3). Since the PSF and the modeled spectra are on the same grid, a discrete convolution like in Eq. (5.3) can be performed.

Fig. 5.11b shows the modeled artificial spectra after convolution with the PSF from Fig. 5.4. Fig. 5.12a and 5.12b show the intensities and the vertical wind velocities, respectively, detected by the peak-finding software as a function of height. In this representation, the optically thick clouds are delta-function-like point sources (small range extent, high intensity). They effectively return a copy of the laser pulse. Therefore, around the clouds the characteristic chirp effect is best visible. Within the continuous signal of the planetary boundary layer or the virgae the chirped pulse smears the spectra out. Consequently, an offset of about -0.25 m s^{-1} is introduced, compared with the input spectra.

The deconvolution of the spectra in Fig. 5.11b is shown in Fig. 5.11c for five iterations and in Fig. 5.11d for ten iterations. The same PSF which was used to generate the modeled spectra was applied here to iteratively deconvolve them with the method described in Section 5.1.3. Fig. 5.12b shows the detected velocities calculated from the spectra deconvolved with ten iterations as a dotted red line. It is important to consider a reasonable threshold on the signal intensity, because the velocity estimation at very small intensities can yield wrong results. Therefore, in this simulation normalized intensities smaller than 0.05 are considered as noise and are not taken into account for the velocity evaluation process. After ten iteration steps the velocity readings within the continuous signals are shifted back to their initial values (0 m s^{-1} in the boundary layer and -0.987 m s^{-1} in the virga) and the cloud peaks are reduced to one height step again. After ten iteration steps the maximum deviation between the input signal and the deconvolved signal is 0.02 m s^{-1} (see Fig. 5.12c), which is well below the nominal measurement accuracy of 0.10 m s^{-1} of WiLi.

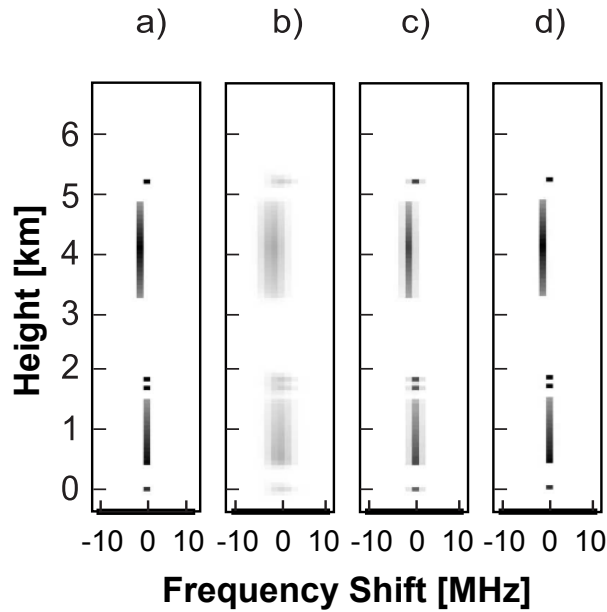


Figure 5.11: Overview of the different steps of the simulation: a) ideal input spectra, b) raw spectra as they would be detected by the wind lidar, spectra deconvolved with 5 iterations (c) and (d) with 10 iterations.

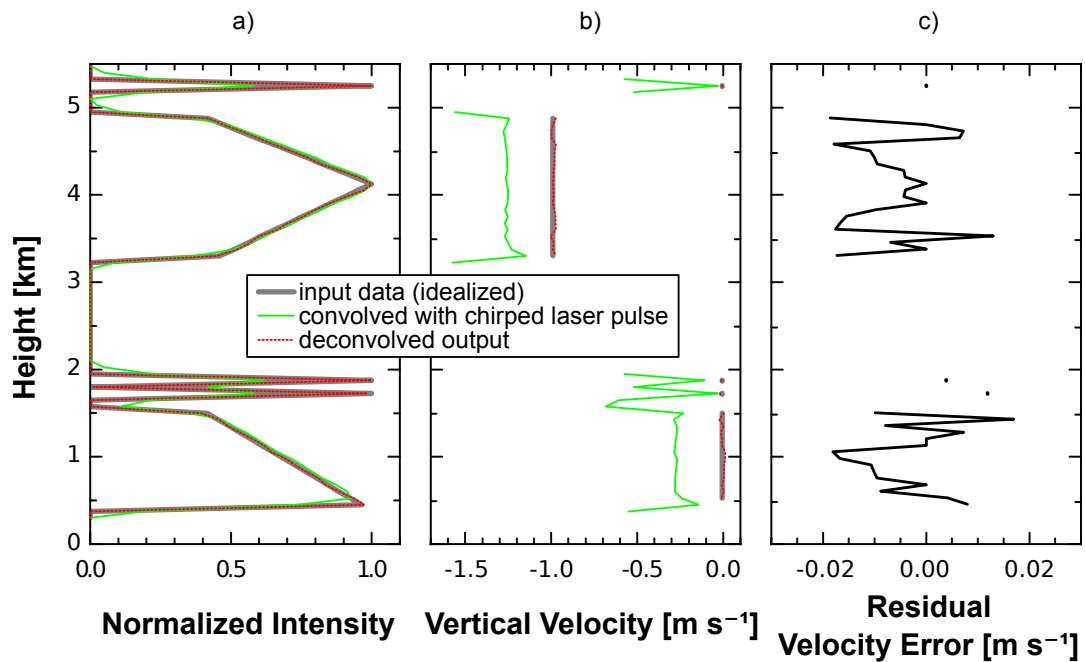


Figure 5.12: Intensities (a) and vertical wind velocities (b) calculated with the evaluation software from the simulated datasets (Fig. 5.11a, b and d). Thick gray lines: idealized input data (Fig. 5.11a), solid green lines: results from the simulated raw spectra (Fig. 5.11b), dotted red lines: results after deconvolution of the simulated spectra with 10 iterations (Fig. 5.11d). Panel (c) shows the difference in the velocity estimation between the idealized input data and the deconvolved spectra. It is visible that the deconvolution removes the chirp effect and that the deviation between the ideal input data and the deconvolved data is less than 0.02 m s^{-1} .

5.1.5 Usage of deconvolution in the scope of this work

The presented deconvolution method enables WiLi to reach a very high velocity accuracy in the range of 0.05 to 0.10 m s^{-1} . The final accuracy is no longer determined by the chirp effect, but by other factors, e.g., the pointing stability of the scanning unit. The deconvolution technique can be applied on stored averaged spectra or in real time during the measurement. Both variants have been implemented in the context of this work. Historical datasets, like that of the SAMUM-2 campaign, were also deconvolved, because averaged spectra had been stored during the operation of WiLi. The method works, even if the shape of the chirp changes over time, and can also be applied in chirp-free cases to simply increase the range and frequency resolution. The RL algorithm has been designed for general purposes and can be used for deconvolution of any dataset, if only a suitable PSF is available. It is worth noting that the algorithm does not require any assumptions about the undisturbed dataset, but only takes available information about the measurement process to remove disturbances. Therefore, the experience with deconvolution operations, gained in the development of the chirp correction, is further used in this work. In Chapter 7, a one-dimensional version of the RL algorithm is applied for the correction of spectral broadening in cloud-radar spectra.

5.2 Cloud-radar data processing

The MIRA-35 cloud radar (see Fig. 5.13) emits electromagnetic pulses with a pulse repetition frequency of 5000 Hz , a wavelength of 8 mm and a pulse length of 300 ns . It records a heterodyne signal by mixing the backscattered radiation with a narrow-band reference wave. Two orthogonally polarized channels are recorded simultaneously. In both channels, the signal processor directly measures and stores the complex amplitude of the incoming radiation for each shot in each range gate. After 256 shots, a Fourier transformation is applied on all stored complex amplitudes of each range gate. In this way, two Fourier spectra are obtained: one co- and one cross-polarized spectrum. Fourier spectra are averaged for 10 s and stored temporarily on harddisk. In this configuration, the velocity resolution is about 0.08 m s^{-1} and the range resolution is about 30 m . The complete signal recording and processing of the MIRA-35 cloud radar system is described by Bauer-Pfundstein and Görzdorf [2007].

From the raw spectra all other cloud radar products are derived:

- Radar reflectivity factor Z : The values in co- and cross channels are quadratically summed up to a total power spectrum. Z is the integral of this spectrum, after noise subtraction, range correction and multiplication with the system constant of the radar.
- Mean velocity v : first moment of the total power spectrum.
- Linear depolarization ratio δ (LDR): ratio of the summed power in the cross- and co-spectra.

These values are stored permanently for each range gate. The averaged raw spectra are compressed by setting all spectral points to zero that fall below a certain noise threshold. This dataset is then run-length compressed and stored permanently. The compression is applied, because the raw spectra consume several hundred Gigabyte of disk space per day. Consequently, only compressed spectra are available for this work, which will play a major role in Chapter 7.



Figure 5.13: MIRA-35 cloud radar (left, in foreground) and WiLi Doppler lidar (right, in background) at TROPOS, Leipzig.

5.3 Linking Doppler lidar and cloud radar

In Section 3.2 the sensitivities of lidar and radar have been compared. The lidar has been found to be superior to the radar in the detection of cloud droplets. When probing the vertical velocity at a cloud base, the movement of the newly created very small droplets indicates the true wind velocity most precisely. The small droplets can be detected with a Doppler lidar, but fall below the detection limit of the cloud radar. Further upward within the cloud, the Doppler lidar beam is attenuated strongly, but the cloud radar can detect the large cloud droplets. In this subsection the vertical-velocity measurements of Doppler lidar and radar are compared at different height levels within a liquid cloud layer.

Figure 5.14 shows an AC cloud which does not show any signs of precipitation. Different levels (marked in the figure with A, B and C) have been chosen for the comparison. The levels are not at the same measurement height for both instruments, because the Doppler lidar signal is attenuated at cloud base, and the values received above cloud base originate from a lower level. They are displayed at cloud top due to the large range-gate size of WiLi. The point-to-point correlation between the vertical velocities observed with Doppler lidar WiLi and the cloud radar is evaluated in Fig. 5.15 for different height levels. The vertical-velocity values of the cloud radar and WiLi are found to be in linear relation for all compared height levels. At the lowest height level A, the vertical-velocity values of the cloud radar are biased towards larger downward velocities. This bias can be explained by a greater influence of large drizzle droplets on the

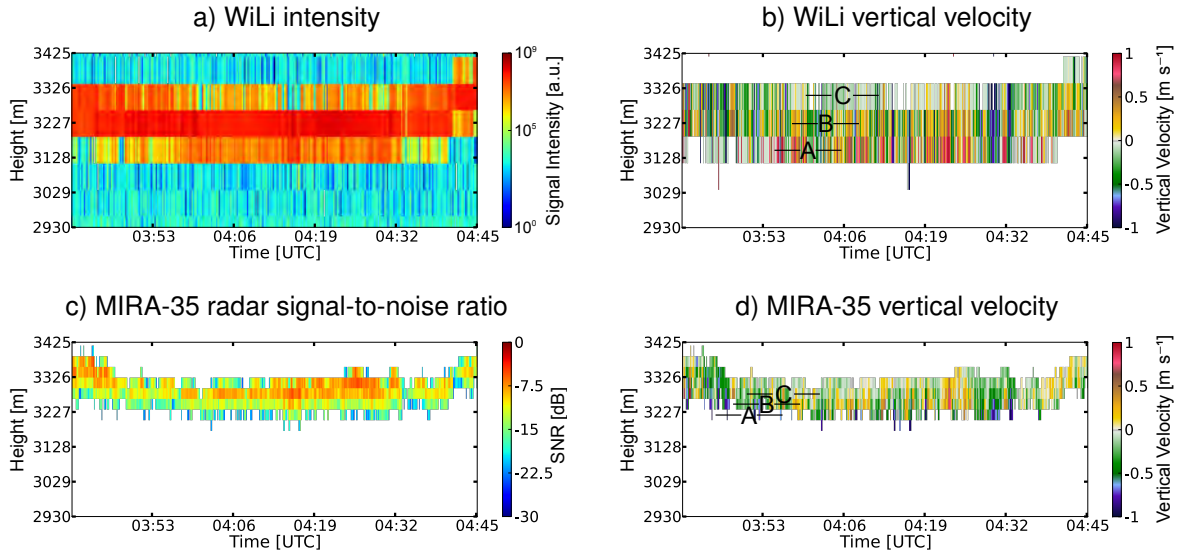


Figure 5.14: Intensity (a) and vertical velocity (b) of Doppler lidar WiLi together with MIRA-35 radar reflectivity (c) and vertical velocity (d) for a short section of an AC cloud recorded at Leipzig on 1 August 2012.

cloud-radar signal at this height level. The slope of the correlation line between the cloud radar and WiLi data is smaller than one at all compared height levels, meaning that the cloud radar shows smaller vertical velocities than WiLi. This difference can occur, e.g, from slightly mismatched height levels, if spherical turbulent structures are assumed. The correlation between the vertical velocities also confirms that the values detected by WiLi above 3300 m height actually originate from a lower level. Some values are detected by the Doppler lidar at the highest level C, because one range gate extends 50% into the neighboring ones and there is no other signal received within the highest range gate. However, the proportionality to the respective values of the cloud radar indicates that the vertical-velocity values of WiLi are independent and actually deliver height-resolved information.

For the same cloud section, the averaged profiles of vertical velocity and signal strength of both WiLi and cloud radar are shown in Fig. 5.16. The gray lines indicate the average of all profiles, while the orange and green lines represent profiles of updrafts and downdrafts, respectively. An average vertical velocity of $\pm 0.1 \text{ m s}^{-1}$ was used as a threshold to sort the profiles into updrafts and downdrafts, respectively. In Fig. 5.16a the averaged signal strengths of both systems is shown, while Fig. 5.16b depicts the average profiles of vertical velocity. WiLi already detects vertical velocities at about 3150 m height, while the radar shows its first measurement value 80 m higher at 3230 m. Above that level, the averaged vertical-velocity profiles of WiLi and the cloud radar agree within about $\pm 0.1 \text{ m s}^{-1}$, i.e, within the measurement accuracy of both systems. In this case, the pointing error is critical, because a tilt would introduce a component of the advection velocity into the measured vertical velocity. A deviation of no more than 0.1° off-zenith is desired. This pointing accuracy is difficult to accomplish, especially for the cloud

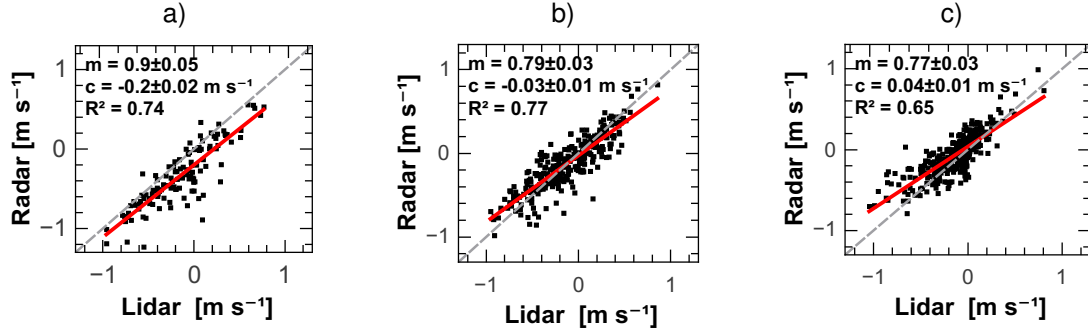


Figure 5.15: Correlation plots for horizontal levels marked in Fig. 5.14. Levels A, B and C correspond to plots (a), (b) and (c), respectively. For the whole one-hour time period, pairs of values from WiLi and cloud radar are plotted. The time resolution of WiLi was reduced to 10 s by averaging of 5 adjacent values to match the time resolution of the cloud radar. A linear function $f(x) = mx + c$ is fitted to each dataset. In panel (a) only sporadic measurements are found in the cloud radar dataset. The existing velocity pairs show the best linearity ($m \approx 0.9$), but they are biased ($c \approx -0.2 \text{ m s}^{-1}$). At height levels B and C the slope is smaller ($m \approx 0.8$) but the bias is very low (within $\pm 0.05 \text{ m s}^{-1}$).

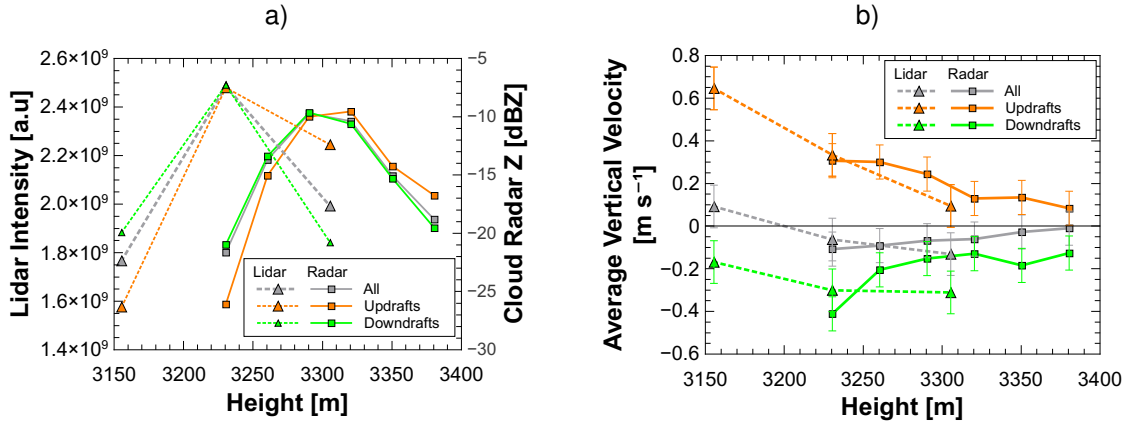


Figure 5.16: Mean Doppler lidar and cloud radar signal (a) and vertical velocity (b) of the cloud section depicted in Fig. 5.14. The averaged values are only shown, if more than 10 values were present in the whole time and height section.

radar, which has only limited means of precision leveling. Hence, it is very pleasing to find both systems in such good agreement. This comparison is essentially enabled by the deconvolution method described in Section 5.1. With the help of this method it is shown here for the first time that height-resolved vertical-velocity information from cloud bases can be derived with Doppler lidar, even with a long pulse length of about 180 m.

5.4 Capabilities of lidar and radar to probe turbulence

The structure of layered clouds is the result of turbulent motion inside the cloud layer. Sources of turbulent motion can be, e.g., wind shear, radiative cooling at cloud top or gravity waves. Energy introduced into the system leads to the development of large eddies, which consecutively break down into many smaller eddies. This process dissipates the turbulent energy towards smaller and smaller sizes eventually reaching the molecular level, where energy is converted from mechanical energy into heat. Kolmogorov [1941] proposed that the power spectrum of turbulent energy dissipation is given by

$$E(k) = C\epsilon^{\frac{2}{3}}k^{-\frac{5}{3}}. \quad (5.5)$$

$E(k)$ is the energy per unit volume, $C \approx 0.5$ the Kolmogorov constant, ϵ the energy dissipation rate and $k = \frac{2\pi}{\Lambda}$ the wavenumber (with Λ the corresponding structure size). The variance of one velocity component within this turbulent field is

$$\sigma^2 = \int_0^\infty E(k) dk, \quad (5.6)$$

with the standard deviation σ .

Usually, layered clouds are embedded into a turbulent layer, topped by an inversion layer. This inversion restricts the maximum size of the turbulent eddies. Only eddies with a size Λ smaller than two times the layer depth d_l can move freely. The wavenumber at which turbulent motion becomes visible in the energy spectrum is hence $k_l = \pi/d_l$.

In Fig. 5.17 turbulent-energy spectra of the AC cloud from Fig. 5.14 are depicted. The spectra were calculated from the vertical velocities measured with WiLi and the cloud radar at height level B in Fig. 5.14. The transition from time to spatial frequencies was made by application of Taylor's hypothesis [Taylor, 1938], which assumes $k = \frac{2\pi}{u_a} f$. The mean advection speed u_a at cloud base has been taken from the GDAS dataset. The bold lines in Fig. 5.17 are smoothed versions of the corresponding energy spectra. The energy spectrum of the cloud radar is smaller than that of WiLi by a constant factor. This difference can, again, be explained by a non-perfect match in height levels. However, the shapes of the averaged curves are similar, meaning that the cloud radar and WiLi show the same frequency response below an integration time of 10 s.

With the help of this description, the capabilities of Doppler lidar and cloud radar for measuring turbulent motion within cloud layers can be estimated. For that purpose, a model of a simple energy spectrum is used: For spatial frequencies $k < k_l$ let the energy be constant at $E_0 \stackrel{!}{=} C\epsilon^{\frac{2}{3}}k_l^{-\frac{5}{3}}$, for $k > k_l$ the energy spectrum is assumed to be proportional to $k^{-\frac{5}{3}}$. Continuity is demanded at k_l . These assumptions reproduce energy spectra similar to those depicted in Fig. 5.17, but without noise, and Eq. (5.6) can be solved analytically:

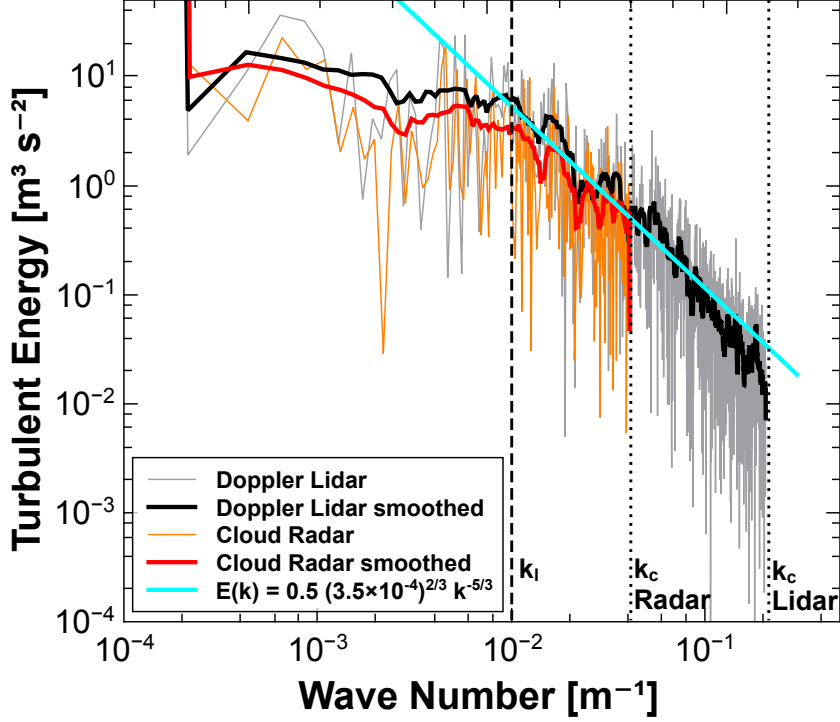


Figure 5.17: Comparison between the turbulent energy spectra of Doppler lidar and cloud radar. The advection speed taken from the GDAS dataset is $u_a = 7.5 \text{ m s}^{-1}$. The characteristic wavenumber is found to be $k_l = 0.01 \text{ m}^{-1}$. Standard deviations are $\sigma_L = 0.39 \text{ m s}^{-1}$ for WiLi and $\sigma_R = 0.28 \text{ m s}^{-1}$ for the cloud radar. The blue curve indicates the energy spectrum for a dissipation rate of $\epsilon = 3.5 \times 10^{-4} \text{ m}^2 \text{ s}^{-3}$ and $C = 0.5$.

$$\sigma^2 = C \epsilon^{\frac{2}{3}} \left(k_l^{-\frac{5}{3}} \int_0^{k_l} dk + \int_{k_l}^{k_c} k^{-\frac{5}{3}} dk \right) \quad (5.7)$$

$$= C \epsilon^{\frac{2}{3}} \left(\frac{5}{2} k_l^{-\frac{2}{3}} - \frac{3}{2} k_c^{-\frac{2}{3}} \right). \quad (5.8)$$

$k_c = \frac{\pi}{\Lambda_c} = \frac{\pi}{\Delta t u_a}$ is the cut-off wavenumber, which depends on the advection speed and the measurement interval Δt . For an ideal measurement system $\Delta t \rightarrow 0$ and consequently $k_c^{-\frac{2}{3}} \rightarrow 0$. In Table 5.1 values for the standard deviation σ and the corresponding variance σ^2 are shown, which have been calculated with Eq. (5.8). The numeric values of $C \times \epsilon$ and k_l have been taken from the real measurement of Fig. 5.17. Whilst the standard deviation gives a direct impression of the order of magnitude of the vertical-velocity values, the variance is a measure for the turbulent kinetic energy (TKE). These calculations isolate the effect of time resolution. The values of variance and standard deviation are also proportional to the strength of the recorded vertical-velocity values. Therefore, variance and standard-deviations for the cloud radar are overestimated, because it detects slightly lower vertical-velocity values and, hence, a smaller energy-dissipation rate

Table 5.1: Estimation of vertical-velocity standard deviation and variance, detected by different measurement systems. $u_a = 7.5 \text{ m s}^{-1}$ and $k_l = 0.01 \text{ m}^{-1}$, like for the cloud spectrum presented in Fig. 5.17.

Parameter	Δt	k_c	σ	$\sigma/\sigma_{\text{ideal}}$	σ^2	$\sigma^2/\sigma_{\text{ideal}}^2$
Unit	s	m^{-1}	m s^{-1}	%	$\text{m}^2 \text{s}^{-2}$	%
Cloud radar	10.00	0.04	0.33	79.59	0.11	63.35
WiLi (SAMUM-2)	5.00	0.08	0.36	87.70	0.13	76.91
WiLi (UDINE)	2.00	0.21	0.38	93.52	0.15	87.46
Ideal System	0	∞	0.41	100.00	0.17	100.00

(see Fig. 5.17).

Table 5.1 shows that WiLi comes closest to the ideal system with a measurement interval of 2 s. The vertical-velocity standard deviation measured by the cloud radar is only 12% smaller than the one of an ideal system. Hence, the smaller time resolution of the cloud radar has a limited impact on the total standard deviation. However, the cloud radar is mostly missing the spatial frequencies in the inertial subrange, which have decisive impact on the single vertical-wind values. Up- or downdraft events short in time will be missed. The cloud shown in Fig. 5.17 was moving with an advection speed of 7.5 m s^{-1} . Later, in Section 6.1, it is shown that the layered clouds under study in this work move with an average advection speed of 13 m s^{-1} . If the same conditions are assumed as in Table 5.1, but an advection speed of 20 m s^{-1} , the cloud radar's cut-off wavenumber would be $1.5 \times 10^{-2} \text{ m}^{-1}$. In that case, it would resolve about 55% of the TKE and miss the dissipation range completely. WiLi would resolve 72% and partly cover the inertial subrange, which would allow the measurement of the energy dissipation rate [O'Connor et al., 2010].

WiLi has deficits at high wavenumbers that result from the relatively large range gate size of 75 m and the pulse length of 180 m. Some of the small turbulent eddies within this range will cancel out and let the spectrum slightly drop below the $-5/3$ -slope (see Fig. 5.17). For a measurement interval as low as 2 s a similar effect would also be expected for the cloud radar. In a measurement height of 5000 m, the MIRA-35 cloud radar has a beam width of about 50 m. For a given advection speed $u_a \approx 13 \text{ m s}^{-1}$ turbulent motion will be smoothed out during one measurement due to cancellation effects in the lateral direction. Hence, the measurement interval of both systems cannot be reduced arbitrarily, even if signal strength would allow it.

5.5 Combined observations with Doppler lidar, cloud radar and wind profiler

Lidars and cloud radars can only measure vertical velocity, if a sufficient number of aerosol particles, cloud droplets or ice crystals are present in the target volume. Under clear-air conditions, no velocity information at all can be derived, but the movement

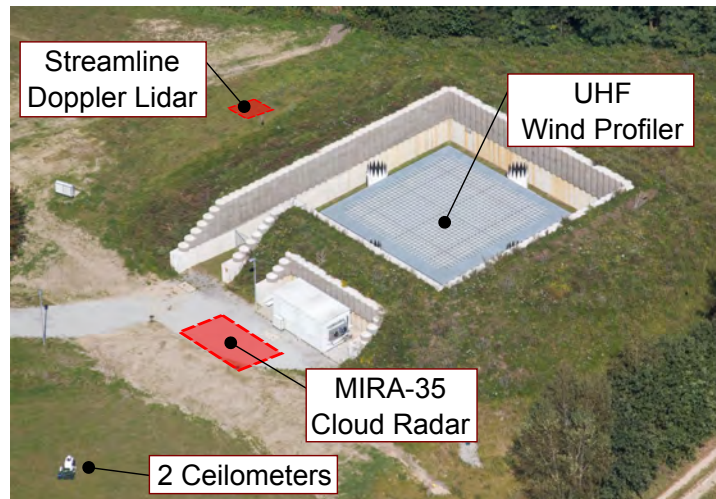


Figure 5.18: Aerial view of the wind profiler site at MOL (Image Credit: DWD). The photograph was taken in September 2011. In the meantime a Streamline Doppler lidar and a MIRA-35 cloud radar were deployed next to the wind profiler (red areas).

of clear air is actually an important measurement quantity. Large-scale atmospheric motion (e.g., gravity waves) can influence a cloud decisively, and falling droplets or ice crystals are slowed down or accelerated by vertical air movements.

Wind-profiler radars have been designed to measure the movement of the clear air. While the radar technique itself is nearly 70 years old, the wind profiler technique has been developed not before the late 1970s [Strauch et al., 1984; Weber and Wuertz, 1990]. A wind profiler exploits Bragg scattering at atmospheric density fluctuations to produce a backscatter signal even under clear-air conditions. Rayleigh scattering from particles also adds to the signal, but as the efficiency of Rayleigh and Bragg scattering is proportional to λ^{-4} and $\lambda^{-\frac{1}{3}}$, respectively, Bragg scattering dominates more and more for longer wavelengths.

The distribution of powerful wind profilers is limited, but they can actually deliver the desperately needed information about the velocity of clear air. They can only be operated by a limited number of well-funded institutions, due to their high operational costs. The DWD operates an ultra-high frequency (UHF) wind profiler at MOL (see Fig. 5.18). It works at 482 MHz and can deliver wind information from 0.5 km to 10 km height with a range resolution of 150 m, a measurement interval of about 10 s and a velocity resolution of about 0.1 m s^{-1} [Böhme et al., 2004]. The distance between two neighboring range gates is 94 m due to range interpolation.

5.5.1 Combined observation strategy and case studies

In the context of this work, a cooperation between MOL and TROPOS has been established in July 2013. Combined measurements of the vertical velocity were carried out simultaneously with the wind profiler, the Streamline Doppler lidar and the MIRA-35 cloud radar at MOL. To avoid misunderstandings between the LACROS and MOL

Table 5.2: MOL instrumentation utilized in the experiment.

Designation	MOL Doppler lidar	Wind profiler	MOL cloud radar
System type	HALO Streamline Doppler lidar	UHF wind profiler	MIRA-35 cloud radar
Wavelength	1.5 μm	0.6 m	8.3 mm
Range gate length	50 m	94 m	30 m
Integration time	2 s	10 s	10 s
Receiver field of view	0.05 mrad	50 mrad	10 mrad
Pulse repetition rate	10 kHz	12.5 kHz	5 kHz
Average emitted power	0.2 W	200 W	30 W

instruments, the Streamline Doppler lidar and the MIRA-35 cloud radar of MOL are designated MOL Doppler lidar and MOL cloud radar in the context of this work. Operational parameters of the systems measuring vertical velocity can be found in Table 5.2. All systems were co-located within a 30-m radius (see Fig. 5.18) and had therefore overlapping observation volumes. In normal operation the phased-array antenna of the wind profiler is used to derive the height-resolved horizontal wind with a digital beam-swinging technique. For the duration of the combined measurements, MOL Doppler lidar, MOL cloud radar and the wind profiler were used in a vertical-stare mode. No scanning at all was involved in this project. A schematic representation of the observation volumes is given in Fig. 5.19 illustrating the big technical differences between the three systems. The measurements were carried out by Ronny Leinweber, Ulrich G6rsdorf and Volker Lehmann of MOL, the data evaluation was done at TROPOS. In the following, two example cases are presented that demonstrate the capabilities of combined measurements of Doppler lidar, cloud radar and wind profiler.

5.5.1.1 Vertical-velocity feature classification during warm-cloud event

In Fig. 5.20 the vertical velocities measured by the different systems at Lindenberg on 30 July 2013 are shown. It is clearly visible from Fig. 5.20c that the air around the approaching cloud system is in strong vertical motion, with up- and downdrafts on the order of $\pm 1 \text{ m s}^{-1}$. The thin cloud from 11:00 to 11:15 UTC at 2900 m is clearly embedded in a large updraft region. The vertical-velocity pattern within this cloud compares well between all engaged measurement systems. The wind profiler even shows updrafts within the precipitation of the cloud system approaching at 11:30 UTC. Fig. 5.20d shows the FWHM of the wind-profiler spectral width. When comparing Fig. 5.20b and 5.20d, it is obvious that the wind profiler signal is broadened by small-scale turbulence (visible, e.g., at cloud tops) and by Rayleigh scattering at large particles (e.g., at around 12:00 UTC). A collection of vertical-velocity features, detected in this combined measurement, is shown in Fig. 5.20e. The figure shows that the combination of the three instruments is a unique way to coherently resolve and identify the different types of vertical motion in the troposphere.

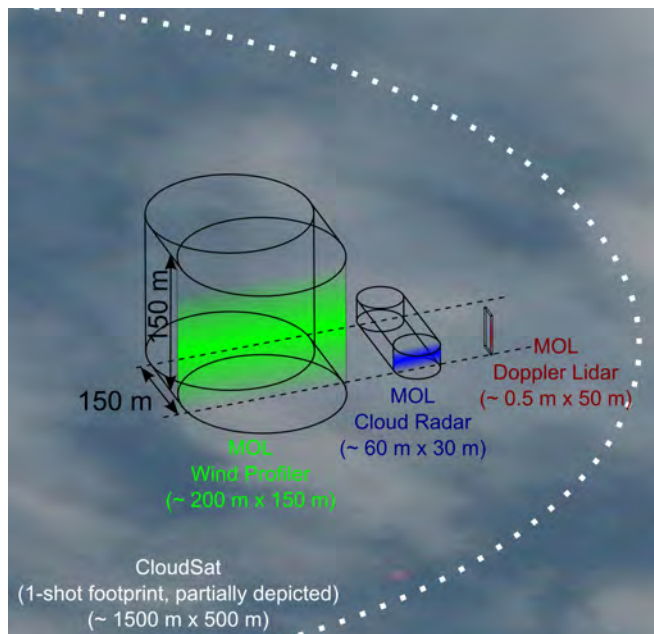


Figure 5.19: Comparison of observation volumina of MOL Doppler lidar (red), MOL cloud radar (blue) and wind profiler (green). Beam diameter times folded pulse length is given in brackets below the system names. The length interval of 150 m, indicated by two dashed lines, is the displacement of the cloud during an integration time of 10 s, when moving with an advection speed of $u_a = 15 \text{ m s}^{-1}$. In the background, a representation to scale of the AC cloud from Fig. 4.3 is shown. In this figure, the observation volumina are shown next to each other. In reality, the observation volumina of cloud radar and Doppler lidar overlap from about 1000 m height upwards. One pulse of the wind profiler fills a factor of $10^4 \dots 10^5$ more space than the Doppler lidar. For comparison, the CPR on CloudSat has a single-shot footprint of about 1500 m (partially depicted) at a vertical resolution of about 500 m (not depicted). The smaller observation volumina are one of the biggest advantages of ground-based platforms compared with satellite systems.

A magnified portion of the updraft structure between 11:00 and 11:15 UTC from Fig. 5.20 is shown in Fig. 5.21. A liquid-water cloud forms within the updraft structure, but also in the downdraft regions signals are visible in the Doppler lidar measurements. Where cloud droplets are present, the imprint of the updraft structure can be seen in the MOL Doppler lidar (Fig. 5.21a) and partly in the MOL cloud-radar observations (Fig. 5.21b). In Fig. 5.21a it is visible that the MOL Doppler lidar also has a chirped laser pulse. Chirp-induced artifacts are visible as artificial negative vertical velocities at cloud top and cloud bottom (black dotted box). The values at cloud top and cloud base are shifted by about -0.3 m s^{-1} , compared with the central value. Unfortunately, the datasets presented here cannot be chirp-corrected with the method described in Section 5.1, because the MOL Doppler lidar was not set up to store the pulse spectra at the time of these measurements. At the present state of development the storage of laser-pulse spectra is technically not possible for this kind of Doppler lidar [METEK company, personal communication].

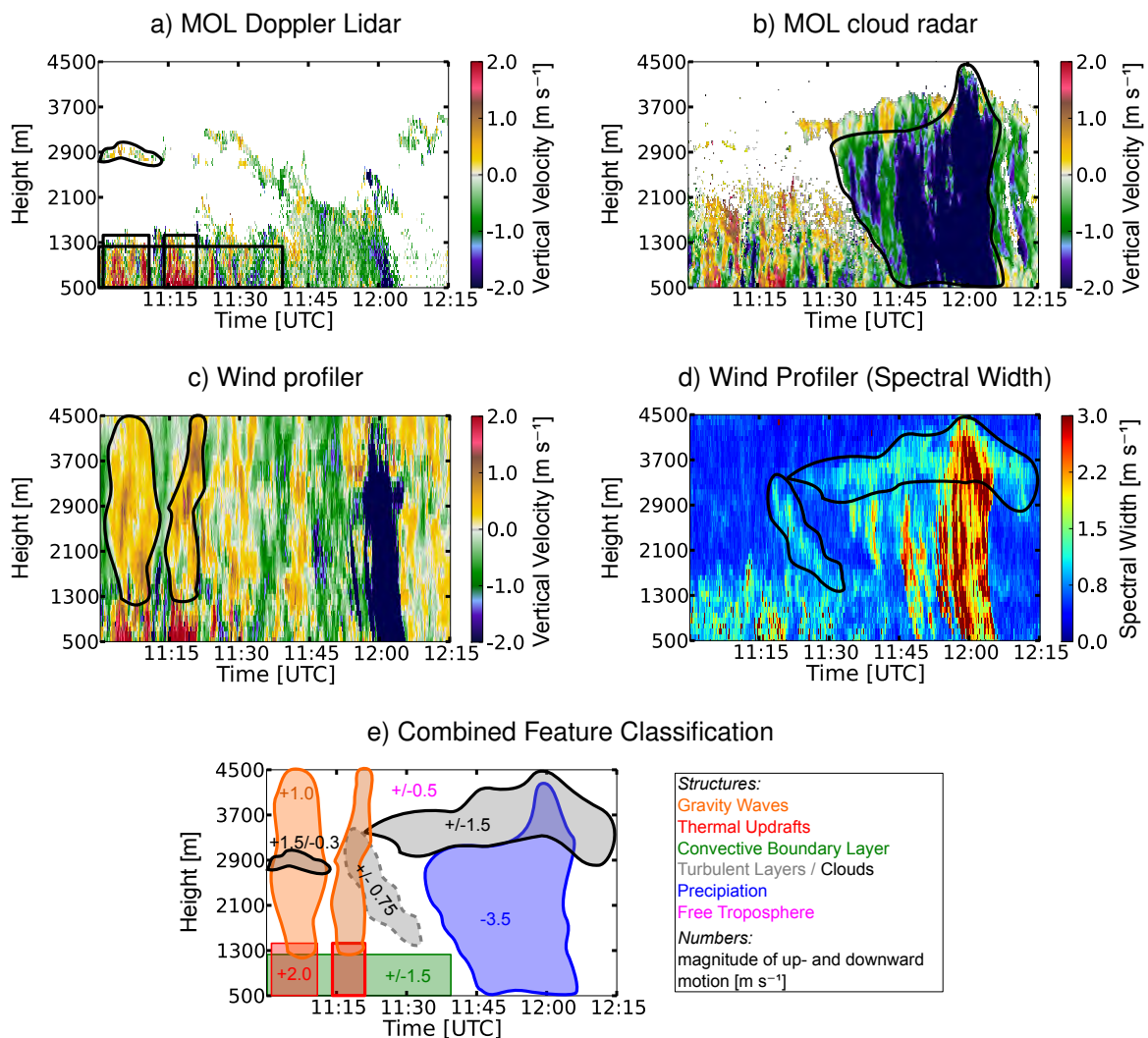


Figure 5.20: Overview about the vertical velocity measured by the different systems of MOL at Lindenberg, Germany on 30 July 2013, 11:00–12:15 UTC. Features, unique for each instrument, are marked in a) to d). MOL Doppler lidar (a) shows the turbulent boundary layer and cloud bases. MOL cloud radar mainly detects clouds and precipitation. The wind profiler delivers information about vertical-wind structures (c) and the spectral broadening (d) in the free troposphere. The detected vertical-wind features are collected in (e). Around 12:00 UTC it is visible that Rayleigh scattering at rain droplets becomes strong enough to dominate the signal of the wind profiler.

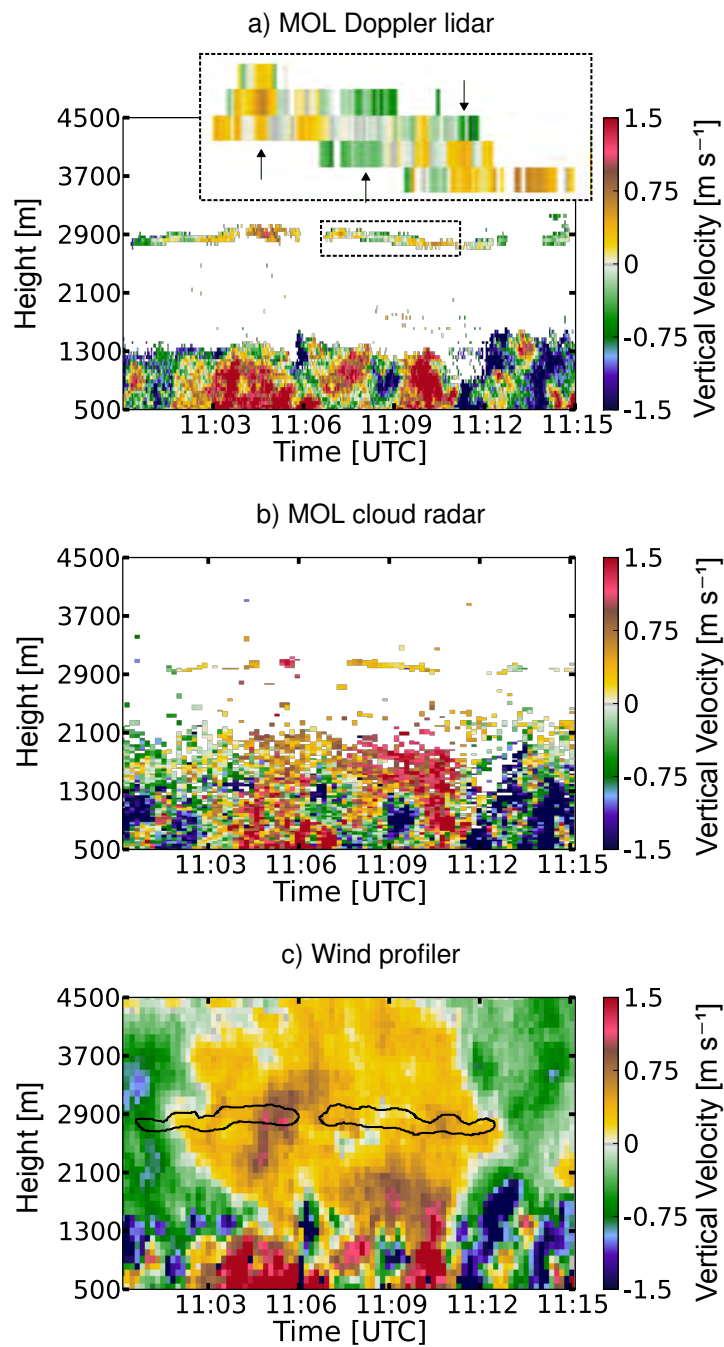


Figure 5.21: Magnified portion of Fig. 5.20 (11:00-11:15 UTC). The wind profiler (c) gives unambiguous information about the vertical velocity of air in the vicinity of the cloud, which is detected by the MOL Doppler lidar (a) and partly by the MOL cloud radar (b). The dotted box in (a) marks a time period during which the MOL Doppler lidar shows chirp-induced artifacts (negative vertical velocities) at cloud base and cloud top (see Fig. 5.7 for comparison).

5.5.1.2 Removing the vertical-velocity bias from the terminal fall velocity in a mixed-phase cloud

A special benefit of the wind profiler measurements is the possibility to derive unbiased terminal fall velocities of droplets and ice crystals. In Fig. 5.22 a combined vertical-velocity measurement from 25 September 2013 is shown. Particles in the virga can be found to move upwards at 3700 m height around 10:09 UTC in the MOL cloud radar and at around 10:17 UTC in the MOL Doppler lidar. After subtraction of the vertical velocities measured by the wind profiler at the corresponding time and height interval,

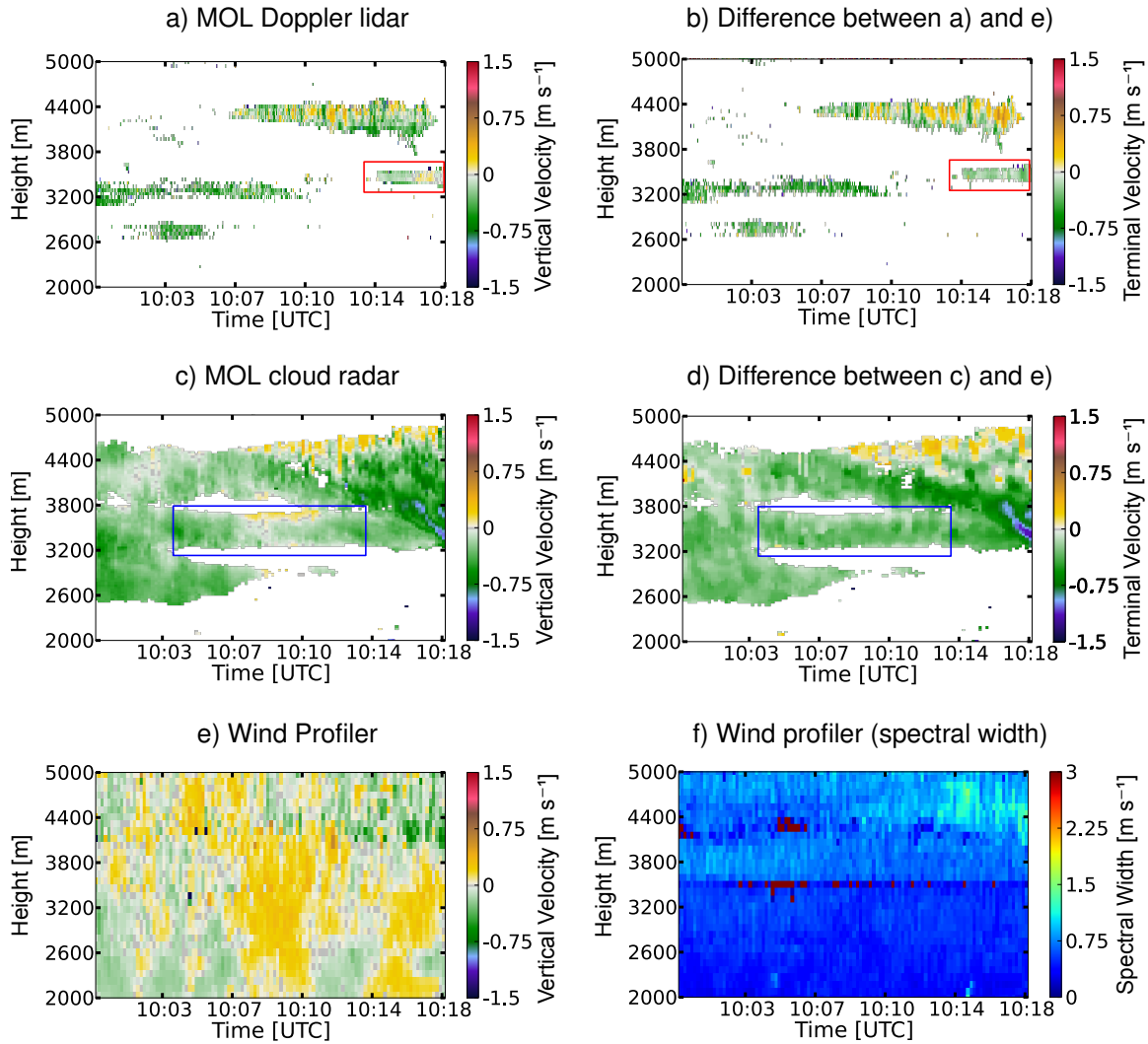


Figure 5.22: Demonstration of terminal-fall-velocity correction within the virga of an ice-producing layered cloud over Lindenberg, Germany on 25 September 2013, 10:00–10:18 UTC. A nearest-neighbor interpolation of the wind-profiler data was used in the subtraction process. In Fig. 5.23 the histograms of vertical velocities in the sections marked by red and blue boxes are presented. The subtraction may be invalid in the turbulent layers, because the wind profiler does not have sufficient spatial and temporal resolution to resolve the fast turbulent motion directly.

the true fall velocity of the particles relative to the air becomes visible. The histograms of the sections within the red boxes in Fig. 5.22 are shown in Fig. 5.23. The suppression of unrealistic positive values can be seen between the untreated (left column) and corrected vertical velocities (right column).

In Section 3.2.4, it was shown that the size of a particle can be computed, if its terminal fall velocity is known and a basic particle classification can be done. However, from Fig. 3.4 it becomes obvious that the uncertainty in derived particle size is large even for a relatively small error in terminal fall velocity. The assumption of a population of

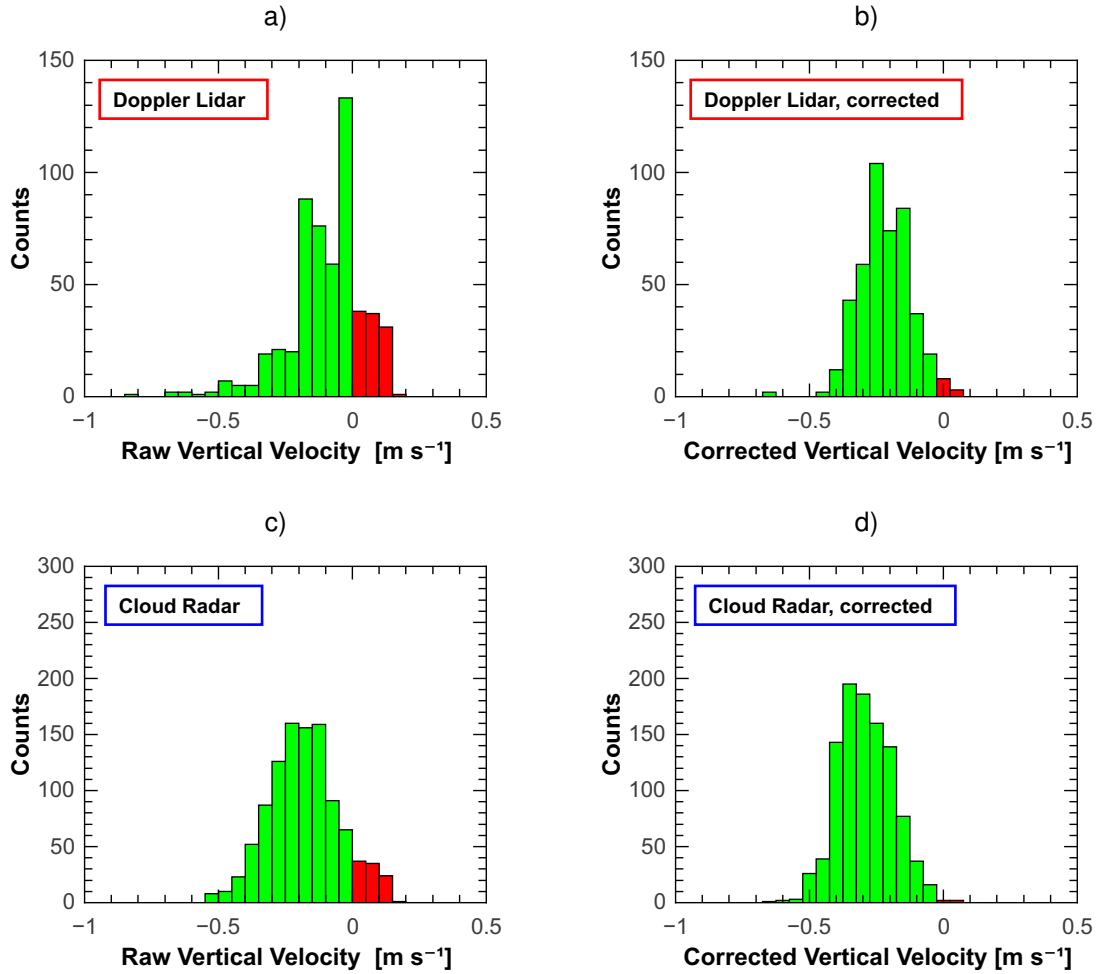


Figure 5.23: Retrieval of the true terminal fall velocity of ice particles from the cloud virga marked in Fig. 5.22 with red and blue squares. Upward motion is shown with red bars, downward motion with green ones. The original datasets of MOL Doppler lidar (a) and MOL cloud radar (c) show a large portion of particles moving upwards. After the time and height-resolved subtraction of the wind-profiler vertical velocities, a considerable lower number of measurement values of lidar (b) and radar (c) indicate upward motion. A 3×3 median filter was applied on the corrected radar data for reduction of strong interpolation noise. For a meaningful comparison the same filter was applied on the raw vertical-wind signals. Hence, the effective time resolution of both datasets is reduced to 30 s for this comparison.

hexagonal columns with a terminal velocity of $v_t = 0.5 \pm 0.1 \text{ m s}^{-1}$ leads to a maximum particle diameter between 300 and 500 μm . With $v_t = 0.5 \pm 0.2 \text{ m s}^{-1}$ the possible particle size range already spreads from 200 to 600 μm .

The uncertainty of $\pm 0.1 \text{ m s}^{-1}$ is within the uncertainty of Doppler lidar and cloud radar systems, but as long as the vertical movement of the air is not known, the measured vertical velocity does not yield useful information about particle size or shape.

5.5.2 Interpretation of first results and next steps

The combined vertical-velocity measurements yield unique information about the movements of small and big particles together with the true movement of the air. The use of a wind profiler can fill the white spaces left on the vertical-velocity picture drawn by Doppler lidars and cloud radars. Large-scale atmospheric motion becomes visible and the extent and strengths of vertical-velocity fields can be studied independent of the presence of tracers, like aerosol particles or cloud droplets. One can see, e.g., from Fig. 5.22 that vertical air movements in the free troposphere can strongly bias fall velocities measured by Doppler lidar or cloud radar and that this bias can be reduced with the help of a wind profiler. If all vertical-velocity measurements can be connected properly, it may be possible to derive size and shape information directly from particle fall velocity. Such an approach is presented in Chapter 7.

The ambiguity between Rayleigh and Bragg scattering in the presence of large particles poses problems by broadening the wind profiler's spectral peak and possibly shifting the measured vertical velocity. However, it may be possible to calculate a wind-profiler Rayleigh spectrum from the MIRA-35 spectra to better isolate the Bragg peak. The technique has already been established for a 3-GHz radar by Gage et al. [1999]. The MIRA-35 cloud radar has at all heights a smaller observation volume, higher spectral resolution and a better sensitivity towards liquid and ice particles than the wind profiler. The approach of Gage et al. [1999] should therefore also be feasible for this combination.

6 Vertical-velocity and glaciation statistics of mid-latitude and sub-tropical layered clouds

Mixed-phase layered clouds appear all over the globe under very different conditions [e.g., Zhang et al., 2010a]. Their climatology has been studied before [Seifert et al., 2010; Riihimaki et al., 2012], but detailed information about vertical-velocity statistics in these cloudy environments is still absent. The unique combination of instruments within LACROS is used here us to obtain new datasets of this important cloud type.

In Section 6.1, the scopes of the UDINE and SAMUM campaigns are briefly discussed and an overview is given about the cloud cases that were selected from the UDINE and SAMUM-2 datasets. Two exemplary cloud cases from the UDINE campaign are presented in Section 6.2. These two cases demonstrate, how selected clouds were classified into mixed-phase or liquid clouds and how microphysical quantities such as IWC or LWC were derived. In Section 6.3, the freezing behavior of clouds over Leipzig is studied. The results compare well with recent observations from CloudSat/CALIPSO, but deviate strongly from former studies of TROPOS. A lidar ice detection threshold is introduced in order to harmonize the results. IWC and LWC derived from the Cloudnet observations at Leipzig are then applied in Section 6.4 to further quantify the ratio between ice and water mass in mixed-phase layered clouds over Leipzig. The precise knowledge about the freezing state (mixed-phase or liquid) of the cloud layers is used in Section 6.5, where the vertical velocities at cloud bases are evaluated. Measurements from Doppler lidar and cloud radar are presented and compared. In this context, the influence of falling particles on the vertical-velocity measurements at cloud base is, for the first time, compared between Doppler lidar and cloud radar. The combination of both instruments allows the isolation of the effects of falling particles on the measurements. Based on this knowledge, vertical-velocity statistics are compared between the mid-litudinal (UDINE) and sub-tropical climate zones (SAMUM-2).

6.1 Overview about UDINE and SAMUM campaigns

The two measurement campaigns SAMUM-1 and SAMUM-2 were conducted in the years 2006 and 2008, respectively (see Ansmann et al. [2011] for an overview). The main scientific goal was to understand, how mineral dust is transported from a its source (SAMUM-1) over the Atlantic to Europe or North America (SAMUM-2). During SAMUM-2, TROPOS established a lidar observation site at Praia International Airport

and did continuous measurements with the multiwavelength/Raman/polarization lidar BERTHA (Backscatter Extinction lidar–Ratio Temperature Humidity profiling Apparatus, see Althausen et al. [2000]) and the Doppler lidar WiLi in January, February, May and June 2008. The resulting combined dataset was re-evaluated in the context of this work, focusing on the statistics of vertical velocities in layered clouds. The elastic-backscatter channels of BERTHA were used to identify layered clouds. The depolarization channels were employed to decide between precipitating ice and water particles below the cloud layers and, thus, between liquid and mixed-phase clouds. WiLi delivered the vertical velocities at cloud bases. The vertical-velocity measurements were interrupted by conical scans, which are left out in this analysis. In the context of this work, this dataset was compared with the UDINE measurements to contrast the behavior of liquid- and mixed-phase layered clouds in the sub-tropics and the mid-latitudes. Such observations are not present in the literature until now.

From 2010 to 2013, the UDINE campaign was carried out at TROPOS, Leipzig. The location of Leipzig makes it possible to study marine and continental air masses and, thus, to acquire cloud-base vertical-velocity statistics, which may be representative for the whole mid-latitudes. The vertical-velocity measurements were assisted by the EARLINET [Wandinger et al., 2004; Pappalardo et al., 2014] lidar MARTHA, equipped with multiple fields of view [Schmidt et al., 2013], and during two time periods by the mobile PollyXT Raman lidar. Just in time for the campaign, the cloud radar and the HATPRO radiometer were obtained by TROPOS in August 2011. This additional equipment enabled the participation in Cloudnet [Illingworth et al., 2007], which has greatly served the UDINE campaign with its automatically provided micro- and macrophysical cloud products (e.g., IWC/LWC, drizzle detection and simple target classifications).

From the UDINE and the SAMUM-2 datasets, a number of cloud cases were selected. The cloud-selection criteria comprise the absence of low-level cloud cover, a variation in cloud base height (CBH) smaller than 1000 m and a maximum vertical extent of the liquid cloud layer of 500 m. Potential precipitation in the virga had to be clearly linked to the cloud under investigation. Seeding from higher-level clouds could, e.g., be identified by the cloud radar (UDINE only). Additional liquid layers below the cloud could be discriminated from precipitation, because of the strong lidar attenuation and/or by the vertical-wind velocity characteristics within these layers (alternating up- and downdrafts). Drizzle and rain were identified by terminal fall velocity and lidar/radar depolarization ratio. Cloud top height (CTH) was measured, if the cloud top layer was detected by the cloud radar. Mainly for high-altitude cases, this was usually not the case and the CTH was estimated from the lidar measurements by adding to the CBH 300 m, which is the mean thickness of all cloud top layers that were detected by the cloud radar. An overview about 417 cloud cases selected from the UDINE dataset is given in Fig. 6.1. In 352 cases, Cloudnet was operational. 283 cases were acquired with WiLi. In 218 cases, WiLi and Cloudnet measured together, 168 of them were identified as supercooled clouds. The measurements were supported by PollyXT or MARTHA in 177 cases. From the SAMUM-2 dataset, 76 cloud layers were selected. The average length of a cloud case is 1.7 hours.

In the context of this work, some technical upgrades were added to the WiLi system

to include it in LACROS: A new software system, remotely controllable hardware and new laser components were implemented until Summer 2011. These technical updates allowed for faster reaction times, continuous, unattended measurements and a shorter measurement time interval of 2 s due to the higher available laser power. The gain in technical capabilities is also visible in Fig. 6.1 as an increase of collected cloud cases over time. Also a seasonal variability in the occurrence frequency of layered clouds is visible, with a higher rate of selected cloud cases in the second half of the year.

The occurrence statistics of all cloud layers measured during both SAMUM-2 and UDINE campaigns is shown in Fig. 6.2. The cloud top temperatures (CTT) in both datasets mainly lie between 240 and 280 K. This temperature range compares well with existing measurements of the CALIPSO and CloudSat satellites [Zhang et al., 2010a]. The height occurrence is shifted by about 2000 m between the sub-tropics (SAMUM-2) and the mid-latitudes (UDINE), because of different average ground temperatures. The occurrence frequency is about 20 cloud layers per month for the sub-tropics and 17 per month for the mid-latitudes, if the whole SAMUM-2 period and the intensive measurement phase of UDINE between 2011 and 2013 are taken into account. The real occurrence frequency of layered clouds may have been higher, because not all cases passed the selection criteria.

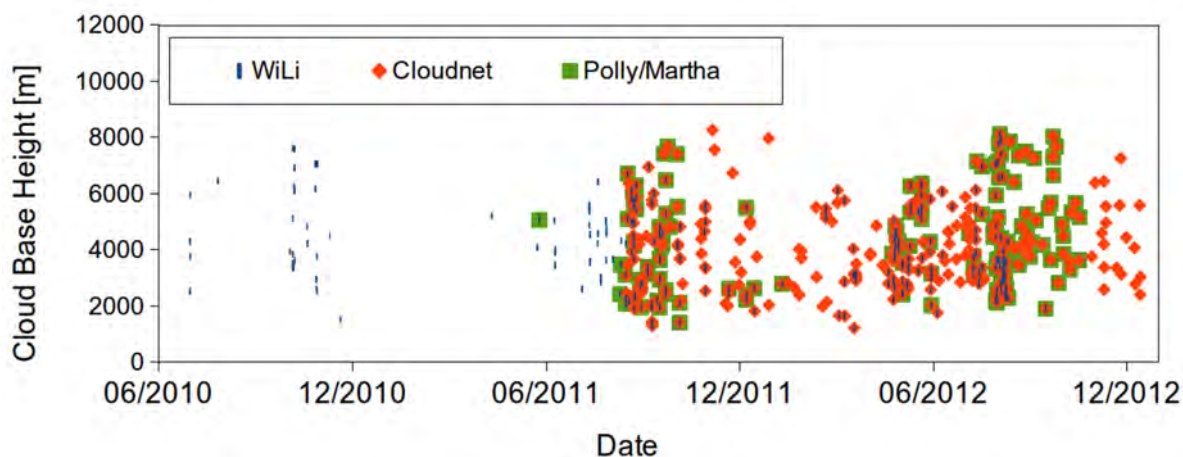


Figure 6.1: Overview about time of occurrence and base height of all selected cloud cases acquired during the UDINE campaign from June 2010 to January 2013. In 2010, mainly technical development of WiLi was done. The main measurement phase started with the establishment of Cloudnet in August 2011. The increased seasonal occurrence of layered clouds in mid-latitudes is visible in each year from June to November. The increase in recorded cases from August 2011 on is due to increased automation of the Doppler lidar WiLi, installation of the new MIRA-35 cloud radar and the establishment of Cloudnet at TROPOS.

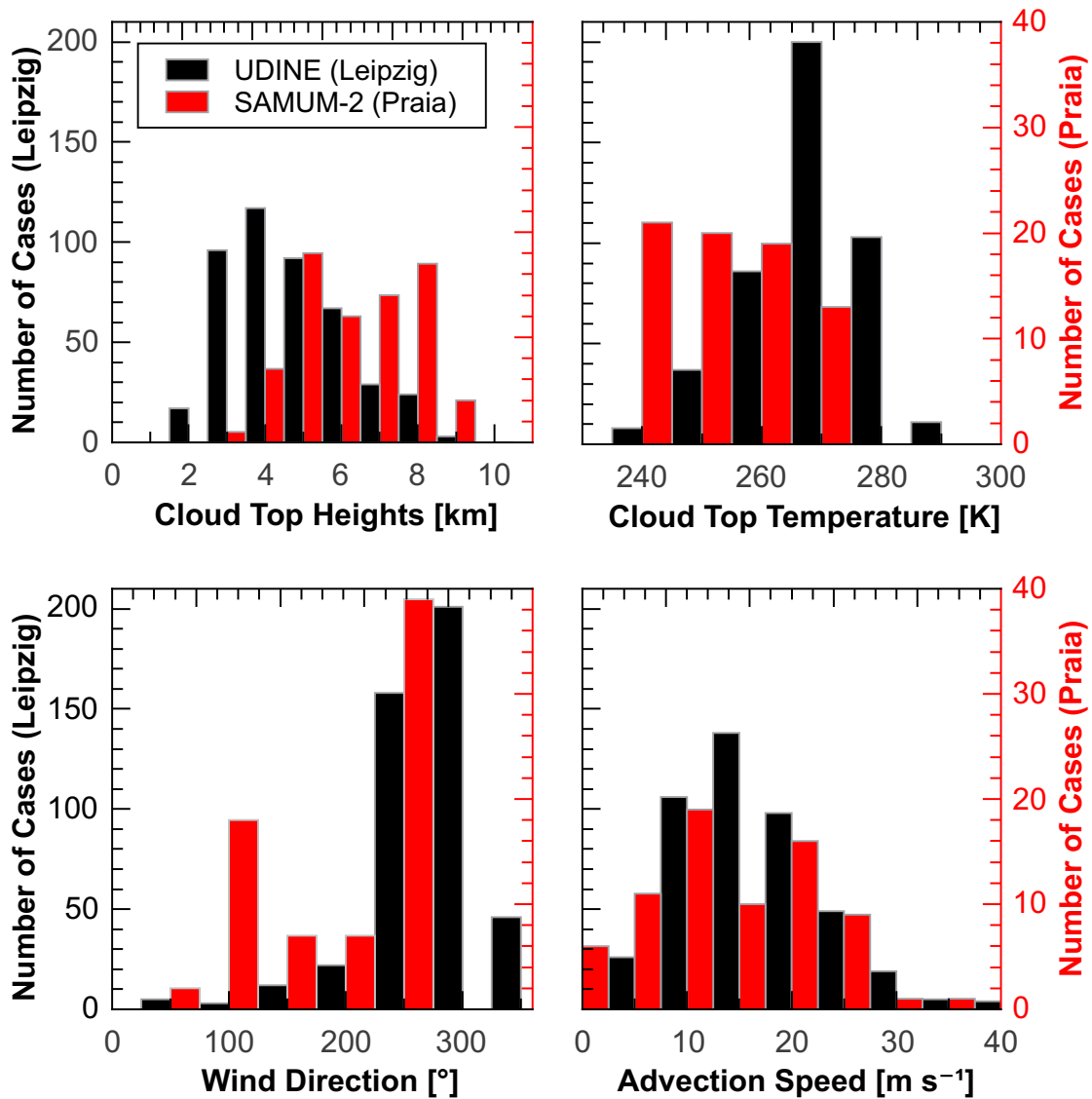


Figure 6.2: Histograms of the basic meteorological parameters at cloud top of all cases from the SAMUM-2 and UDINE campaigns considered in this work. Cloud top heights were measured, if the cloud radar was available, or estimated, if the cloud radar did not detect the cloud top layer. Temperatures, meteorological wind directions and wind speeds were derived from the GDAS reanalysis dataset at cloud top height. Corresponding vertical-wind statistics are given in Section 6.5.

6.2 Case studies from UDINE

In the following, two case studies are presented to show the synergies between lidar and radar in the measurement of layered clouds. The use of the cloud classification scheme introduced in Section 4.5 is exemplified and the retrieval of microphysical quantities like IWC and LWC is demonstrated. The first case represents a cloud in which ice production is very low and lidar does not detect any ice. In the second case, ice crystals are detected by both lidar and radar.

6.2.1 Case study 1: Mixed-phase cloud layer at high temperature and low rate of ice formation

Fig. 6.3 presents a cloud case measured at Leipzig on 17 September 2011. The AC cloud was advected from western direction at a height of 4200 m as part of a larger system of layered clouds as visible from Fig. 6.3a. The GDAS radiosonde profile, interpolated to the coordinates of Leipzig, shown in Fig. 6.3g, indicates a CTT of $-9\text{ }^{\circ}\text{C}$. The cloud radar (Fig. 6.3b) shows particles falling from the cloud layer. At 00:17 UTC, a short period of particle melting was detected in the LDR. The sudden change in particle fall velocity and the high LDR of -18 dB (arrows in Fig. 6.3d and 6.3f) confirm that the precipitation falling from the cloud top layer contained ice particles and that the cloud layer contained a mixture of cloud droplets and ice crystals. This cloud case, exhibiting radar reflectivity factors smaller than -30 dBZ , surely puts the measurement equipment and the ice-classification methods to a test, but it also makes the benefit of lidar and radar coupling obvious. The lidar shows a small signal below the cloud layer, which is probably originating from humidified aerosol particles, since the layer is not visible in the cloud radar measurements. Also, the depolarization channel (not shown) of the PollyXT lidar did not receive any signal between 2000 and 4000 m height. Histograms of the vertical velocity are inserted into Fig. 6.3c and Fig. 6.3d. To avoid influence of falling ice crystals, the vertical-velocity histogram of WiLi is obtained at cloud base, where the received intensity from the cloud droplets is strongest. The vertical-velocity statistics derived from this cloud was also used as input for the numerical simulations presented in Section 2.4. The standard deviation of the vertical velocity at cloud base is $\sigma_v = 0.44\text{ m s}^{-1}$ and the mean vertical velocity is $\bar{v} = -0.12\text{ m s}^{-1}$ (both derived from 663 data points).

The presence of ice particles itself is an interesting finding at this relatively high CTT. The cloud-radar measurements also allow the estimation of the size of the falling particles. The fall speed of the falling particles was about 0.6 m s^{-1} (e.g., at 00:15 UTC and 3000 m height). According to Fig. 3.4, the ice particles were, therefore, relatively large with $D_m > 1\text{ mm}$. Considering the very weak signal received by the cloud radar in the range $Z = -30\text{...}-45\text{ dBZ}$, the number concentration of the detected particles was in the range of $N \approx 0.1\text{...}1\text{ m}^{-3}$, assuming hexagonal ice columns. The few ice crystals probably grew fast inside the predominantly liquid cloud layer and deposit quickly. Under such conditions, vertical air motions can easily maintain the liquid phase against the ice crystals.

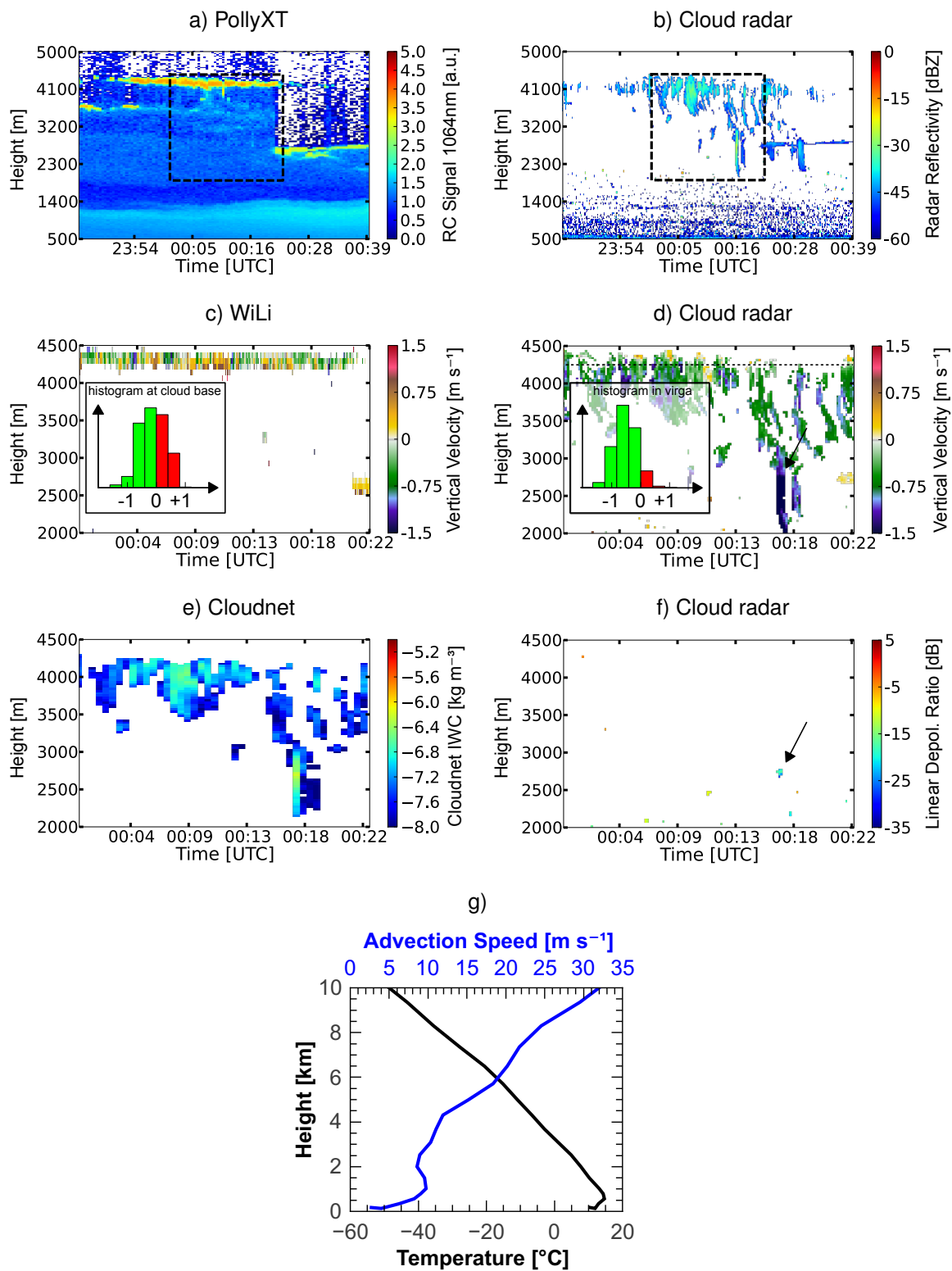


Figure 6.3: Mixed-phase cloud layer recorded at Leipzig on 17 September 2011, 0:00-0:22 UTC. The time-height section marked with a dashed box in a) and b) is depicted in c) to f), respectively. The arrows in plots d) and f) indicate a short melting event. Panel g) shows temperature and advection speed from 0 to 10 km height from the GDAS dataset for grid point Leipzig on 17 September 2011, 0:00 UTC.

Hogan et al. [2006] proposed a method to estimate the IWC and optical particle extinction α from temperature and radar reflectivity. The method is based on airborne in-situ measurements and provides the following simple logarithmic parameterizations:

$$\alpha = 10^{(0.000447ZT+0.0683Z-0.0171T-3.11)} \times 10^6 \text{ Mm}^{-1}, \quad (6.1)$$

$$\text{IWC} = 10^{(0.000242ZT+0.0699Z-0.0186T-1.63)} \times 10^{-3} \text{ kg m}^{-3}, \quad (6.2)$$

where Z is the radar reflectivity factor in dBZ and T the temperature in °C. Errors are estimated to be 50% for both α and IWC in the temperature interval above -40 °C. The relations presented here are valid for a 35 GHz radar. Cloudnet uses these parameterizations to operationally provide IWC values from the radar reflectivity and model temperature (e.g., Fig. 6.3e). In the context of this work, the quality-assured IWC values of Cloudnet are used. This quality assurance involves several checks, e.g., for high radar attenuation. For this case study, Cloudnet provides $\text{IWC} = 10^{-8} \dots 10^{-7} \text{ kg m}^{-3}$ in the cloud virga (see Fig. 6.3e), which matches the order of magnitude of the IWC reproduced by numeric modeling in Section 2.4.

6.2.2 Case study 2: Mixed-phase cloud layer at low temperature and high rate of ice production

Figure 6.4 presents another observation of an AC layer with precipitating ice particles observed at Leipzig on 2 August 2012. The cloud was part of a frontal system advected from south-western direction with an advection speed of 20 m s^{-1} at cloud top and $\text{CTT} = -29$ °C (see Fig. 6.5). The identification of ice precipitation is considerably easier in this case than in the one before. From the cloud virga a clear depolarization signal was received by the lidar (Fig. 6.4c) and even sporadic LDR values can be recognized in the cloud radar measurements (Fig. 6.4d). The elevated LDR values of -22 dB at 21:30 UTC and 6500 m height point towards large, non-spherical particles. The mean depolarization ratio detected by the PollyXT lidar in Fig. 6.4c is around 0.5 in the virga. Higher values are probably noise. At cloud base, the depolarization ratio monotonically increases from 0.3 to about 0.5 at cloud top, due to multiple scattering of droplets in the liquid-water layer.

The mean radar reflectivity factor of falling ice particles is -22 dBZ. According to Eq. (6.1) and the temperature profile from the GDAS radiosonde, a mean particle extinction of $\alpha \approx 90 \text{ Mm}^{-1}$ is derived. Cloudnet shows an IWC between 10^{-7} and $10^{-5} \text{ kg m}^{-3}$ (see Fig. 6.4h). Cloudnet also provides the LWC (Fig. 6.4g). The LWC values are computed by the scaled adiabatic approach of Cloudnet [Pospichal et al., 2012], which is based on measurements of the HATPRO microwave radiometer. The algorithm distributes the liquid water path (LWP) measured with the HATPRO radiometer amongst all detected liquid sub-layers. Together with the parameterizations of Hogan et al. [2006], ice-water path (IWP), liquid-water path (LWP) and condensed-water path ($\text{CWP} = \text{LWP} + \text{IWP}$) of any cloud can be derived. Fig. 6.6 shows these quantities for the cloud layer of Fig. 6.4. IWP and LWP values were derived by integration of IWC and LWC values over the cloud column (5600 to 7800 m height). In Fig. 6.4g, it can be

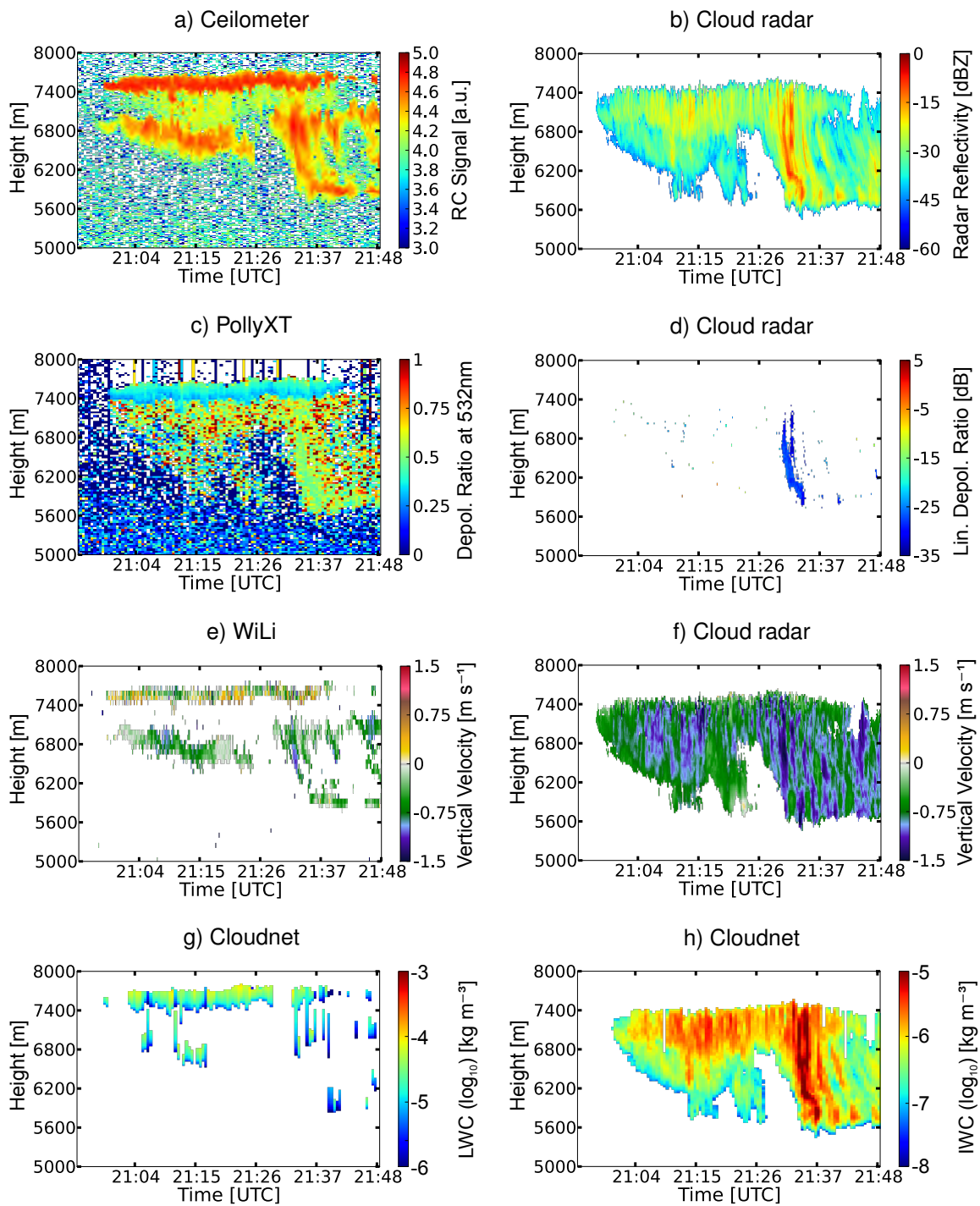


Figure 6.4: Mixed-phase cloud layer observed at Leipzig on 2 August 2012, 21:00-21:45 UTC. The left and right columns show products derived from lidar and radar, respectively. Ceilometer, WiLi and cloud radar were pointed to the zenith, while PollyXT was tilted 5° off-zenith.

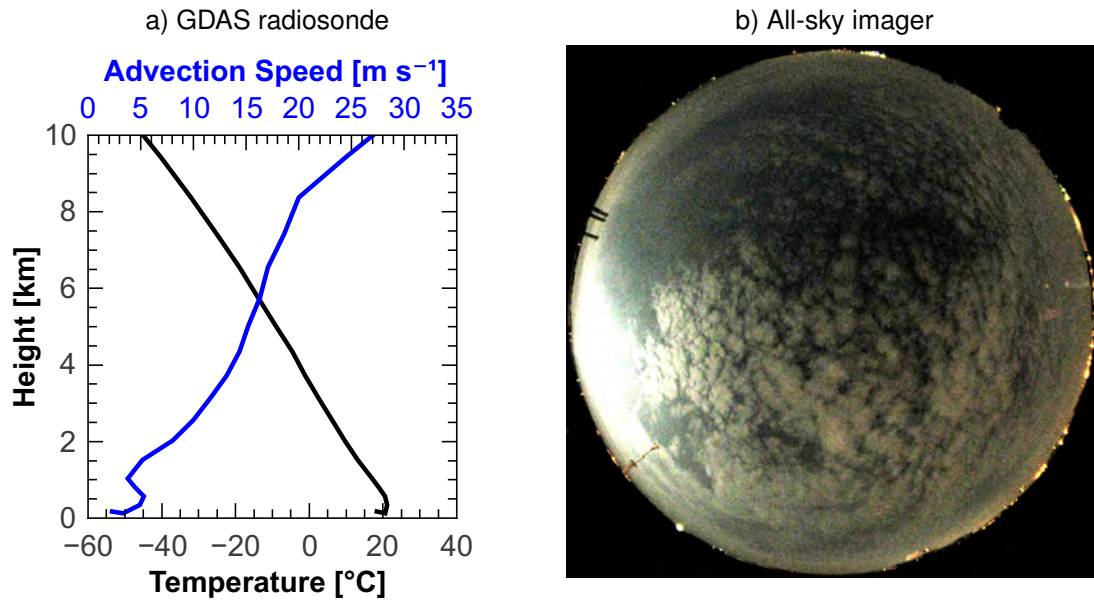


Figure 6.5: (a) Temperature and advection speed from 0 to 10 km height from GDAS dataset for grid point Leipzig on 2 August 2012, 21:00 UTC. (b) Brightness-enhanced picture of the all-sky imager on the roof of TROPOS from 21:30 UTC.

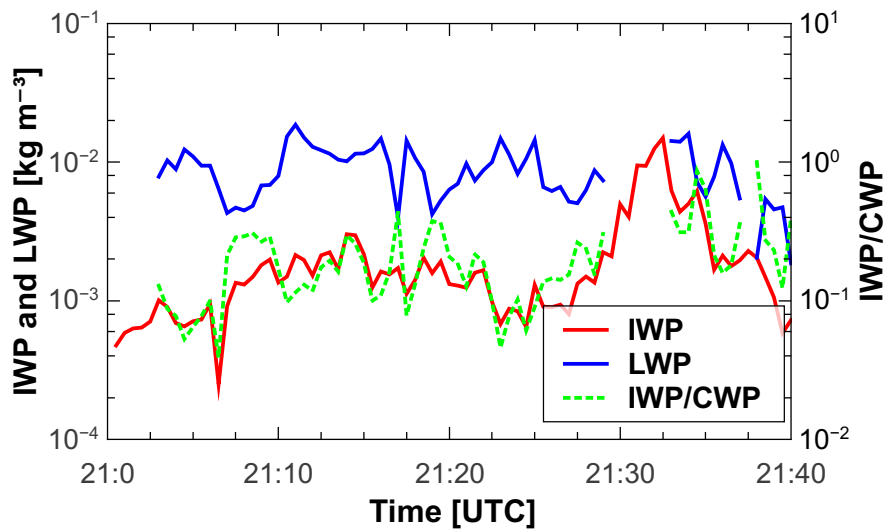


Figure 6.6: IWP, LWP and the ratio between IWP and CWP for the cloud of Fig. 6.4. IWP and LWP are derived by integrating the IWC and LWP values provided by Cloudnet over the complete height of the cloud, including the liquid cloud top and the falling ice particles.

seen that there are liquid layers classified within the cloud virga at 6800 m height. This misclassification is a result of strong specular reflections that affect the measurements of the vertically pointing ceilometer, shown in Fig. 6.4a. The signal exceeds the threshold used to classify liquid layers in Cloudnet, so additional liquid layers are identified in these regions and Cloudnet distributes the measured LWP among them. Therefore, LWC is also integrated over the total cloud column for computing the LWP. Around 21:30 UTC a short gap in the LWP measurements can be seen due to high signal attenuation in the precipitation. For the following analysis, such gaps are filled with the mean of the existing values.

6.3 Observation of cloud freezing with LACROS

Cloud freezing properties have been studied at TROPOS for a long time. Extensive measurement efforts have been carried out globally [Ansmann et al., 2009; Kanitz et al., 2011]. Seifert et al. [2010], e.g., analyzed a ten-year dataset of EARLINET lidar observations to derive the temperature dependence of ice formation. Recently, Zhang et al. [2010a] presented latitude-dependent statistics on mixed-phase cloud occurrence, retrieved from combined CALIPSO lidar and CloudSat radar observations. The results for the latitude belt from 30° N to 60° N were found to be in contradiction with respective lidar observations performed at Leipzig (51° N, 21° E) from 1997 to 2008 [Seifert et al., 2010]. Compared with CALIPSO/CloudSat these lidar measurements show a much lower mixed-phase cloud fraction for the temperature range between -10°C and -25°C .

With LACROS there is the chance to resolve this issue, because the same systems employed in the measurement campaigns before (PollyXT and MARTHA) are now accompanied by the cloud radar. It has to be determined, whether it is possible to harmonize lidar and radar data regarding mixed-phase cloud observations. This harmonization would significantly increase the comparability and the scientific value of past studies. Therefore, the combined ground-based lidar/radar dataset of the UDINE campaign was analyzed for the time period from August 2011 to January 2013. In this section, the threshold values of particle backscatter and extinction are derived, above which lidar can detect a cloud being mixed phase. The microphysical properties of mixed-phase clouds are analyzed in the following Section 6.4. Contents of both sections have been published in Bühl et al. [2013].

6.3.1 Adaption to CALIPSO/CloudSat observation strategy

There are big differences between remote-sensing measurements taken from satellite and from ground-based platforms. The comparison of ground-based and satellite-based data is therefore challenging and the dataset of the UDINE campaign has to be specially processed to be comparable to the satellite-based datasets. The most important issue may be that the satellite has a speed of about 7700 m s^{-1} over ground. Hence, it only observes snapshot-like cross sections of the clouds, but can sense a cloud over its complete

geometric extent, at least in one direction. A ground-based station like LACROS can observe a cloud in more detail, but depends on the cloud moving over the station. In the following, a way is shown, how satellite and ground-based measurements can be connected.

The satellite-based study of Zhang et al. [2010a] focused on so-called “mid-level liquid-layer-topped stratiform clouds” with vertical extent of the liquid layer smaller than 500 m. At the time of this study, the CALIPSO and CloudSat satellites traveled in the same orbit in the so-called “A-Train” formation, with only 15 seconds separation. The CALIPSO lidar delivers information about CTH, whereas the CloudSat radar measures the properties of the precipitating particles below the cloud with a horizontal resolution of about 1.4 km. Five CALIPSO profiles were averaged over the 1400 m wide footprint of the CloudSat radar. Zhang et al. [2010a] analyzed each snapshot-like profile individually and considered it as “mixed-phase”, if a radar signal was present below the cloud top. Otherwise, it was considered “liquid”. A discrimination between drizzle and ice particles could not be done from space.

From the UDINE dataset 352 cases of mid-level layered clouds were selected (like the one in Fig. 6.4). The number of cloud cases naturally decreases with decreasing CTT (see Fig. 6.2). However, in the interval between -25°C and 0°C the cloud numbers are sufficient to provide statistical errors around $\pm 10\%$. The present study is restricted to mixed-phase clouds. Pure ice clouds (e.g., cirrus) were left out intentionally. For case selection, the criteria discussed above in Section 6.1 were applied. To be able to compare the measurements of this work to those of CALIPSO and Cloudsat, a similar evaluation process like done by Zhang et al. [2010a] was carried out with the UDINE dataset. If, e.g., a horizontal wind speed of 15 m s^{-1} is assumed, each 30-s Cloudnet profile would represent a length of 450 m in the atmosphere. For each profile, the CTH is estimated and the corresponding CTT and advection speed is derived from the GDAS dataset. With the help of the advection speed the geometrical length of each profile (“virtual ground track”) is determined by multiplying its time duration with the advection speed. From the single profiles the mixed-phase cloud fraction is calculated: For each 5-K interval of CTT the total length of the ice-containing profiles is divided by the length of all profiles. This profile-based evaluation method is different to previous lidar-based studies (e.g., [Seifert et al., 2010; Kanitz et al., 2011]), where always complete cloud cases (lasting from minutes to several hours) were classified to be “ice-containing”, if there were ice particles detected anywhere below the liquid cloud base.

6.3.2 Observations

The mixed-phase cloud fraction per temperature interval is shown in Fig. 6.7, where the results of this study (red curve) are compared with the study of Seifert et al. [2010] (black curve) and the satellite-based study of Zhang et al. [2010a] (green curve). The results of this study compare well with the satellite measurements over the whole temperature range. However, they deviate strongly from the results of Seifert et al. [2010].

There is obviously a difference in the ability of lidar and radar to detect falling ice particles, as it was shown in the case studies discussed in Section 6.2. Therefore, the

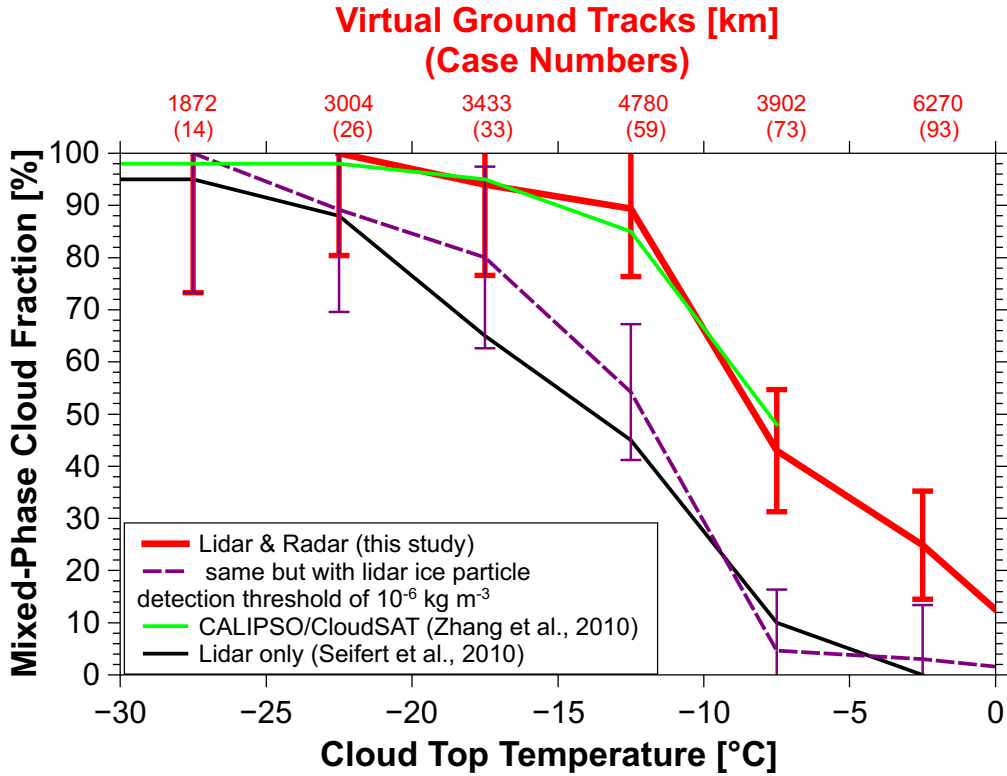


Figure 6.7: Comparison of the current study with other studies about heterogeneous ice formation. On the top axis the total virtual ground tracks and (in brackets) the number of cases involved are shown for each 5-K interval of CTT. Error bars show the statistical uncertainty based on the number of cases. For error bars of Seifert et al. [2010] please refer to the original publication, in Zhang et al. [2010a] no error bars are given.

conditions (α , IWC and IWP/CWP) are investigated at which both lidar and radar can equally detect ice formation. The statistical distribution of the radar reflectivity factors measured in the virgae of mixed-phase clouds is given in Fig. 6.8. From each median value, the corresponding particle extinction α and the IWC are derived with the method of Hogan et al. [2006] (see Eqs. (6.1) and (6.2)) and displayed in Fig. 6.9. If one assumes a lidar detection threshold of $\alpha_{\min} \approx 30 \text{ Mm}^{-1}$ (corresponding to $\beta_{\min} \approx 1 \text{ Mm}^{-1} \text{ sr}^{-1}$), the cloud-freezing curve of Seifert et al. [2010] can be reproduced from data of this study by defining all cases which lie below this threshold as “liquid”. The resulting curve of mixed-phase fraction is shown in Fig. 6.7 (dashed purple). From Fig. 6.9 it is visible that the extinction threshold corresponds to the introduction of an IWC detection threshold of $10^{-6} \text{ kg m}^{-3}$. In the context of the parameterizations used here, both values correspond to a radar reflectivity factor of -27 dBZ for the temperature interval between -40 and $-10 \text{ }^\circ\text{C}$. Given the difference in the evaluation method, there may be still a difference between the statistics of this study and Seifert et al. [2010]. Nevertheless, the results show that the differences between the statistics occur probably because the lidar obviously misses the low amounts of ice at temperatures larger than $-15 \text{ }^\circ\text{C}$.

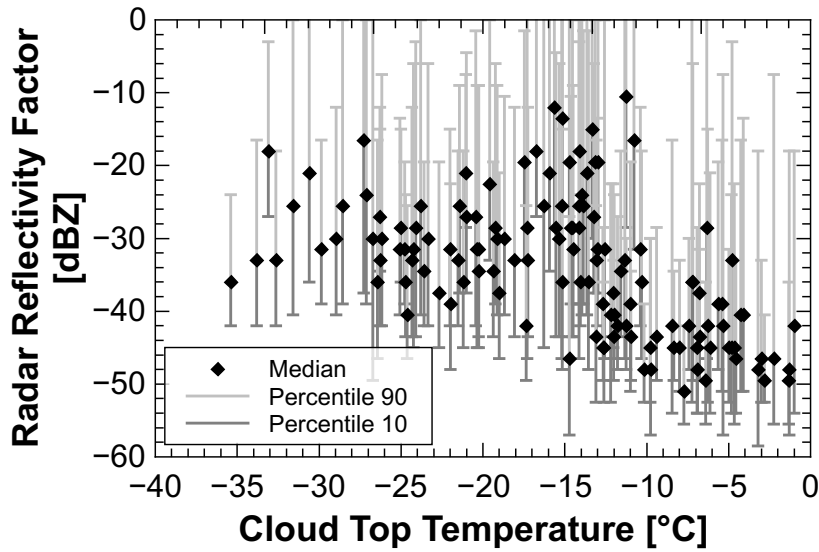


Figure 6.8: Distribution of the radar reflectivity factors measured within the virgae of each mixed-phase cloud. Median values are depicted as diamonds with its $\pm 40\%$ spread values. Note the accumulation of high values in the temperature range from -15 to -10 °C, where the WBF process is most efficient.

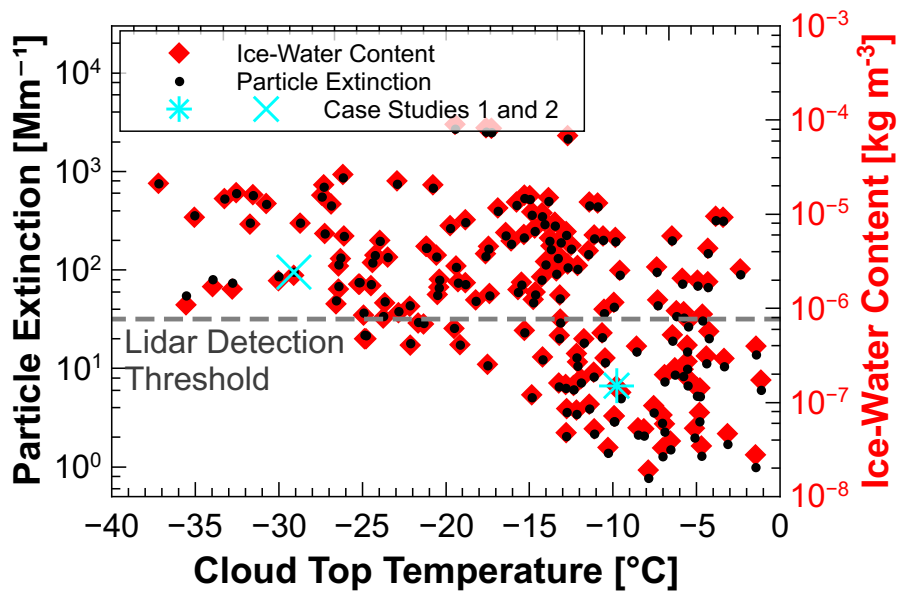


Figure 6.9: The mean particle extinction (α) and ice water content (IWC) derived for all cases with the parameterization of Hogan et al. [2006] (see Eqs. (6.1) and (6.2)). Errors of the single values are about one order of magnitude due to uncertainties in the α and IWC parameterizations and a possible incomplete detection of particles by the cloud radar.

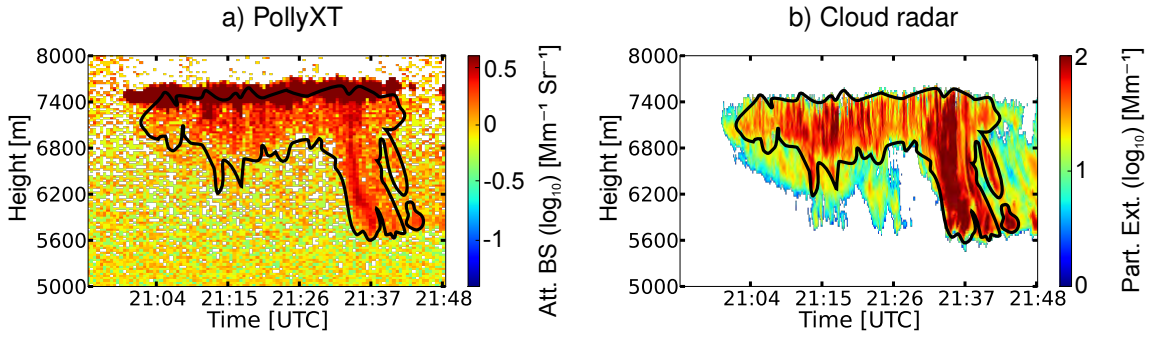


Figure 6.10: (a) Attenuated backscatter (Att. BS) at a wavelength of 532 nm of PollyXT, calibrated at 5000 m according to Bucholtz [1995], (b) particle extinction (Part. Ext.) derived by Eq. (6.1) and a GDAS radiosonde profile. The contour line for 30 Mm^{-1} derived from (b) is drawn in both graphs. It is visible that the PollyXT does hardly detect any signal below $\alpha = 30 \text{ Mm}^{-1}$ or $\beta = 1 \text{ Mm}^{-1} \text{ sr}^{-1}$. Scales are shifted by a factor of $L_i = 25 \text{ sr}$ (lidar ratio for ice particles).

The threshold proposed here should not be mixed up with the signal-to-noise ratio of a lidar system. The PollyXT and the MARTHA lidars are capable of detecting $\beta < 1 \text{ Mm}^{-1} \text{ sr}^{-1}$, especially when averaging over a lot of profiles. However, assuming this threshold, the temperature dependence of ice formation from Seifert et al. [2010] is reproduced best. Evidence for the source of the threshold can be found in Fig. 6.10. It can be seen from the figure that even at 6800 m height the molecular backscatter is so strong that particle backscatter below $1 \text{ Mm}^{-1} \text{ sr}^{-1}$ disappears in the background. It may also be an issue that the 532-nm channel of PollyXT is equipped with strong neutral density filters to avoid dead-time effects in the photon-counting signal. This strategy is usually applied for observations of clouds. Hence, the particle-detection capabilities of a lidar channel may be higher, if dead-time effects are accepted at cloud base in order to increase signal strengths in the virgae. From Fig. 6.4c it can be seen that the depolarization channel still detects a weakly depolarized signal in regions where no particles can be seen in the total signal.

6.4 Quantification of heterogeneous ice formation in mixed-phase layered clouds

It was shown in the previous section that the combination of lidar and radar does not only allow the detection of the mere presence of mixed-phase cloud layers. It can also help to derive quantitative information about the properties of the falling ice crystals. To get further insight into the process of ice formation, information about the ratio of ice and water mass in a cloud layer is of major importance. Therefore, the IWP and LWP of the clouds under study were derived by column integration of the IWC and LWC provided by Cloudnet. Both IWC and LWC are quality-assured products of Cloudnet, but it is worth noting that all cloud cases in this study were checked for elements, which could potentially compromise the derived IWP or LWP values. For example, in the

presence of a melting layer the IWC integration was always started above it. For each vertical profile the ratio

$$\frac{\text{IWP}}{\text{IWP} + \text{LWP}} = \frac{\text{IWP}}{\text{CWP}} \quad (6.3)$$

was derived. Column integration of the IWC allows the determination of the maximum ice mass that was produced at cloud top. Water vapor deposition below the liquid layer may contribute to the IWP by an unknown extent, so the actual ice mass produced in the liquid layer can be lower than the observed IWP. Hence, the IWP/CWP ratio is a robust upper estimate for the mass ratio of ice and water in the predominantly liquid top layer of the clouds. The IWP/CWP ratio is averaged only over profiles where ice was detected, making it an upper estimate for each single cloud case.

The average IWP, LWP and IWP/CWP ratio for all cloud cases are shown in Fig. 6.11 and 6.12. The case studies presented before are marked with blue symbols. The cloud cases in Fig. 6.11 and 6.12, which fall below the lidar detection threshold, are marked with red squares. In this depiction, the reasons for the characteristic differences between the lidar and radar studies at temperatures larger than -15° are best visible. For the clouds at higher temperatures, liquid water seems to dominate and the low amount of ice crystals are not detected by lidar. 90% of the cases that fall below the lidar IWC detection threshold show an IWP smaller than $10^{-3} \text{ kg m}^{-2}$. 85% of the IWP/CWP ratios are below 10^{-1} , 60% are below 10^{-2} . It is worth noting again, that the IWP/CWP ratio indicates the maximum mass ratio between ice and liquid water within the mixed phase cloud top. Hence, it yields insight, if either liquid water or ice is dominating the microphysics of the cloud (compare with the IWC/CWC ratio in Section 2.3.2).

6.4.1 Discussion of cloud-freezing study

The temperature at which half of the cloud profiles contain ice is $-9 \pm 3^\circ \text{C}$ in this study (see red curve in Fig. 6.7). Yet, it cannot be directly concluded from these measurements that, at this temperature level, ice production plays a major role for the further development of the cloud layer towards glaciation or precipitation formation. The high measurement sensitivity of powerful radar systems like the MIRA-35 cloud radar or the Cloud Profiling Radar (CPR) on CloudSat could be misleading. The ability to measure and to quantify the efficiency of heterogeneous ice production from ground can significantly improve our understanding of heterogeneous ice formation. In this context, the IWP/CWP ratio seems to be an interesting measurement quantity. As mentioned in Chapter 2, the ratio of ice to liquid water can strongly influence the microphysics of a mixed-phase cloud layer. It may be necessary to take into account the level of cloud glaciation when investigating heterogeneous ice formation, because the mass ratio between ice and water is found here to cover several orders of magnitude. It could distort the picture of heterogeneous ice formation significantly, if a cloud with an IWP/CWP ratio of 10^{-4} is treated in the same way as one, which is just about to glaciate completely and has an IWP/CWP ratio approaching 1.0. The IWP/CWP also increases the comparability of cloud-freezing studies with different measurement systems. All measurement systems that can accurately provide IWC and LWC should produce very

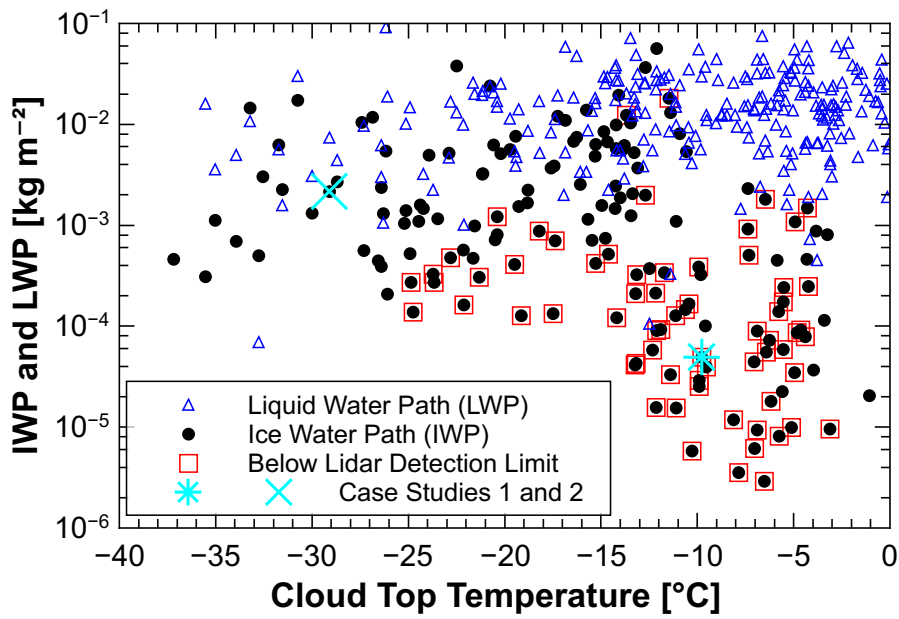


Figure 6.11: Mean LWPs and IWPs of all cloud cases under study. IWP values of cases that fall below the lidar IWC detection threshold are marked with red squares.

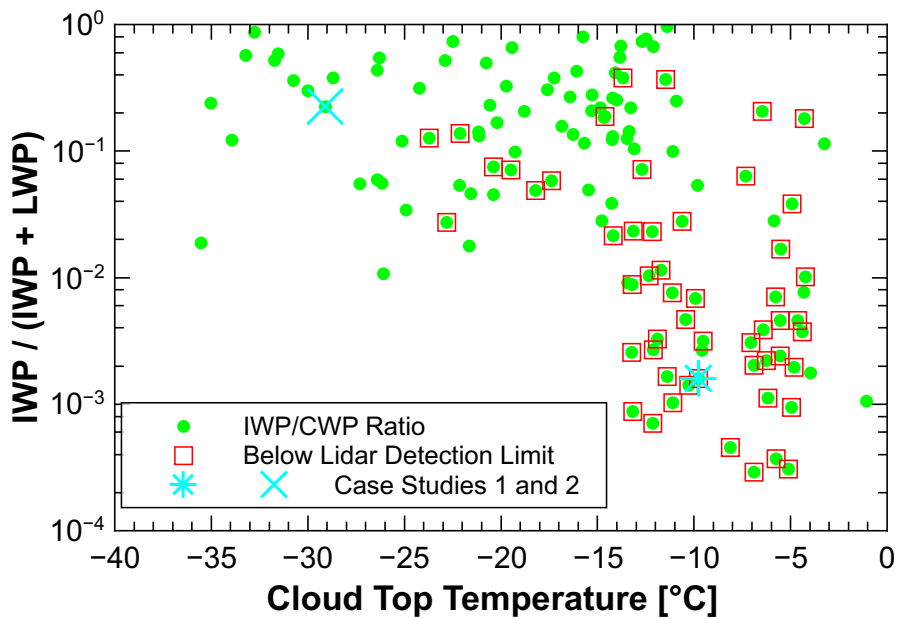


Figure 6.12: IWP/CWP ratios for all mixed-phase cloud cases ($IWP > 0$). Again IWP/CWP values of cases that fall under the lidar IWC detection threshold are marked with red squares.

similar IWP/CWP statistics above their IWC detection threshold. That makes cloud-freezing statistics comparable and independent of the absolute ice-detection capability of single measurement systems.

The red and the green curves in Fig. 6.7 basically tell us that ice formation is occurring in the atmosphere at any temperature level below 0 °C. But with increasing temperature, the amount of ice decreases and liquid water dominates more and more the microphysics of the layered clouds. Hill et al. [2013] show that it is still difficult to assess at which levels of ice formation a mixed-phase cloud will turn into an ice cloud. It is shown here that ground-based remote sensing can give additional information about such cloud systems, allowing the estimation of the ratio between ice and liquid water. However, it has to be kept in mind that the IWC (and therefore also the IWP) measurements are estimates and to a certain amount reflect the parameterization method they were retrieved with. The method of Hogan et al. [2006] gives a good start, but in future more direct ways must be found to quantify the process of heterogeneous ice formation not only on the basis of the total mass of ice and water particles, but also with their corresponding particle number concentrations. Only in this way, the process of particle nucleation can be quantified and measured precisely.

6.5 Combined lidar/radar vertical-wind statistics in layered clouds

In this section, vertical-velocity statistics at cloud bases are presented. Such measurements are novel in different aspects. At first, vertical-velocity statistics in layered clouds have, up to this point, only been available from aircraft measurements. No extensive ground-based measurements are available. Secondly, the combination of Doppler lidar and cloud radar is unique and allows mutual validation of both systems. In the following two subsections, the ice-detection capabilities of the cloud radar are used to analyze the influence of falling ice particles on Doppler lidar signals. In turn, the Doppler lidar is used to validate the vertical-velocity measurements of the cloud radar. The Doppler lidar is found to exhibit little influence from falling particles. This inter-evaluation of

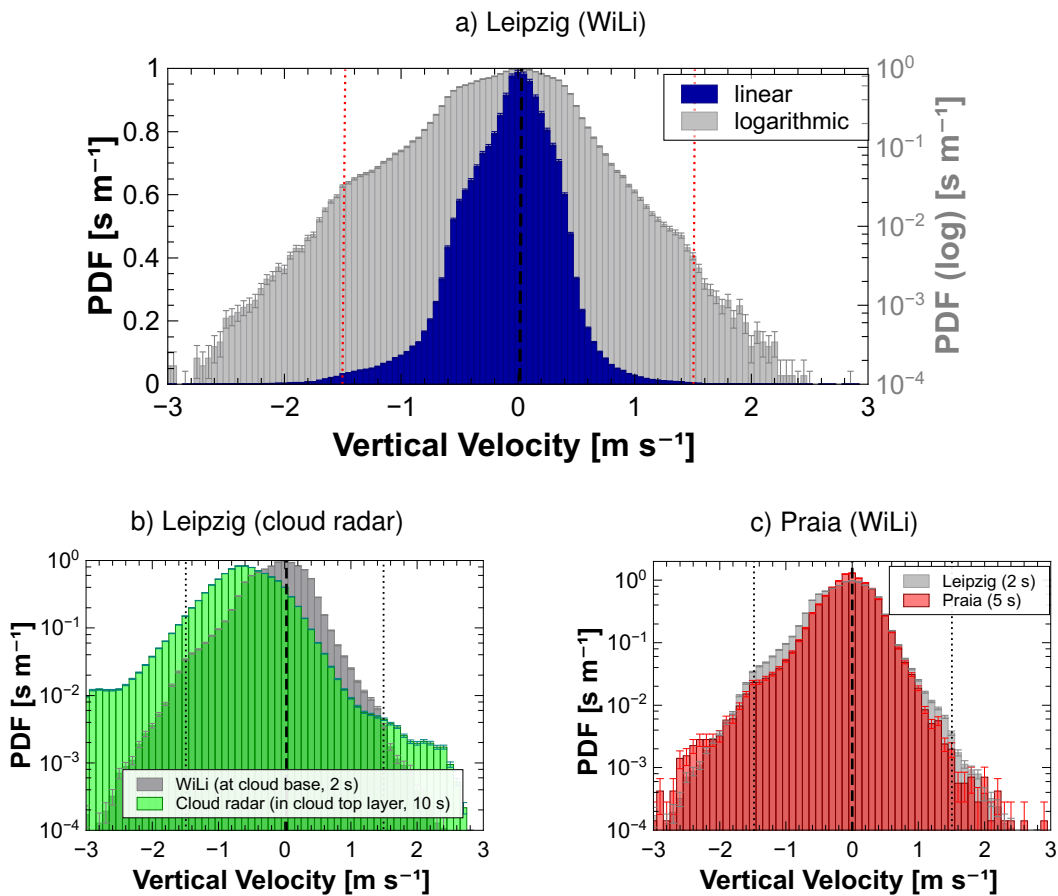


Figure 6.13: Overview about the vertical-velocity datasets collected at Leipzig (with Doppler lidar WiLi and cloud radar) and Praia (WiLi). In all graphs vertical, dotted lines are drawn at $\pm 1.5 \text{ m s}^{-1}$ to make asymmetries easier visible. For the WiLi histograms, the values were read from the point, where the largest signal occurred in the profile (cloud base). The cloud radar values were read from the entire liquid cloud layer, because the cloud base cannot be derived unambiguously from the cloud radar measurement.

cloud radar and Doppler lidar is a prerequisite for the analysis presented in Section 6.5.4, where the vertical-velocity statistics from the UDINE dataset are analyzed with respect to meteorological influences, e.g., solar forcing or temperature. Differences between the statistics recorded in the sub-tropics (SAMUM-2) and the mid-latitudes (UDINE) are explored in Section 6.5.5.

Fig. 6.13 shows the probability density functions (PDF) of the three main components of the statistical dataset. A combined Doppler-lidar and cloud-radar dataset is available for Leipzig. At Praia combined Doppler lidar and Raman lidar (WiLi and BERTHA) measurements are available. There are inherent technical differences in the three datasets:

- The Doppler-lidar dataset from Leipzig (Fig. 6.13a) has been recorded with WiLi with 2-s resolution during a period of three years between 2010 and 2013. Therefore, the statistical significance is highest.
- The cloud-radar dataset (Fig. 6.13b) was also recorded at Leipzig between 2011 and 2013, but with a temporal resolution of 10 s. The radar is therefore less sensitive towards fast variations in the vertical velocity (see Section 5.4). Also, the vertical-pointing accuracy of the radar is smaller than that of WiLi, making the mean value less reliable.
- The Doppler-lidar dataset from Praia (Fig. 6.13c) is based on 16 weeks of measurements in the framework of the SAMUM-2 campaign (2008). It was recorded with 5 s temporal resolution.

The PDF shown in this chapter are all normalized in such a way that $\sum_{i=1}^N \text{PDF}(i)\Delta x = 1$ (i is the bin number, Δx the bin size and N the number of bins). The value of the PDF is hence independent of bin size and histograms with different binning can be compared quantitatively. With this normalization, the PDF comprises the reciprocal physical unit of the dataset values (e.g., s m^{-1} for vertical-velocity values).

6.5.1 Measuring vertical velocity at cloud bases of precipitating cloud layers

The measurement of the vertical velocity of air at cloud base with Doppler lidar and cloud radar is challenging. The measured velocity does not directly indicate the velocity of the air, but it is always biased by the fall velocity of droplets and ice crystals. In Chapter 5, the capabilities of Doppler lidar and cloud radar in measuring the vertical velocity at cloud base have been found to be comparable for a non-precipitating cloud layer. At the base of such layers, cloud droplets with $D \approx 10\text{...}20 \mu\text{m}$ occur and the offset due to fall velocity is negligible (see Fig. 3.4). In precipitating cloud layers, especially the cloud radar signal can be easily governed by big ice crystals or drizzle droplets, but also Doppler lidars are not completely insensitive to this bias. Therefore, the statistics of vertical velocities at the cloud bases is analyzed thoroughly to identify cloud regions, where falling particles affect the Doppler lidar measurements. In this section, the cloud

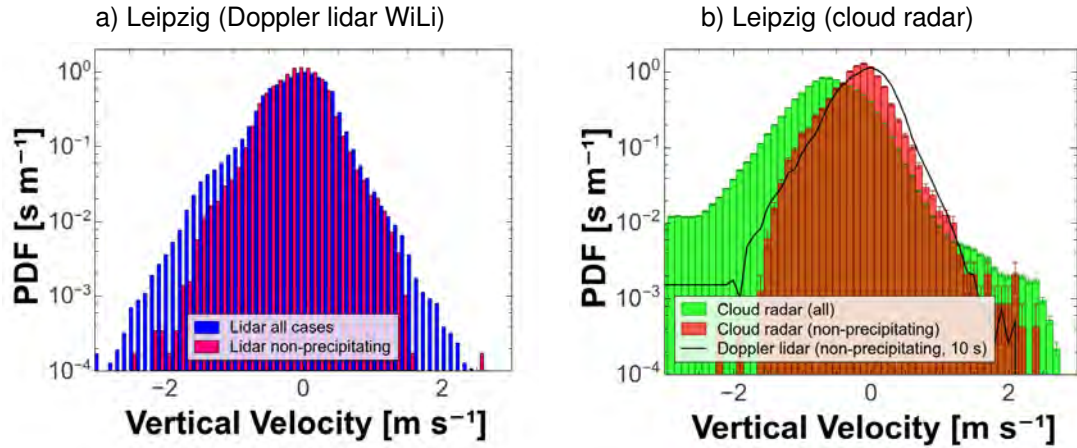


Figure 6.14: Comparison of all vertical-velocity values measured in the cloud column (cloud radar) and at cloud bases (WiLi). Precipitating clouds are compared with non-precipitating ones. It becomes obvious that a Doppler lidar is less susceptible to disturbances introduced by falling particles.

classifications of Section 6.3 are used to compare the signals of Doppler lidar and cloud radar in precipitating and non-precipitating layers.

Fig. 6.14a shows the distribution of vertical velocities at cloud bases measured with WiLi, separately for precipitating and non-precipitating cloud cases. To get a reliable separation, only cloud cases are taken into account that were observed with WiLi and the cloud radar simultaneously. The effects of falling particles on the measurements are minimal between -1 and 1 m s^{-1} , where 98% of the measurement values are located. Only outside this interval, differences in the statistics become significant. Fig. 6.14b shows the same differentiation for the cloud radar, taking into account all detected values inside the cloud layers (green histogram). A strong shift towards negative values is visible, presumably due to the detection of falling ice or water particles within the cloud layers. The mean of the vertical velocity shifts towards zero, if only the cloud cases without any sign of precipitation are taken into account (red histogram). For comparison, the Doppler-lidar statistics for non-precipitating cases (interpolated on a 10 s time grid) is shown as a black solid line.

At this point, it becomes obvious again why a combination of cloud radar and Doppler lidar can be so fruitful: Both systems together can be used to level out specific weaknesses of the single systems. In this way, the significance of both datasets is increased. Recently, the weak dependence of the WiLi signal on falling ice particles was, e.g., exploited in the investigations of mixed-phase cloud layers inside of cloud virgae detected by the cloud radar [Seifert et al., 2012].

To further qualify the WiLi measurements, the influence of falling particles on the vertical-velocity variance σ_v^2 is explored. This measurement quantity is commonly used to describe turbulence in cloud layers. Fig. 6.15a shows this quantity derived from WiLi measurements for cloud cases with and without precipitation. A shift of $0.03 \pm 0.02 \text{ m}^2 \text{ s}^{-2}$ towards higher vertical-velocity variances is visible for precipitating cases. In Fig. 6.15b,

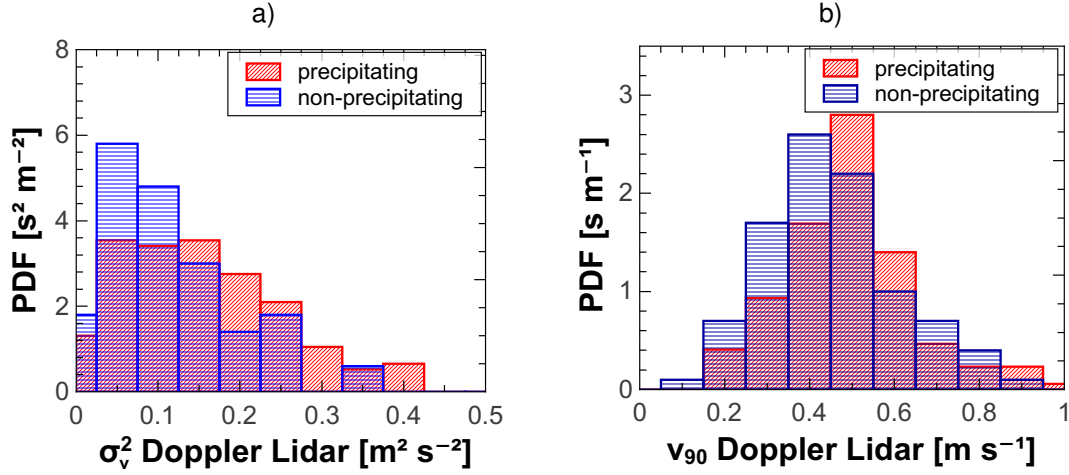


Figure 6.15: Cloud-base vertical-velocity variance for precipitating and non-precipitating clouds (a) and 90% percentile of updraft velocities (b).

the 90% percentile v_{90} of the positive vertical velocities is shown. It also shows a small shift of $0.06 \pm 0.04 \text{ m s}^{-1}$ towards positive values. Both shifts cannot be considered significant, given the high relative uncertainties.

6.5.2 Vertical-wind statistics between cloud base and cloud top

In Section 5.3 it has already been shown that it is possible to compare the vertical-velocity values of lidar and radar inside of a cloud layer on a single-case basis. In this subsection, the difference between the detected vertical velocities at cloud base, inside the cloud layer and at cloud top are investigated for the UDINE dataset.

The range-gate length of the cloud radar is much smaller (30 m) than that of WiLi (150 m). If the cloud radar detects a cloud, it is usually resolved into different range gates. WiLi, however, records the cloud layer by means of one strong peak at cloud base. For a meaningful comparison between the two systems, first the effects of the different range resolutions have to be eliminated. Therefore, in Fig. 6.16 the cloud-radar vertical velocities are averaged across the entire liquid cloud layer (dark red line), only taking into account non-precipitating clouds. This line is nearly identical to the one measured with WiLi (black dashed line) with a small offset of about -0.1 m s^{-1} in the mean value. The dotted lines represent the vertical-velocity statistics of precipitating clouds measured with the radar at cloud bases (purple), cloud centers (green) and at the cloud top (orange). In precipitating clouds the observed vertical velocities in the lowest radar bin are shifted towards negative values compared with those from cloud top. The distribution at cloud base shows $\sigma = 0.43 \text{ m s}^{-1}$, which is larger than at cloud top ($\sigma = 0.37 \text{ m s}^{-1}$). A bias between the vertical-velocity measurements of Doppler lidar and cloud radar is also visible in Fig. 6.17, where the mean values of the vertical velocity (\bar{v}) and the 90% percentile of the updraft velocities (v_{90}) are compared case by case. It is visible from that figure that both \bar{v} and v_{90} compare well for non-precipitating

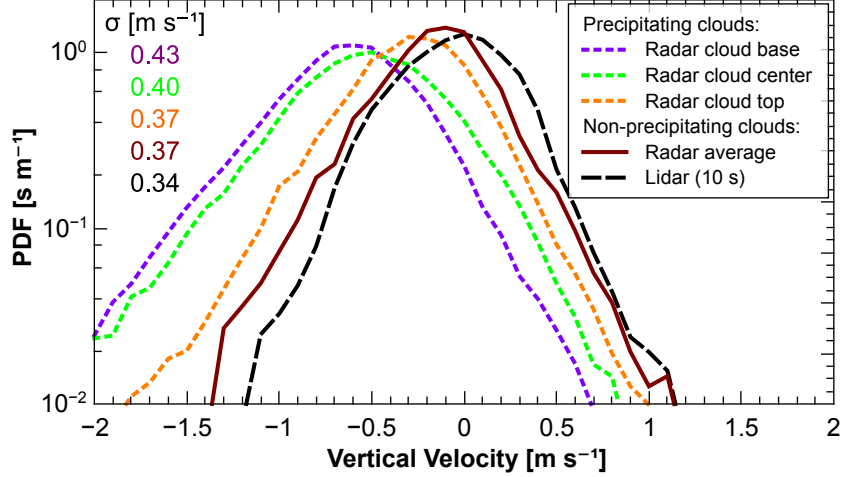


Figure 6.16: Statistical distribution of vertical velocities measured with the cloud radar in relation to their position in the cloud top layer. Standard deviations σ of each PDF are shown on the left.

clouds, while they are both shifted for precipitating clouds.

The mean shift between cloud-radar and WiLi measurements could be explained by a pointing error of the cloud radar. The radar is mounted directly on a container without any possibility of precision leveling. In Fig. 6.2 (Section 6.1) it was shown that the majority of clouds was advected from around 250° with a mean wind speed of about 13 m s^{-1} . A pointing error of 0.4° off-zenith away from this direction could, therefore, explain the discrepancy. In contrast, the beam of WiLi can be adjusted vertically with a leveled mirror, which reflects light back into the system from above the scanner unit. The mirror can be adjusted with an accuracy of 0.01° with the help of a precise air level. The pointing error of the scanner unit is on the same order of magnitude, yielding a total vertical pointing accuracy better than 0.1° and putting the possible influence on the vertical-velocity measurements into the order of 0.03 m s^{-1} .

The shift can also be explained by an offset produced by the presence of large cloud droplets. The cloud radar signal is always dominated by the largest droplets due to the D^6 -sensitivity. From Fig. 3.4 it is visible that liquid cloud droplets with a diameter of $50 \text{ }\mu\text{m}$ show a fall velocity of 0.06 m s^{-1} at $p = 650 \text{ hPa}$ and $T = -13^\circ\text{C}$. Let us assume the gamma distribution from O'Connor et al. [2004]:

$$N(D) \sim (D/D_0)^\mu \exp\left(-3.67 + \mu\right) \frac{D}{D_0}, \quad (6.4)$$

where D_0 is the median volume-equivalent droplet diameter and μ is a parameter controlling the width of the distribution. For SC clouds O'Connor et al. [2004] list values of D_0 in the range between 8 and $20 \text{ }\mu\text{m}$ and put μ into the range between 2 and 10 [Miles et al., 2000]. The maximum of the distribution is situated around $8 \text{ }\mu\text{m}$, if $D_0 = 15 \text{ }\mu\text{m}$ and $\mu = 6$. To find the maximum of the corresponding diameter-dependent cloud radar signal, Eq. (6.4) is multiplied by D^6 . The maximum of the resulting distribution is

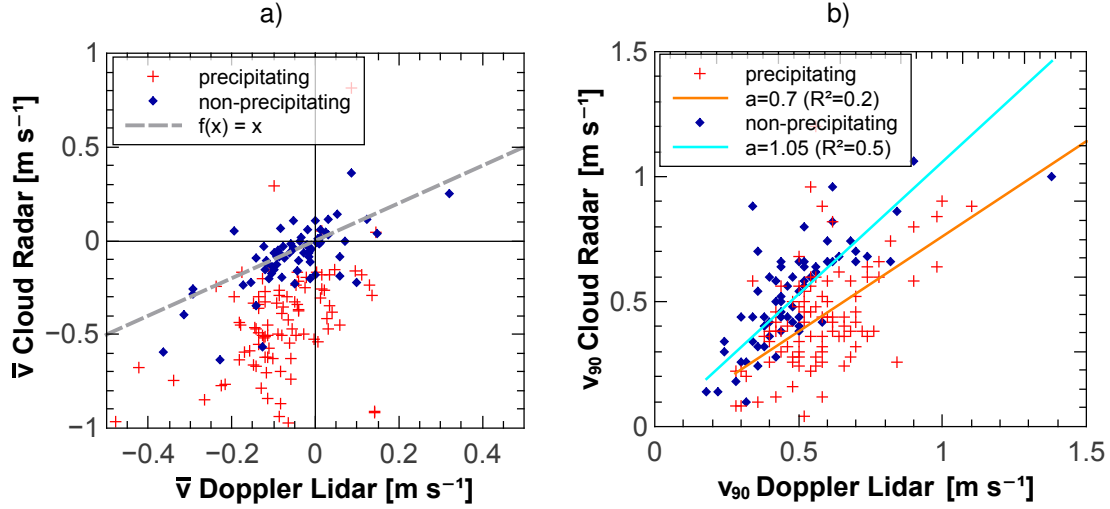


Figure 6.17: Scatterplots of vertical-velocity mean values (a) and 90% percentile of the updraft velocities (b) for single cloud cases measured with cloud radar and WiLi. Only cases with more than 150 valid vertical-velocity values from both instruments are considered. Slope values of a linear fit function $f(x) = ax$ are shown.

now at $20 \mu\text{m}$, corresponding to a terminal fall velocity of 0.01 m s^{-1} . 95% of the radar signal originates from particles smaller than $D = 30 \mu\text{m}$, which again corresponds to a terminal fall velocity of 0.04 m s^{-1} . Taking into account turbulent air motion inside of the cloud layers, all velocity measurements would be distributed equally around the central velocity bin of the cloud radar and the vertical-velocity statistics should not be shifted by more than 0.04 m s^{-1} . However, the production of a very small amount of drizzle droplets bigger than $30 \mu\text{m}$ could add to this. One droplet of $100 \mu\text{m}$ produces a signal which is a factor of $100^6/30^6 = 1371$ stronger than that of a droplet with a diameter of $30 \mu\text{m}$ and has already a fall speed of 0.4 m s^{-1} at 650 hPa (see Fig. 3.4).

6.5.3 Cloud-base vertical-velocity distribution as a function of height and temperature

Numeric climate and weather models usually do not resolve in-cloud turbulence directly. Hence, parameterizations are applied to describe the vertical movements in the atmosphere [Tonttila et al., 2013; West et al., 2013]. Measurements of vertical air velocity are thus required to either evaluate these parameterizations or to initialize the model (see Section 2.4). A possible height or temperature dependence of cloud-base vertical velocity is examined in Fig. 6.18a and 6.18b. Within this statistic, no significant differences in the vertical motions are found for the considered temperature and height range. The absence of such a dependence has big advantages for modeling, because only a reduced number of parameterizations is required. It can also be concluded that the physical mechanism creating and maintaining the turbulence must be independent of height and temperature.

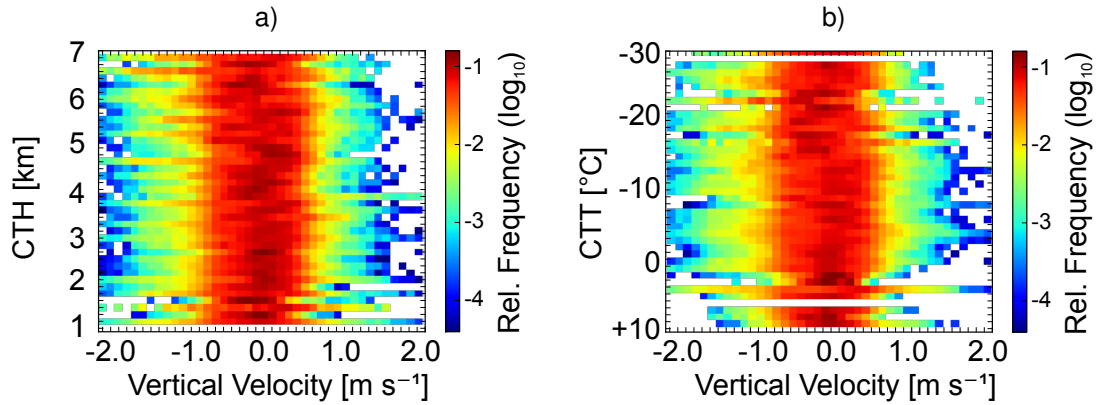


Figure 6.18: Distribution of vertical velocities in dependence of cloud top height (a) and cloud top temperature (b). All cloud cases from the UDINE dataset are taken into account, for which WiLi data is available. Each row is normalized to its sum. Deviations at +3 and -25 °C are due to a lower number of cloud cases within this specific temperature interval.

6.5.4 Effects of solar forcing and cloud phase on vertical-velocity statistics

Solar irradiation is one major driver of global air movements and can influence clouds by radiative heating. In this section, the solar influence on mid-level layered clouds is explored by sub-dividing the supercooled cloud cases of the UDINE dataset into liquid/mixed-phase and daytime/night-time cases. As before, the decision between liquid and mixed-phase clouds was made according to the cloud classification scheme introduced in Section 4.5. Daytime and night-time cases are separated by a ± 2 -hour interval around sunset and sunrise, respectively. Cases overlapping with this interval are left out from the daytime/night-time decision. The analyzed dataset is restricted to supercooled clouds to investigate the connection between vertical-velocity distribution and ice formation. Warm clouds would introduce a bias, because they principally cannot form ice and would only randomly attribute vertical-velocity values to the liquid-cloud fraction. Therefore, a “liquid” cloud is also a non-precipitating cloud in this context.

For all possible combinations of the classifications Fig. 6.19 shows the vertical-velocity distributions at cloud bases. The first to fourth statistical moments were derived for each distribution and are shown in Table 6.1. The first moment is the mean value \bar{v} , the second moment the variance σ_v^2 . The third moment of a sample with N values is computed by

$$\gamma_3 = N^{-1} \sum_{i=1}^N \left(\frac{v_i - \bar{v}}{\sigma_v} \right)^3 \quad (6.5)$$

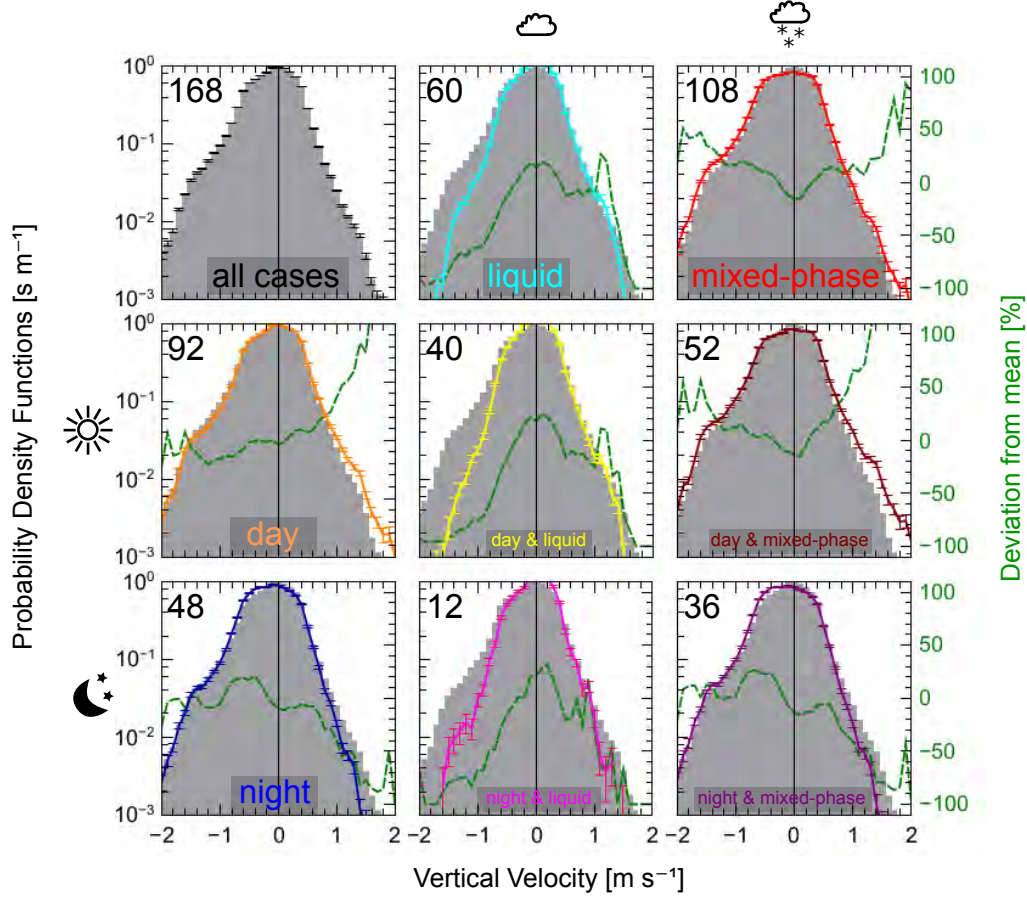


Figure 6.19: Vertical-wind statistics for different types of supercooled cloud layers. In each sub-figure the histogram of the total dataset is plotted as a reference (gray background) and the number of involved cloud cases is given in the upper left corner. See Table 6.1 for the moments of each PDF.

Table 6.1: Moments of the vertical-velocity distributions for different combinations of cloud phase and time of appearance (see histograms in Fig. 6.19).

	No. of cases	Average m s^{-1}	Variance $\text{m}^2 \text{s}^{-2}$	Skewness	Kurtosis
all	168	-0.068	0.210	-0.441	1.411
mixed	108	-0.092	0.232	-0.426	1.220
liquid	60	0.003	0.134	-0.113	1.086
day	92	-0.034	0.204	-0.349	1.701
night	48	-0.109	0.189	-0.499	1.231
day and mixed	52	-0.060	0.243	-0.322	1.361
day and liquid	40	0.017	0.122	-0.018	1.087
night and mixed	36	-0.124	0.196	-0.479	1.169
night and liquid	12	0.008	0.119	-0.283	0.877

and called skewness, the fourth moment is

$$\gamma_4 = \frac{N^{-1} \sum_{i=1}^N (v_i - \bar{v})^4}{(N^{-1} \sum_{i=1}^N (v_i - \bar{v})^2)^2} - 3 \quad (6.6)$$

and called kurtosis. The third moment is a measure for the asymmetry of the distribution. The fourth moment indicates any excess of the distributions compared with a Gaussian distribution. The third and the fourth moments are very sensitive towards outliers, therefore all moments are computed for the velocity range between -3 and 3 m s^{-1} . In this interval nearly all significant vertical-velocity values are located (see logarithmic graph in Fig. 6.13a).

An influence of solar forcing may be visible from Fig. 6.19 in the graphs marked with day (orange) and night (blue). Compared with the mean dataset in the background (gray), the PDF of the day cases is about 50% larger at an updraft of 1 m s^{-1} . At this vertical velocity, the PDF from the night cases is 50% smaller compared with the mean dataset. This difference may be attributed to solar heating introducing more energy into the cloud. The mechanism leading to an increase in updraft strength might, however, not be straightforward. The main source of turbulent energy for layered clouds is probably radiative cooling at cloud top. It is visible that the higher vertical velocities occur mainly in mixed-phase clouds (category: day & mixed-phase in Fig. 6.19). The influence of solar radiation on particle growth in mixed-phase clouds is discussed in Lebo et al. [2008], where it is found that solar heating can, e.g., influence the effectiveness of the WBF process.

It is worth noting that the vertical-velocity distribution of liquid clouds shows a mean value (1st moment) of 0.003 m s^{-1} (see Table 6.1). Additionally, the skewness (3rd moment) of the distribution is only -0.113 , meaning that it is very close to the Gaussian distribution. The influence of falling particles can, again, be seen between the right and the middle column in Fig. 6.19. The excess at vertical velocities around -1.5 m s^{-1} is clearly more prominent in the mixed-phase cases. The mean shift towards negative values in these cases is probably due to the influence of falling particles. This effect is investigated in Section 6.5.6.

6.5.5 Comparison between sub-tropics and mid-latitudes

Layered clouds in the sub-tropics and in mid-latitudes occur under very different meteorological conditions. In mid-latitudes, they mainly follow frontal systems, in the sub-tropics the influence of gravity waves generated from deep convective systems may be a more prominent driver. Figure 6.20 compares the statistical distributions of the first to fourth distribution moments retrieved from the single cases. It is visible that the overall statistical parameters of both datasets are very similar and no significant differences can be found for the first three moments. Only the fourth moment (kurtosis), which describes an excess in the outer parts of the histogram, is considerably larger

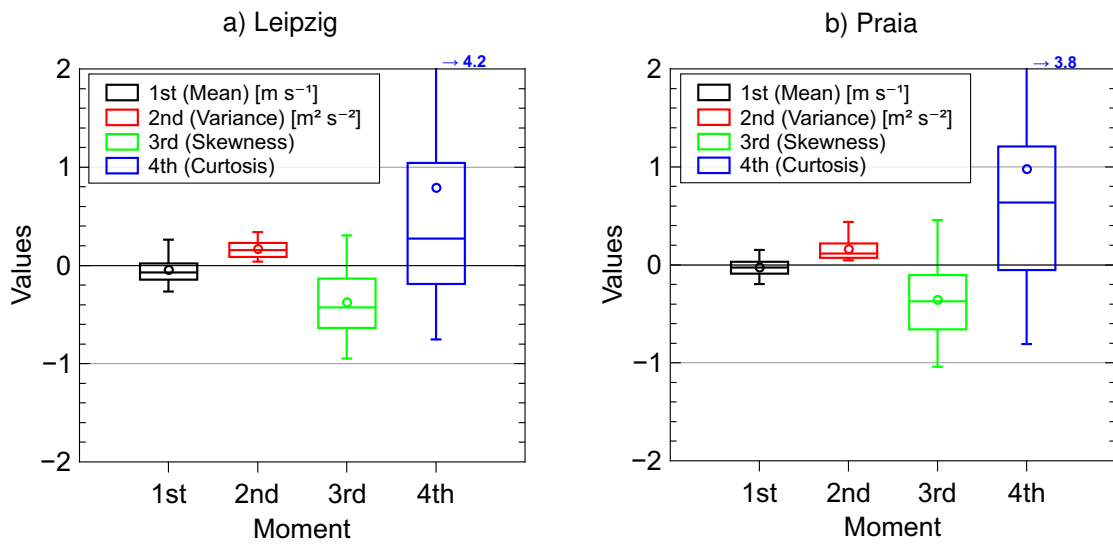


Figure 6.20: Comparison of first to fourth statistical moments of the vertical velocities for all cloud cases recorded at Leipzig (a) and Praia (b). Large boxes indicate the 25% and 75% percentiles around the mean values (circles), while the bars show the 5% and 95% percentiles.

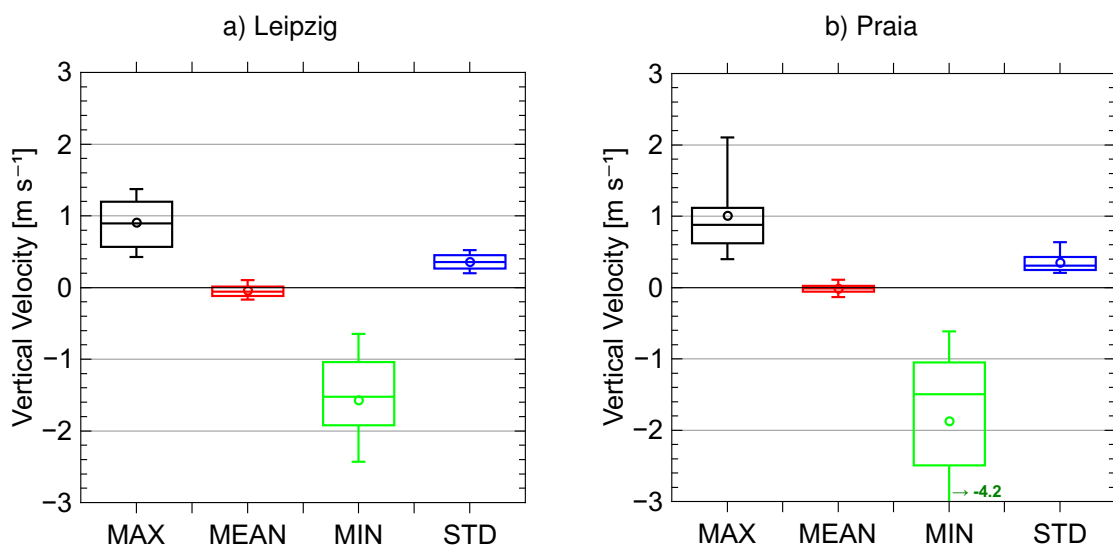


Figure 6.21: Comparison of the minimum (MIN), maximum (MAX), mean (MEAN) and standard deviation (STD) of the vertical-velocity distributions recorded at Leipzig (a) and Praia (b). The statistics consist of the single values derived for each cloud case. Large boxes indicate the 25% and 75% percentiles around the mean values (circles), while the bars show the 5% and 95% percentiles.

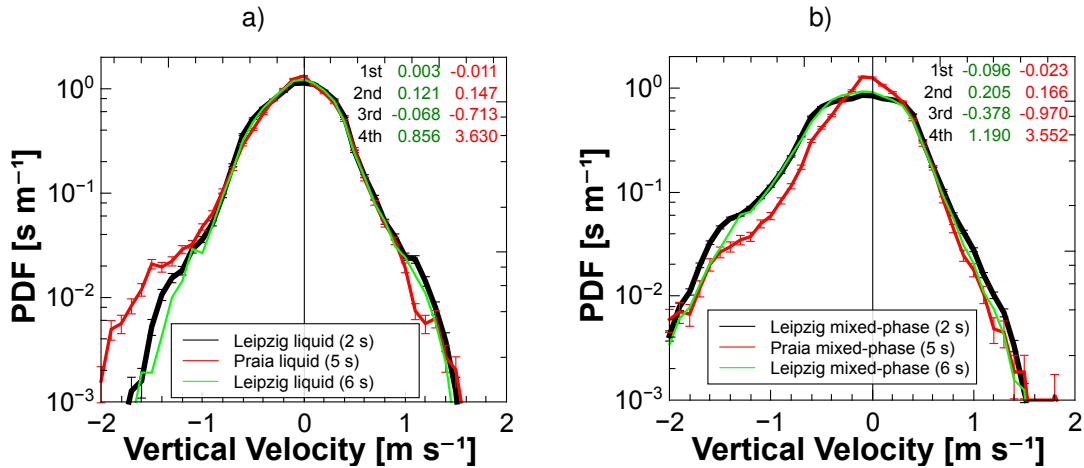


Figure 6.22: PDFs of the vertical velocities at cloud base measured with WiLi at Leipzig and at Praia for supercooled liquid (a) and mixed-phase cloud layers (b).

for the clouds at Praia. Hence, the distribution is deviating stronger from a Gaussian shape at high vertical velocities. Further distributions of maximum, minimum, mean and standard deviation are shown in Fig. 6.21. Before selection of the absolute minimum and maximum, a 3-bin median filter was applied on each cloud case to avoid noise artifacts. Strongest differences can be found here in the maximum and minimum values, which corresponds to the differences found in the kurtosis. The kurtosis increases rapidly, if such outliers are present within the dataset. Differences are mainly visible in the higher moments. This discrepancy probably results from a low amount of very high vertical-velocity values, measured at Praia. Occasional strong wave motion in the upper troposphere could influence the vertical-velocity pattern in the sub-tropical clouds.

In Figure 6.22 the vertical velocities at cloud bases are compared for the datasets from Leipzig (UDINE) and Praia (SAMUM-2). The values of UDINE were averaged on a 6-s timegrid to better compare to the 5-s timegrid used in the SAMUM-2 experiment. A further classification beyond mixed-phase and liquid clouds, as shown before, is not done in this case, because the number of cases is not sufficient and the significance of the statistics would be too low. Statistical moments are given in the figure. For liquid clouds, both statistics are nearly identical. Significant differences show up only for mixed-phase clouds at negative vertical-velocities. The right flanks of the vertical-velocity histograms from Leipzig and Praia are very similar in both cases. For liquid cases, PDF values agree within 5% in the range from -0.9 to 0.9 m s^{-1} . That is an amazing result, given the fact that the two datasets were recorded about 5000 km and 5 years apart. The updraft statistics in the panel shown in Fig. 6.19 and the height- and temperature-resolved histograms in Fig. 6.18a are also very similar. The physical process behind the generation of these clouds, therefore, appears to be universal. Once formed, layered clouds seem to be largely independent structures, kept alive by their internal motion.

6.5.6 Investigation of the excess at negative vertical velocities

In the previous sections, it was shown that the statistics of vertical velocities at cloud base can be easily derived for non-precipitating clouds (see Fig. 6.19 and 6.22). For precipitating clouds the derivation of meaningful statistical properties is more difficult, because falling particles partially mask the movements of the small cloud droplets at cloud base. Such effects can be seen, e.g., in Fig. 6.22b, where an excess at negative vertical velocities is visible. That excess may originate from downdraft regions within the cloud, where cloud droplets have dissolved and only the falling ice crystals are left to produce a Doppler lidar signal. One can assume that the vertical air movements in these areas of the cloud are statistically not different from the rest of the cloud.

In Fig. 6.23 it is, therefore, attempted to reproduce the statistics of mixed-phase clouds from the statistics in pure liquid clouds. This approach is based on the assumption that in mixed-phase cloud layers falling ice crystals, drizzle droplets and cloud droplets are subject to the same turbulent motion. The vertical-velocity statistics of falling particles is just offset by their fall velocity (see Fig. 6.16). The vertical-velocity statistics of mixed-phase clouds should, therefore, be reproducible from the statistics of non-precipitating clouds by just adding up different shifted modes. It is visible from Fig. 6.23 that the statistical distribution of mixed-phase clouds is matched closely assuming two additional

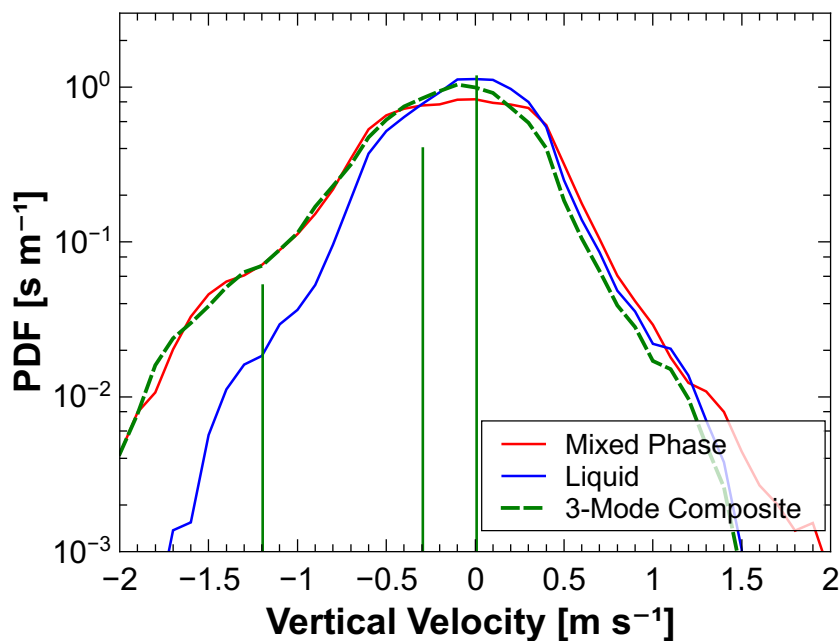


Figure 6.23: The histogram of vertical velocities at the base of liquid clouds at Leipzig (blue curve) is used to reproduce the same statistics in mixed-phase clouds (red curve) assuming additional modes resulting from falling particles (green vertical lines). At the position of the green vertical bars, the blue curve is added with the corresponding weightings of the bars, which are 1.0 for the droplet mode at 0 m s^{-1} , 0.4 for the first falling particle mode at -0.3 m s^{-1} and 0.06 for the third particle mode at -1.2 m s^{-1} . The resulting distribution is renormalized and displayed as the dashed green line.

modes of falling particles. This finding finally explains the excess at negative velocity as particle-influenced and indicates that the velocity distribution is similar even for precipitating mixed-phase clouds and non-precipitating liquid clouds. It is also visible from Fig. 6.23 that the influence of falling-particle modes on the right flank (updrafts) of the PDF is limited.

7 Towards the measurement of ice-particle flux from cloud-radar spectra

In the previous chapters, it has been shown what new and exciting synergistic effects show up, when combining different velocity-resolving instruments. Especially Doppler lidar and cloud radar were found to perform well together, but also the addition of a wind profiler showed that this combination of instruments has a lot of uncharted potential. A precise and unbiased measurement of vertical velocity makes it, e.g., possible to directly derive information about size and shape of particles. However, it is extremely difficult to observe processes within the top layer of the cloud, because liquid droplets and ice crystals coexist in the observation volume and are in turbulent motion. The processes within the cloud layer itself, which are vital for the understanding of heterogeneous ice formation, are therefore hidden.

In this chapter, an approach is described to detect and quantify heterogeneous ice nucleation at cloud top. A combination of Doppler lidar, cloud radar and wind profiler is used to capture the vertical motions at cloud base and inside a mixed-phase cloud layer and to separate liquid droplets and ice crystals by their fall velocities. A major problem is the strong turbulence within the mixed-phase layers, which distorts the cloud-radar spectra. The turbulent and instrumental distortions of the radar spectra are therefore measured with the help of a wind profiler and/or a Doppler lidar. Subsequently, the detected distortions are removed with the help of a deconvolution technique, similar to the one introduced in Section 5.1. The velocity scale of the spectra can then be directly converted to particle sizes, using the approach of Heymsfield and Westbrook [2010] presented in Section 3.2.4.

In Section 7.1, it is shown that the process of ice nucleation can be sensed remotely, if the flux of ice particles through the cloud base can be quantified. A way towards the derivation of the particle flux from cloud-radar spectra is explained in Section 7.2. A deconvolution method to correct distorted cloud-radar spectra is presented in Section 7.3. Treated spectra are used in Section 7.4 to derive microphysical information about the falling particles. The retrieval of the particle size distribution is attempted directly from the reconstructed cloud-radar spectra, using information from multiple measurement systems to remove disturbances and shifts introduced by vertical motion. Measurement uncertainties and potential further developments of the method are discussed in Section 7.6.

Vertical-velocity information has already been used before in the study of high clouds

[Matrosov et al., 2002; Mace et al., 2002; Deng and Mace, 2006, 2008]. Heymsfield and Iaquinta [2000] employed such a method to gain insight into the climatology of cirrus clouds and particle transport mechanisms. A first application to low clouds was done by Seifert et al. [2012]. Westbrook et al. [2007] and Luke and Kollias [2013] presented methods to separate cloud droplets and drizzle. The aforementioned methods use moments, derived from radar spectra, thereby assuming a certain size or velocity distribution. Protat and Williams [2011] used a combination of a 3-GHz Doppler radar and a 50-MHz wind-profiler to validate statistical relationships between terminal fall velocity and radar signal, but left the size information implicit. Recently, Westbrook and Illingworth [2013] measured particle flux with aircraft within an arctic mixed-phase cloud layer. The method presented here is solely based on ground-based remote-sensing techniques and does not make any assumptions on particle size distribution. All information is retrieved directly from corrected cloud-radar spectra. The synthesis of measurements from Doppler lidar, cloud radar and wind profiler on the scales of single measurement volumes has never been done before. In the context of this work, it is shown that this combination of instruments can provide crucial information to approach the remote sensing of ice nucleation. The method must, however, not stand apart from the other methods mentioned above. It can be used with any of them, by just delivering treated radar spectra to them to improve the quality of the input data.

7.1 A measure for the particle nucleation rate accessible by remote sensing

It has been shown before that ice particles and water droplets can be observed by both lidars and radars. However, it is extremely difficult to observe the process of ice nucleation itself, i.e., the moment when a water droplet turns into an ice particle. This process is therefore mainly studied in laboratories [Phillips et al., 2013], where the number of supercooled droplets can be controlled and the generated ice crystals can be studied in situ. Unfortunately, experimental validation of such experiments in nature is largely missing. This lack of data is mainly due to the fact that the process is hidden inside the mixed-phase cloud top layer and unaccessible by established remote-sensing methods. It is already difficult to even find an observable parameter that is useful to quantify the process of ice nucleation. Fig. 7.1 illustrates this problem by showing two scenarios, in which ice particles are generated from liquid-water droplets within the cloud top layer. They subsequently begin to fall through the layer, until they appear at cloud base. The sketch makes clear, why it is not enough to measure particle number concentration alone. The number concentrations of ice particles directly below cloud base differ by a factor of five between the two scenarios, but the flux $F = N \times v$ of particles is equally $1 \text{ m}^{-2} \text{ s}^{-1}$ in both cases. Hence, the rate of ice production in the cloud top layer is the same, but in the second case particle growth and deposition happen faster.

When the particle number concentration can be measured together with the terminal

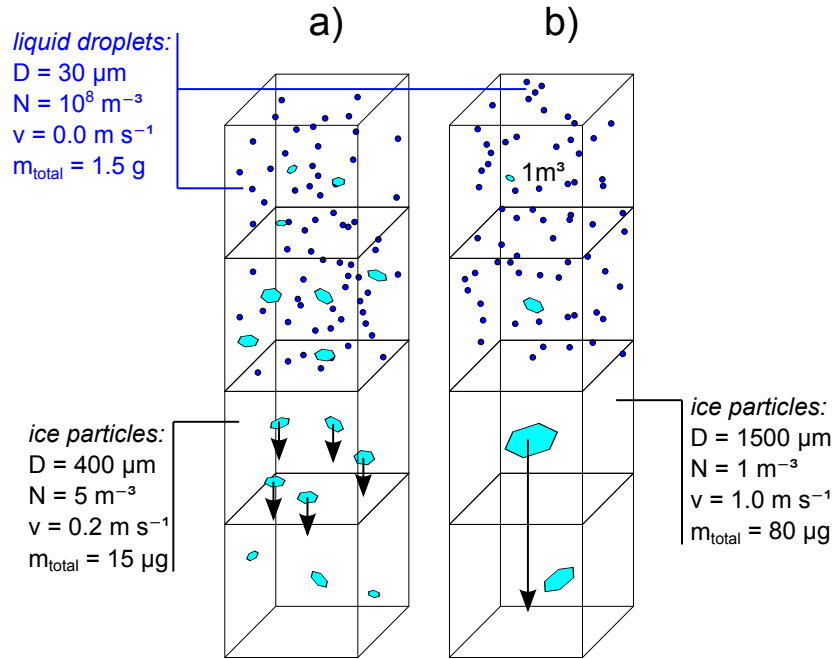


Figure 7.1: Illustration of the difficulties occurring in quantification of heterogeneous ice formation.

fall velocities, the total particle flux $F = \int N(D)v(D) dD$ can be calculated. F indicates the number of particles leaving the cloud base in each second, a quantity that is directly linked to the number of particles generated within the cloud top layer in each second. It is important to catch the particles directly at cloud base at the latest, because further downwards in the virga they are altered, e.g., by evaporation processes and consequently their number and shape is changed. It is even more important, although extremely difficult, to separate the ice and water particles within the liquid cloud layer, to restrict the location where ice nucleation happens.

It has been demonstrated in Chapter 3 that the MIRA-35 cloud radar can detect particle number concentrations of about 1 m^{-3} , if $D_m \approx 300 \mu\text{m}$. Recently, it has been shown by Schmidt et al. [2013] that the number concentration of liquid droplets in a layered cloud can be measured with a dual-field-of-view (DFOV) Raman lidar. In AC cloud layers, droplet number concentrations of 10^8 m^{-3} were found with that technique [Schmidt et al., 2014]. Consequently, ratios between ice and water particles on the order of 10^{-8} can be measured with a combined lidar/radar approach. The particle flux and the particle nucleation rate would be on the same order of magnitude, if particle fall velocities of approximately 0.5 m s^{-1} to 1.0 m s^{-1} are assumed. Currently, there is no experimental method available that can measure such low particle nucleation rates in reasonable time, motivating further efforts into this direction.

7.2 Deriving ice-particle flux from cloud-radar spectra

The cloud radar collects the backscatter signal of all particles moving with the same velocity in one spectral bin. The velocity of the n -th bin is $v(n) = n \Delta v$ (with $n = -128 \dots 128$). (Even though a discrete quantity, the velocity scale of the cloud radar is denoted in the form $v(n)$ to avoid misunderstandings with other indices introduced before). For this work, the MIRA-35 cloud radars of LACROS and MOL were run with $\Delta v = 0.08 \text{ m s}^{-1}$. If any spectral broadening has been corrected, $v_t(n) = -(v(n) - \bar{u}_z)$ (with \bar{u}_z the mean vertical velocity of air in the cloud radar observation volume during integration time) represents the terminal fall velocity relative to the surrounding air. The connection between terminal fall velocity and the maximum diameter D_m has been explored in Section 3.2.4. A monotonically increasing and steady function $v_t(D_m)$ (Eq. (3.24)) can be inverted numerically to derive $D_m(v_t(n)) = D_m(n)$ and, consequently,

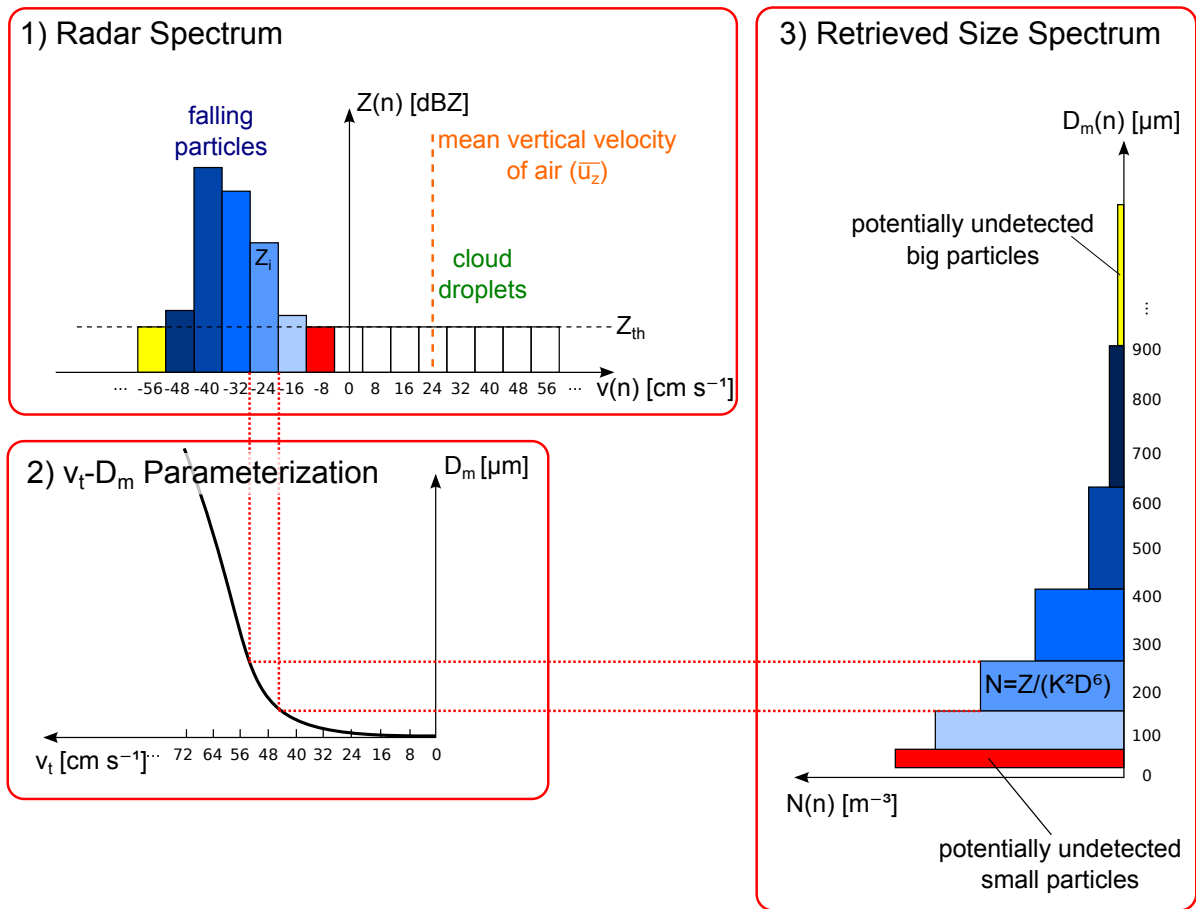


Figure 7.2: Overview about the proposed scheme to derive number concentration from cloud-radar spectra and measured terminal fall velocity v . It is assumed that all turbulence and instrumental effects are removed from the spectrum and only the vertical-velocity bias is left. In this example an updraft of 0.24 m s^{-1} is shifting the spectrum towards larger vertical velocities. If the vertical velocity of air is known, the size of the particles can be estimated from $v_t = -(v - \bar{u}_z)$.

$A_p(D_m)$ and $m_p(D_m)$ of the particles.

The spectral bin n of the cloud radar contains particles with the radar scattering cross section

$$\eta(n) = N(n)4\pi s_{180^\circ}^R(m_p(D_m(n))), \quad (7.1)$$

assuming a signal from only one particle type within the bin. Rearranging for $N(n)$ and inserting Eq. (3.10) yields

$$N(n) = \frac{\pi^2 \rho_{w,i}^2 Z(n)}{36 K_{w,i}^2 m_p^2(D_m(n))}. \quad (7.2)$$

Other observable parameters like particle flux

$$F = \sum_n N(n)v(n), \quad (7.3)$$

optical particle extinction coefficient

$$\alpha = \sum_n 2N(n)A_p(n) \quad (7.4)$$

and

$$\text{IWC} = \sum_n m_p(n) \quad (7.5)$$

(where n must only run over bins, where ice is present) can be calculated from the size spectrum with the known particle properties. For the calculation of F , it is of great advantage to have the information about number concentration and terminal fall-velocity on the same grid.

7.3 Preparation of cloud-radar spectra

Measuring the particle flux F calls for precise knowledge of the particle size distribution together with the spectral distribution of fall velocities. The velocity-resolved spectra of the MIRA-35 cloud radar do not directly represent the particles' terminal fall velocities. The velocity scale is shifted by mean vertical movements and broadened by a variety of phenomena occurring in the observation volume. There are several factors distorting the true vertical-velocity spectrum:

- Sub-scale turbulence σ_t^2 broadens the spectrum of any radar system, because of turbulent motion on scales smaller than the observation volume.
- Particles at the edge of any radar observation volume are observed under a small

angle. This effect introduces the variance

$$\sigma_b^2 = \frac{u_a^2 \phi^2}{2.76}, \quad (7.6)$$

with opening angle ϕ of the radar system and the advection speed u_a [Shupe et al., 2008] and is called beam-width broadening.

- During data processing, an FFT window is applied to reduce noise. Consequently, an additional distortion is introduced into the spectrum. This broadening is small compared with the other ones, but it has a non-Gaussian shape and must, therefore, be treated separately.
- Shupe et al. [2008] also list broadening due to wind shear, but consider it less important. Therefore, it is neglected here.

Unfortunately, the cloud radar needs a relatively long integration time to reduce electronic noise. With increasing integration time, however, the contamination of the radar spectra by the above-mentioned effects increases. Thus, any broadening effects and shifts have to be removed before any method relating microphysical properties of particles to their fall velocity can be applied to the cloud-radar spectra. The measurement and correction of the velocity scale is done by subtracting the mean vertical velocity of air as demonstrated in Section 5.5.1.2. The reconstruction of the true spectral velocity distribution is more difficult [e.g., Westbrook et al., 2007; Luke and Kollias, 2013]. If the mechanisms that have broadened the spectrum are known, a deconvolution like in Section 5.1 can be applied. The PSF responsible for the broadening has to be constructed from the different broadening mechanisms. One approach is to represent the spread by beam-width broadening (σ_b) and turbulence broadening (σ_t) by a Gaussian distribution

$$\text{PSF}_{bt}(v_n) = \left(\sigma_{bt}\sqrt{2\pi}\right)^{-1} \exp\left[-0.5\left(\frac{v_n}{\sigma_{bt}}\right)^2\right], \quad (7.7)$$

with the variance $\sigma_{bt}^2 = \sigma_b^2 + \sigma_t^2$. The PSF of the FFT window can be calculated analytically by Fourier transforming the window (in this case a Hann window). To acquire the total PSF, both functions are numerically convolved on the grid of the radar spectra and normalized in such a way that the sum of all points is 1. This normalization is necessary to conserve the total signal of the treated cloud-radar spectra. Fig. 7.3 shows an example PSF, which assumes $\sigma_b = 0.4$ and $\sigma_t = 0.3$. In the approach presented here, information about broadening and shifts that contaminated the measured velocity spectra are collected by Doppler lidar and wind profiler, measuring simultaneously with the cloud radar.

The RL algorithm is very sensitive towards deviations in the PSF, which is desired, because artifacts can be identified easily. If the assumed PSF is not correct, the deconvolution instantly fails or produces unrealistic results with the test function strongly deviating from the original signal. In this context, the compressed spectra of the cloud radar

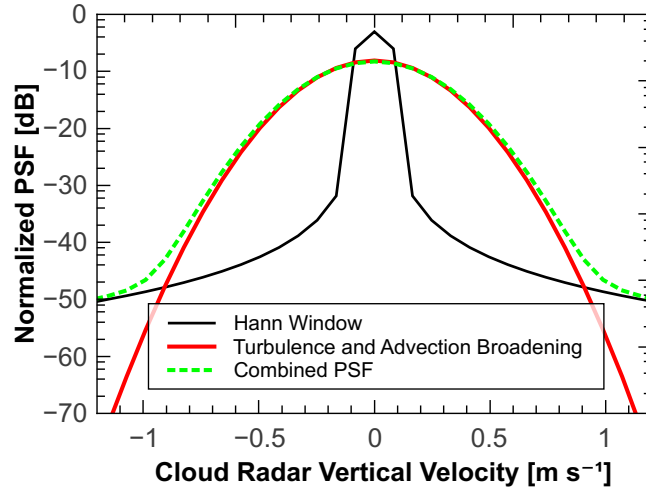


Figure 7.3: Total PSF composed from turbulence broadening, advection broadening and the windowing PSF.

can produce problems, because of the resulting sharp edges at small signal strengths. Therefore, empty spectral points are filled with a constant noise floor, reducing artifacts that would otherwise occur at these sharp edges.

7.4 Case studies

7.4.1 Combined Doppler lidar and cloud radar observations at cloud base

Figure 7.4 shows a mixed-phase cloud layer. The vertical velocity measured with Doppler lidar WiLi is used in this section to derive the parameters necessary to correct the cloud radar spectra. A relatively large advection speed of $u_a = 23 \text{ m s}^{-1}$, a cloud-top pressure of 518 hPa and a CTT of $-15 \text{ }^\circ\text{C}$ are derived from a GDAS radiosonde profile. WiLi indicates a vertical-velocity standard deviation of $\sigma_v = 0.65 \text{ m s}^{-1}$ for the complete cloud case. Fig. 7.5 shows the cloud-radar spectrum recorded at 5050 m height, during the updraft event marked in Fig. 7.4. There are two different ways conceivable to estimate the spectral broadening within the cloud radar observation volume. From the five vertical-velocity values measured with WiLi during the cloud radar measurement interval, a mean value of $\bar{v} = 0.97 \text{ m s}^{-1}$ and a standard deviation of $\sigma_t = 0.23 \text{ m s}^{-1}$ can be derived directly. Advection broadening of the cloud-radar spectra is $\sigma_b = 0.14 \text{ m s}^{-1}$. The combined broadening is $\sigma_{bt} = 0.27 \text{ m s}^{-1}$.

The turbulence broadening σ_t can also be estimated by a statistical approach, taking into account the turbulent energy spectrum. It can serve as a test of plausibility for the σ_t derived directly from the WiLi data. It was shown in Section 5.4 that turbulence is scale-dependent. After a measurement time of 10 s, Doppler lidar and cloud radar have only sensed turbulence on scales below $10 \text{ s} \times 23 \text{ m s}^{-1} = 230 \text{ m}$. The integral of

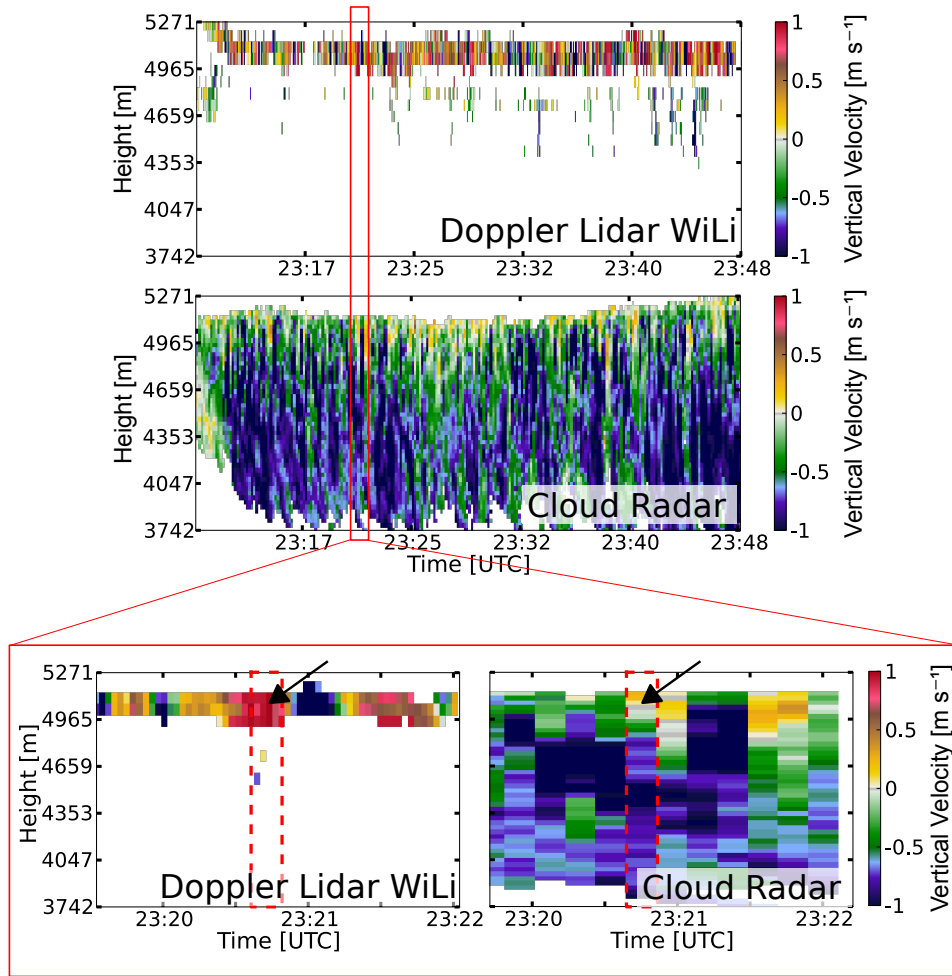


Figure 7.4: Vertical velocity at the cloud base (WiLi) and particle fall velocity (cloud radar). At the height of the black arrows, the cloud-radar spectrum and the mean vertical velocity from WiLi are extracted for the following analysis (see Fig. 7.5). The cloud layer was recorded at Leipzig on 17 September 2012.

the turbulent energy spectrum from $k = \frac{2\pi}{230 \text{ m}} = 0.026 \text{ m}^{-1}$ to the end of the spectrum yields $\sigma_t = 0.20 \text{ m s}^{-1}$, leading to a combined spectral broadening of $\sigma_{bt} = 0.24 \text{ m s}^{-1}$. Hence, the values for σ_{bt} from the direct and the statistical approach correspond within 12%.

The cloud-radar spectrum can be successfully deconvolved with both values. In Fig. 7.5, $\sigma_{bt} = 0.24 \text{ m s}^{-1}$ is used. The quality of the deconvolution is assured by the test function, which is the convolution of the deconvolved data with the PSF. It is drawn in green in Fig. 7.5 and corresponds well with the original cloud-radar spectrum ($R^2 > 0.997$). For the updraft event, a mode of presumably liquid particles becomes visible around the mean vertical-velocity measured with WiLi. The resulting spectrum may not yet be a perfect representation of the undisturbed cloud-radar spectrum, due to the uncertainties in the assumed PSF, but different peaks are visible now.

The example demonstrates that it is possible to separate different particle modes

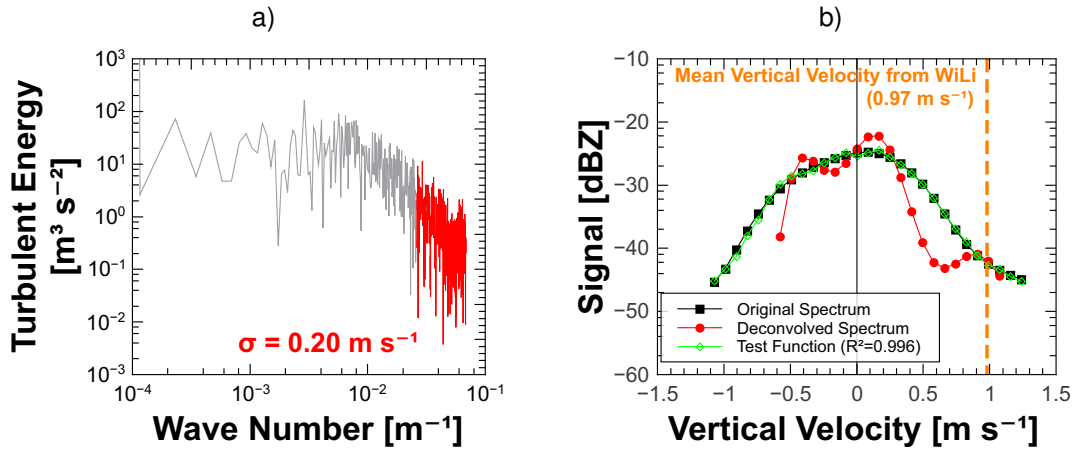


Figure 7.5: (a) Turbulent energy spectrum of the cloud presented in Fig. 7.4, derived from the vertical velocities measured with WiLi. The red part marks the scales below $k = 0.026 \text{ m}^{-1}$, which are smaller than the cloud radar observation volume. The total standard deviation contained in this part of the turbulent energy spectrum is $\sigma_t = 0.20 \text{ m s}^{-1}$. (b) Measured raw cloud-radar spectrum (black) and the same after deconvolution with $\sigma_{bt} = 0.24 \text{ m s}^{-1}$ (red). The test function is depicted in green. The mean vertical velocity measured with WiLi is marked with a dashed orange line.

from turbulence-broadened and velocity-shifted cloud-radar spectra, even within mixed-phase cloud layers and with an integration time of 10 s. Close to cloud base, independent information about the mean vertical velocity of the small water droplets within the cloud radar observation volume can be derived by Doppler lidar. At the same time, turbulence broadening can be estimated from Doppler lidar measurements to remove the broadening from the cloud-radar spectra by deconvolution.

7.4.2 Combined wind profiler, cloud radar and Doppler lidar approach to probe deep liquid cloud layers

In the previous section, it was demonstrated, how a combination of Doppler lidar and cloud radar can be used to separate liquid and ice particles at the cloud base of a turbulent cloud layer. In the following, the combination of MOL cloud radar, MOL Doppler lidar and the wind profiler is used to apply the same method to a thick cloud layer, which cannot be penetrated completely by lidar. The case under study is depicted in Fig. 7.6. It shows a mixed-phase mid-level cloud layer recorded at MOL on 25 September 2013. The wind profiler delivers the desired information about turbulence broadening and vertical velocity around the observation volume of the cloud radar. Unfortunately, the measurement interval of the wind profiler is longer (10 s) than that of the MOL Doppler lidar (2 s) and has a larger observation volume (see Fig. 5.19).

Measurements with this combination of instruments are presented in Fig. 7.7. Independent information about fall velocity (cloud radar), vertical air movement (wind profiler and Doppler lidar) and spectral broadening (wind profiler) is derived simulta-

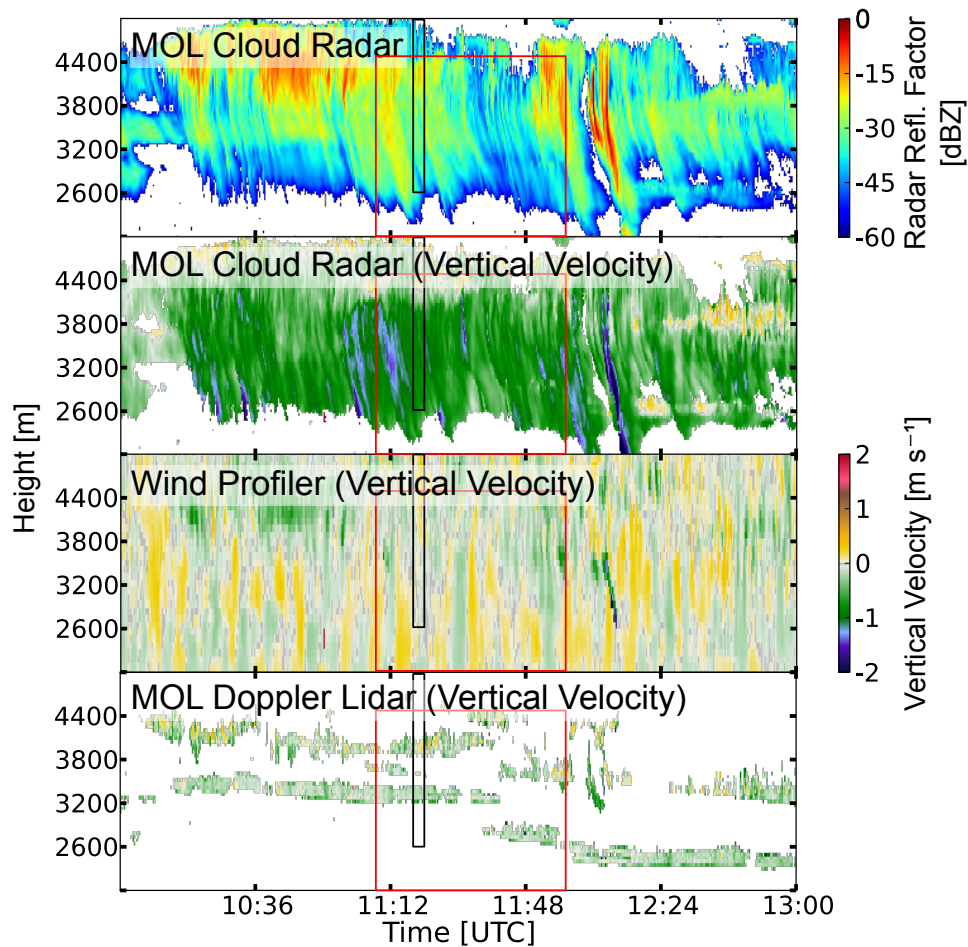


Figure 7.6: Combined measurement with vertically looking MOL cloud radar, wind profiler and MOL Doppler lidar at MOL on 25 September 2013.

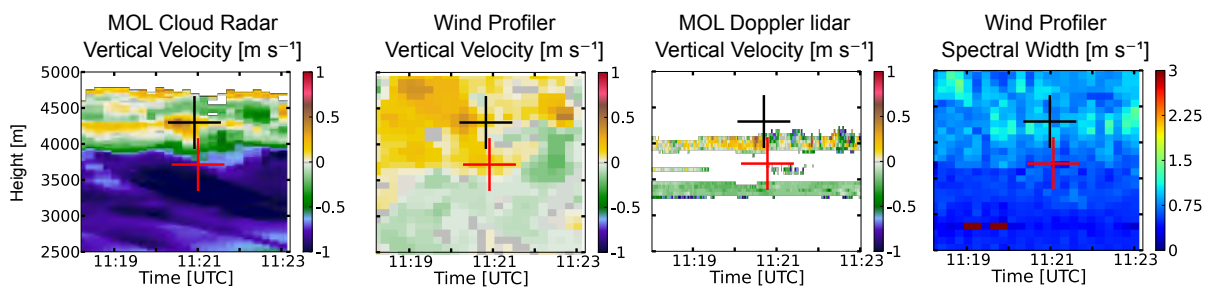


Figure 7.7: Extract from black box in Fig. 7.6 to give a detailed look into the vertical velocity and spectral width measured with MOL Doppler lidar, MOL cloud radar and wind profiler. The crosses indicate the positions of the spectra in Fig. 7.9 and 7.10.

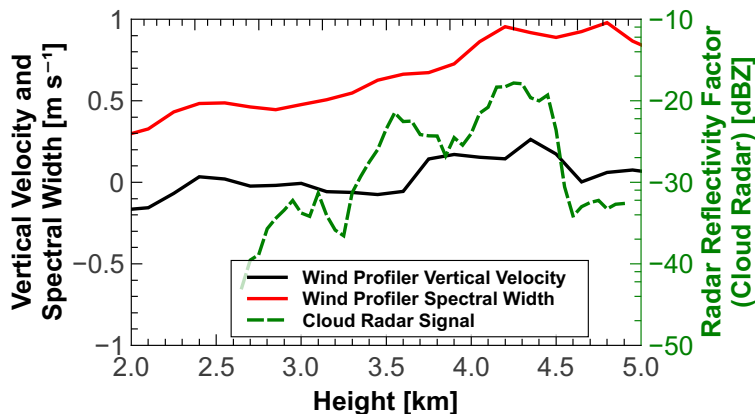


Figure 7.8: Profiles of wind profiler spectral width with correction for advection broadening (red), wind profiler vertical velocity (black) and radar reflectivity factor from cloud radar (dashed green) from Fig. 7.7 at 11:21 UTC.

neously. Fig. 7.8 shows profiles of vertical air velocity (black line) and spectral width (red line) from the wind profiler combined with the signal strength of the cloud radar (green line). A profile at 11:21 UTC is depicted. The opening angle of the wind profiler is 3.0° and with the help of a GDAS radiosonde profile the advection speed is estimated to $u_a = 3.0 \text{ m s}^{-1}$. Fig. 7.8 shows that the spectral width from the wind profiler is not influenced by big particles detected by the cloud radar. Above 5.0 km height, a drop is visible in the the signal of the cloud radar, but the wind profiler continues to show a spectral width of about 0.7 m s^{-1} , indicating turbulence as the reason for the spectral broadening. At 4.0 km height, a spectral width of 0.6 m s^{-1} is measured. The mean 10-s standard deviation of the vertical velocity measured with Doppler lidar is also about 0.6 m s^{-1} within the turbulent layer at 4.0 km height.

Figures 7.9 and 7.10 show the cloud-radar spectra and the retrieved particle properties from the points marked in Fig. 7.7 with a black and a red cross, respectively. At the height where the black cross is located, the wind profiler shows an average spectral width of $w = 0.85 \text{ m s}^{-1}$, strongly varying over the time interval depicted in Fig. 7.7. From the spectral width w , the turbulence component can be estimated to be $\sigma_t = \sqrt{(w/2.4)^2 - 0.14^2} = 0.36 \text{ m s}^{-1}$, assuming a Gaussian peak and correcting for the beam-width broadening of the wind profiler of 0.14 m s^{-1} . The beam-width broadening of the MOL cloud radar is $\sigma_b \approx 0.02 \text{ m s}^{-1}$, which has negligible influence on the resulting $\sigma_{bt} = 0.36 \text{ m s}^{-1}$. For this combined broadening, the deconvolution fails with the test function strongly deviating from the original spectrum ($R^2 = 0.80$). A successful deconvolution is possible up to $\sigma_{bt} = 0.2 \text{ m s}^{-1}$ as shown in Fig. 7.9a. In this figure, one peak around 0.3 m s^{-1} vertical velocity and another separated peak around -0.6 m s^{-1} are revealed. There may be a third peak close to 0.0 m s^{-1} . The reconstruction of a size distribution with Eq. (7.2) from the deconvolved cloud-radar spectrum is shown in Fig. 7.9b. The mean vertical velocity (orange dashed line in Fig. 7.9a) was applied to estimate the pure terminal fall velocities of the particles relative to the surrounding air. A mode of

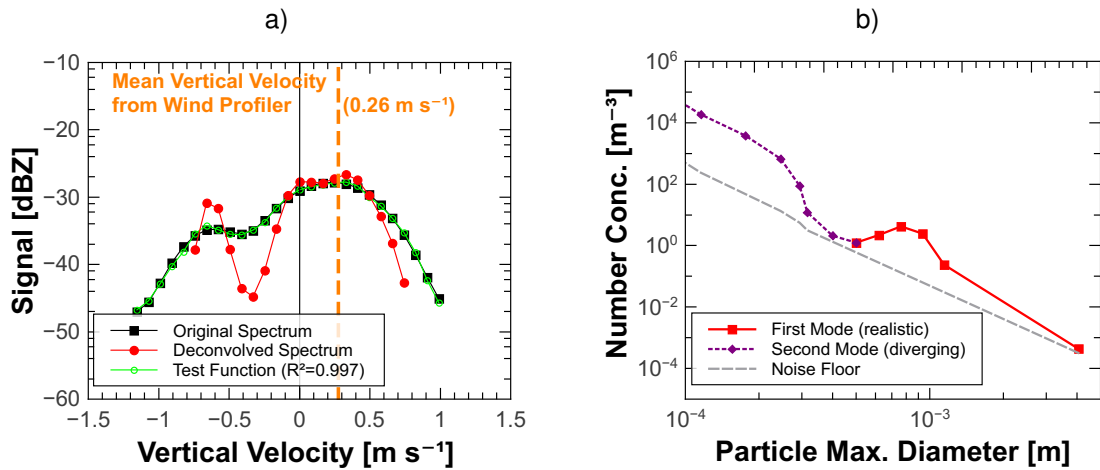


Figure 7.9: a) Raw radar spectrum (black line) and deconvolved one (red line) for the position of the black cross in Fig. 7.8. b) Number concentrations derived from the deconvolved spectrum, assuming that only hexagonal columns are present.

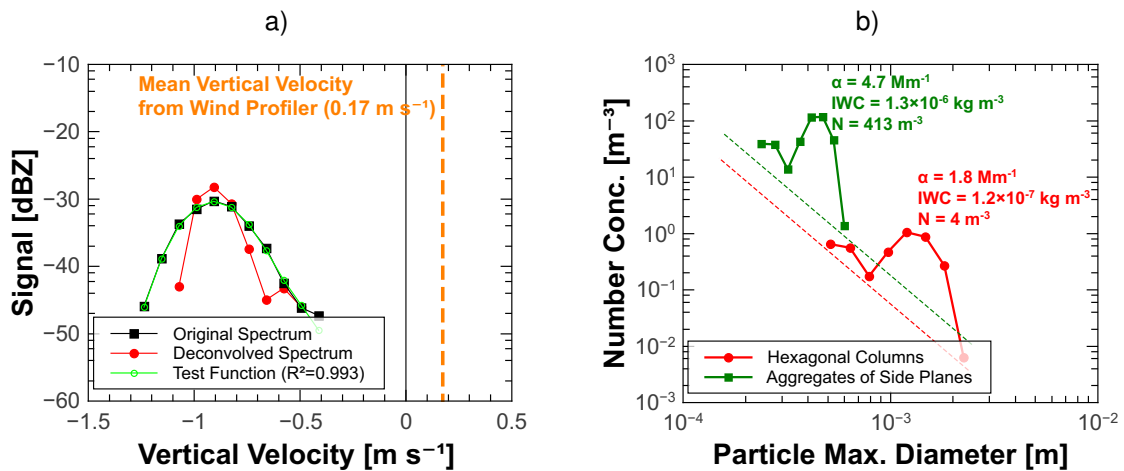


Figure 7.10: Same as Fig. 7.9, but for the position of the red cross in Fig. 7.7. The total signal in the cloud-radar spectrum is -24 dBZ. The retrieval of particle number concentration was done in (b) for two different particle parameterizations. The noise floors are indicated for both size distributions with dashed lines. The range of validity for aggregates of side planes is 600 to 4100 μm , the resulting size distribution for this particle type is slightly outside this range.

large particles is reconstructed around $D_m \approx 1$ mm. Thus, it remains unclear, if those particles are large ice crystals or perhaps drizzle droplets. The signal strength of the radar is too low to measure a meaningful depolarization signal, and particles disappear before crossing the height of $T = 0$ °C. The second peak diverges at smaller particle sizes, because it reaches up to positive vertical velocities.

Fig. 7.10a shows the same procedure applied to the point indicated by the red cross. At this height, the wind profiler shows a spectral width of 0.50 ms^{-1} , also strongly varying between single profiles. From that value, $\sigma_{bt} = 0.15$ ms^{-1} is calculated. The cloud-radar spectrum is successfully deconvolved with $\sigma_{bt} = 0.1$ ms^{-1} ($R^2 = 0.993$). The retrieved particle spectrum is shown in Fig. 7.10b for the two different particle types hexagonal columns and aggregates of side planes. It is visible from Fig. 3.4 that these two particle types represent two extreme possibilities exhibiting significantly different fall velocities for the same particle maximum diameter.

The retrieved size distribution is tested using the method of Hogan et al. [2006]. At 3800 m height (red cross) the radar reflectivity measured with the cloud radar is -24 dBZ, and a temperature of -8 °C was derived from a GDAS radiosonde profile. With these values Eq. (6.1) yields $\alpha = 28 \pm 14$ Mm^{-1} , and from Eq. (6.2) $\text{IWC} = (7.3 \pm 3.7) \times 10^{-7}$ kg m^{-3} is derived. α and IWC derived from the spectra by Eqs. (7.4) and (7.5) are shown in Fig. 7.10b. For hexagonal columns, α and IWC are one order of magnitude too low. For aggregates of side planes, IWC is 50% too high and α is also one order of magnitude too low.

The derived IWC values for aggregates of side planes are within the uncertainty given by Hogan et al. [2006]. The reasons for deviations in the other values can be manifold. Hogan et al. [2006] use the mean of the vertical and horizontal dimension D_{vh} of an ice crystal to calculate particle properties and a mass and area parameterization, where $m_p \sim D_{vh}^{1.9}$ and $A_p \sim D_{vh}^{1.6}$. This procedure makes a direct comparison difficult. Also, an additional mode of small crystals is attached to the measured spectrum at low crystal sizes, where the optical particle imager is no longer sensitive. Those particles could also be missed by the cloud radar. Unfortunately, no powerful lidar was available at MOL at the time of the measurements, so no independent verification of the optical extinction values could be acquired. In future, comparison with methods like the one proposed by Tinel et al. [2005] will probably be possible. The following calculations use the parameterizations for hexagonal columns, keeping in mind that the number concentrations might be different for other particle types.

Fig. 7.11 shows particle number concentration N and particle flux F derived from all cloud-radar spectra in the time-height interval from 11:07 to 11:56 UTC and 2000 to 4500 m, indicated as a red rectangle in Fig. 7.6. Vertical-velocity values from the wind profiler are used to automatically correct the velocity scale of the cloud-radar spectra, so that it resembles the terminal fall velocity relative to the surrounding air. F and N in Fig. 7.11 are calculated from uncorrected and corrected terminal fall velocities. The imprint of the vertical air velocity is visible in the uncorrected values (left column). The fingerprint of the vertical air velocity is easily visible in the uncorrected spectra as an increase in number concentrations in updrafts and a decrease in downdrafts. This effect is significantly reduced by subtracting the vertical air velocity measured with wind

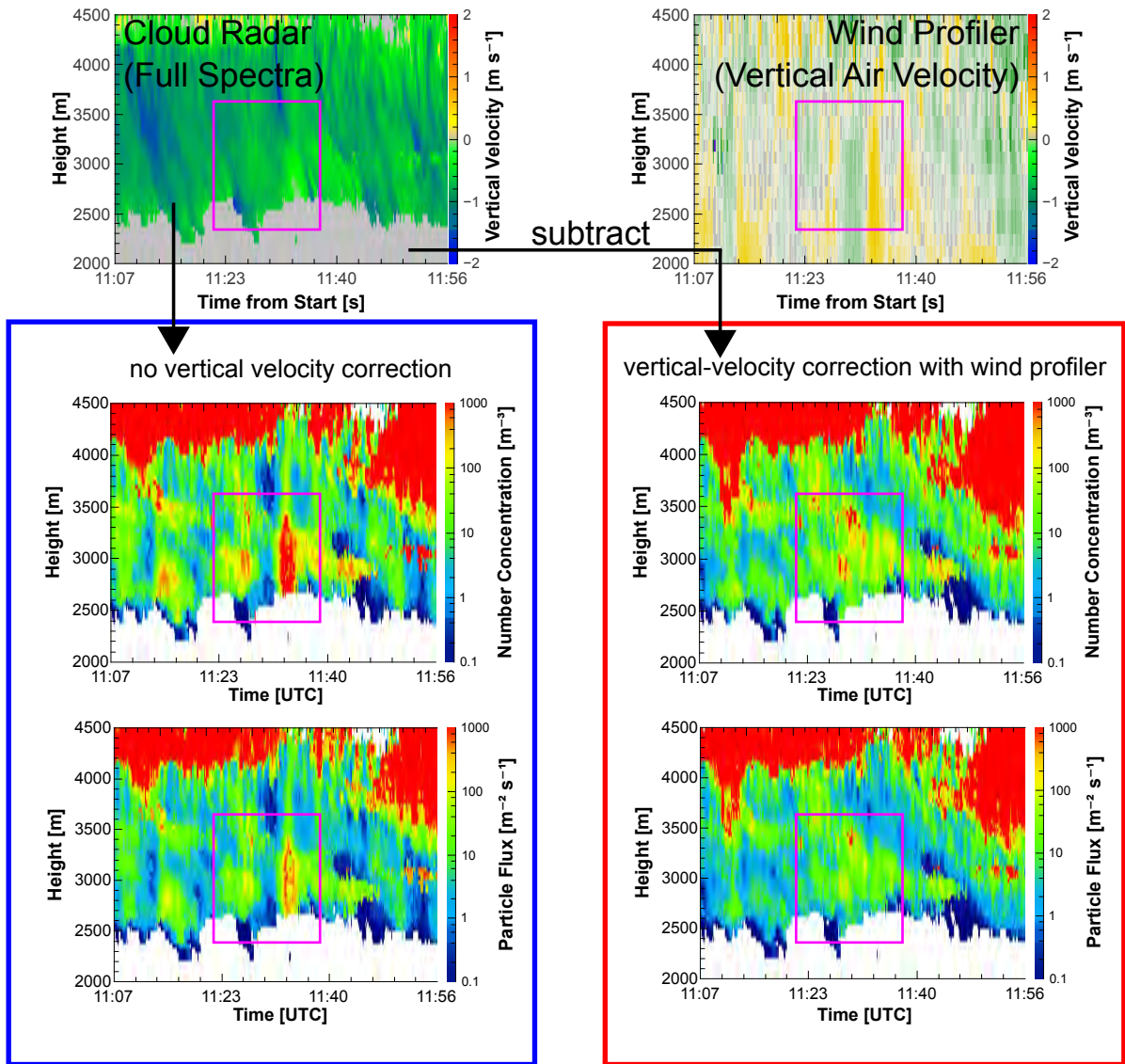


Figure 7.11: Comparison between the particle number concentration and particle flux retrieved with the deconvolution method for uncorrected (left blue box) and corrected (right red box) terminal-fall-velocity fields. Values are derived for hexagonal columns. The presented time-height section is marked in Fig. 7.6 with a red box.

profiler from the cloud-radar vertical velocity and is best visible in the area marked with a pink box. After correcting the vertical-velocity scale with the help of the wind profiler, coherent fall streaks become visible. The flux retrieved in this way refers to the movement of the particles relative to the surrounding air and is, therefore, only proportional to particle properties.

The width of the wind-profiler spectra is unfortunately not only connected with the strength of the turbulence and can be influenced by other factors like Rayleigh scattering from particles and strong signal gradients. It can be used for demonstration purposes (like in Fig. 7.7), but a use for automated deconvolution is more complicated. Therefore, the correction of broadening by deconvolution is kept simple and is run with a fixed $\sigma_{bt} = 0.1 \text{ m s}^{-1}$. Hence, the effect of this correction cannot reach its full potential in this example. The correction of the mean vertical velocity is far simpler and can be done automatically on the complete dataset. Also automatic peak separation for spectra in Fig. 7.9 is not yet implemented. Therefore, the method usually diverges, when a liquid-water mode is present and the cloud-radar spectra show signals at $v > 0$. The algorithm then produces unrealistically high number concentrations, as it was seen before in Fig. 7.9b.

7.5 Size separation of particles

In Fig. 7.12 the same measurement as in Fig. 7.11 is shown. In this figure, however, small and big particles are shown separately. This presentation efficiently removes any error due to overcounting of small particles, originating from an incomplete separation of the signals from ice crystals and liquid cloud droplets in the radar spectra. Streaks of large particles become visible, e.g., in Fig. 7.12c, falling through the cloud system. The tops of these streaks indicate the main levels of ice formation between 4000 and 4500 m height. However, the composition of these big particles remains unclear. They might be large ice crystals or liquid water droplets. In future, the application of particle classification methods including the depolarization ratio may resolve this issue. A height profile of mean particle flux is given in Fig. 7.13. At cloud top, the particle flux can be seen to increase. There, particles nucleate, grow and become detectable for the cloud radar. Between 3400 and 4000 m the flux is noisy, but roughly constant around $8 \text{ m}^{-2} \text{ s}^{-1}$. Below a height of 3000 m, where the particles presumably evaporate, the particle flux decreases.

7.6 Discussion of errors and scope of the method

It has been shown that the accurate measurement of terminal fall velocities is a crucial step towards the remote observation and quantification of heterogeneous ice formation. For this purpose the combination of Doppler lidar, cloud radar and wind profiler has been explored. The three instruments can – in theory – provide all necessary information to measure ice-particle flux at any height inside a mixed-phase cloud layer. Such a

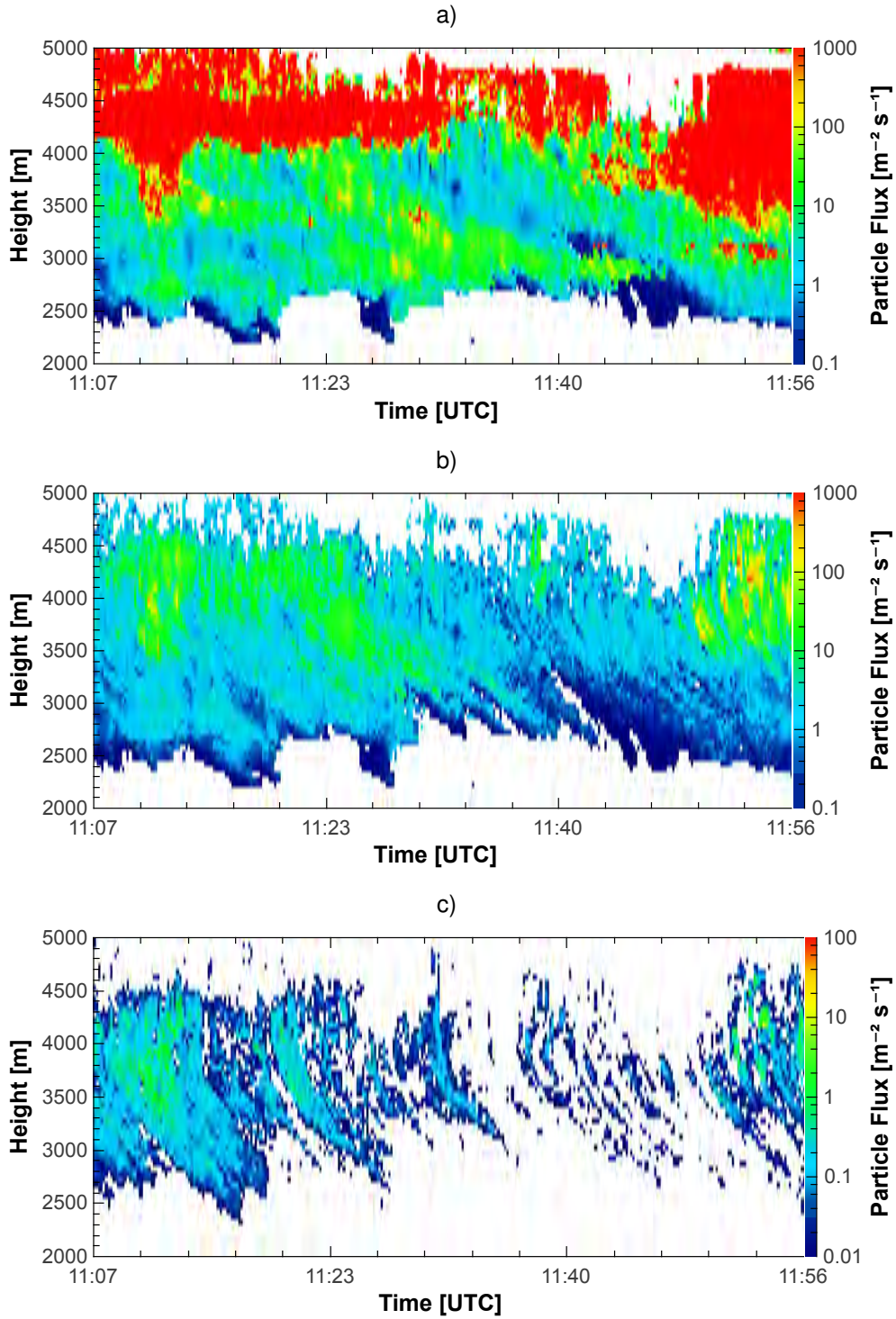


Figure 7.12: Particle flux calculated for different particle size ranges: (a) for the complete spectrum, (b) for particles larger than a diameter of 500 μm and (c) for particles larger than 2000 μm . The assumed particle types in this calculation are hexagonal columns, extended by rimed long columns for $D > 600 \mu\text{m}$. Note the different scale in (c).

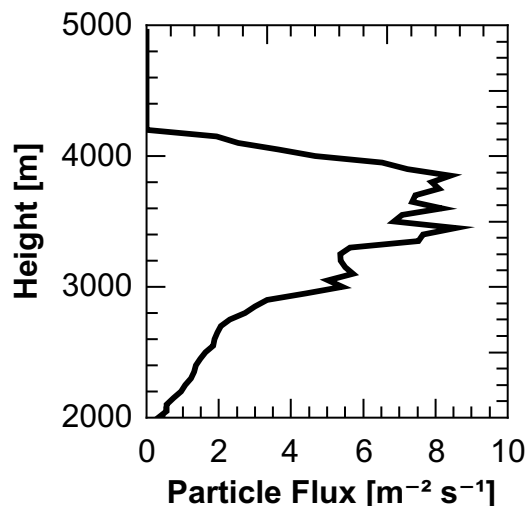


Figure 7.13: Profile of particle flux averaged from 11:07 to 11:40 UTC and from 2000 to 5000 m height for the measurement shown in Fig. 7.12.

combination of instruments can open the possibility to remotely observe ice crystals and cloud droplets independently, because turbulence broadening can be removed from the cloud-radar spectra by deconvolution with the help of vertical-velocity measurements from co-located Doppler lidar and wind profiler. Potential synergistic effects between the instruments are visualized in Fig. 7.14.

The presented method is only one way to remotely measure ice particle nucleation rate. The deconvolution operation used to remove turbulence broadening from the cloud-radar spectra can be used independently to only separate the ice and liquid-water modes. Existing methods can then be applied to retrieve particle properties with assumptions about the shape of the distribution [e.g., Frisch et al., 2002; Heymsfield and Iaquinta, 2000]. The method presented here can, however, be employed to retrieve particle size distributions without such assumptions.

One major uncertainty for the retrieval of particle flux is introduced by missing information about particle type. Efforts are taken, at the moment, to implement advanced particle typing methods, e.g., from Matrosov et al. [2012], into the LACROS cloud-radar algorithms [Alexander Myagkov, personal communication]. Particle typing by remote sensing will remain a challenge given the vast diversity of possible ice crystal shapes [Magono and Chung, 1966], but even very basic information about the shape of the particles (e.g., columnar or plate-like) will facilitate the selection of the correct particle type. The accuracy of the calculated radar reflectivity of a single ice particle also depends on crystal shape, giving the integration of particle typing methods even more significance. Hogan et al. [2006] state that the calculation of cloud radar signals by Eq. (3.9) is accurate within about 30% to 50%. As shown in Section 5.5.1.2, an error of 50% is introduced into the derived particle size, if the corrected vertical velocity is known with an accuracy of 0.2 m s^{-1} . According to Heymsfield and Iaquinta [2000], the

terminal fall velocities derived by their methods are accurate within at least 30% for the whole size range. Hence, the error sums up to more than one order of magnitude, but non of the single errors has to be considered a dead end. In future, cloud radar and Doppler lidar should always be placed directly next to each other to rule out any error due to non-matching observation volumes. More effort has to be put into the analysis of the relation between turbulent motion and the width of the wind-profiler spectrum in order to make this measurement quantity usable for deconvolution of the radar spectra. Chen and Chu [2011], e.g., pointed out that advection broadening does not necessarily produce a Gaussian-shaped broadening. Such a non-Gaussian broadening would be important for the synthesis of the combined PSF that is necessary for the deconvolution operation. Also, the large observation volume of the wind profiler has to be taken into account, with all its adverse effects, e.g., partial beam filling at short integration times [Kollias et al., 2013].

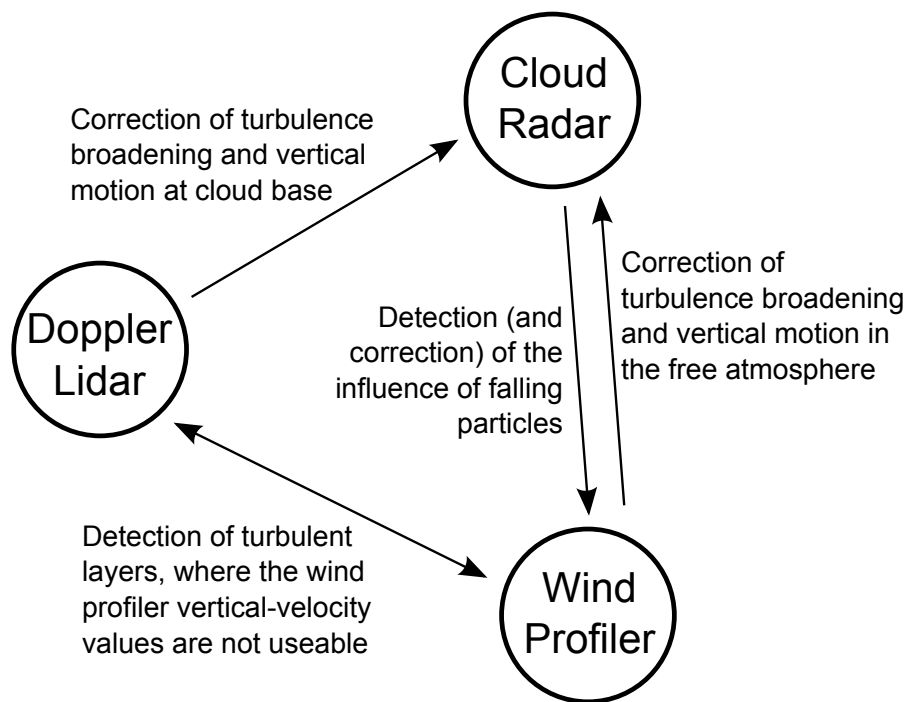


Figure 7.14: Schematic visualization of the potential synergy of Doppler lidar, cloud radar and wind profiler. Each arrow represents one possible correction step.

8 Summary, conclusions and outlook

8.1 Summary and conclusions

The present study paves the way towards the combined measurement of vertical velocity and heterogeneous ice formation in layered clouds. It was shown, how a combination of Doppler lidar, Raman/polarization lidar and cloud radar can be used to study the freezing behavior and vertical motions in layered clouds. For the first time, the synergistic measurements of Doppler lidar and cloud radar have been analyzed in detail.

Vertical velocities from the Doppler lidar were provided as a driving component to a cloud model. The model output, in turn, could be verified with cloud-radar measurements. The resulting IWC values were found to agree within one order of magnitude. This procedure yields a unique chance to study physical processes, hidden inside a mixed-phase cloud layer, on the basis of real measurements.

Doppler lidars have been found to struggle with the high signal gradient at cloud base, due to their long pulse length and adverse laser chirp effects. An iterative deconvolution method has been developed to correct Doppler-lidar data for those artifacts introduced by the laser pulse. The residual error was determined by simulations to be less than 0.02 m s^{-1} after only ten iteration steps. This technique brings the accuracy of TROPOS Doppler lidar WiLi into the range of 0.1 m s^{-1} and significantly reduces the measurement bias. It also allows, for the first time, the retrieval of height-resolved vertical-velocity measurements at cloud bases with unambiguous and independent information in neighboring range gates. Chirp-induced artifacts have been found in the data of Doppler lidar WiLi and in the Streamline Doppler lidar of MOL. The latter Doppler lidar series has been commercially available for years and is wide-spread in the atmospheric-science community. The deconvolution technique presented here is not restricted to any specific instrument. It could be easily used to correct the data of the HALO Doppler lidars, if the reference Doppler spectra of the laser pulse could be recorded.

After chirp correction, Doppler lidar and cloud radar were found to provide the vertical-velocity measurements in a non-precipitating cloud layer within the measurement accuracy of 0.1 m s^{-1} . The cloud radar values were shifted by -0.2 m s^{-1} at cloud base, in the first level where the cloud radar could detect a signal. This shift is probably due to the influence of a small number of large drizzle droplets falling through the cloud layer. For this analysis, vertical-velocity measurements of WiLi were interpolated on the 10-s timegrid of the cloud radar system. Below this time resolution, both systems were found to show the same turbulent-energy spectrum.

The datasets from UDINE and SAMUM-2 were extensively analyzed with respect to cloud freezing behavior and vertical-velocity statistics. For this purpose, the LARDA

software has been developed in order to have direct access to the data products of all LACROS measurement systems. Statistical differences between mid-latitudinal and subtropical layered clouds were found. Layered clouds were found to occur in different height ranges, but seem to prevail solely in the temperature range between 240 and 280 K in both regions. The clouds were sorted by a fixed cloud-classification scheme into liquid or mixed-phase clouds. From this data, it was found that the temperature at which 50% of all clouds are mixed-phase is -9 ± 3 °C for Leipzig. Cloudsat/CALIPSO satellite measurements confirm this finding. The introduction of a lidar particle detection threshold allowed the harmonization of the results with previous lidar-based studies at TROPOS. This finding is extremely useful, because it opens a way to level out the differences between lidar and radar observations. The value and the understanding of current and historical datasets is significantly increased. In a further, quantitative analysis of the ice and liquid-water masses in layered clouds, IWP and LWP were derived for all selected cloud cases, for which Cloudnet measurements were available. The IWP/CWP ratios in layered clouds showed that the mass ratio between ice and water can be as low as 10^{-4} , which occurs frequently at temperatures above -15 °C. The analysis gives an input to the first question, posed in Section 2.5, where the ratio of ice and liquid-water mass was found to crucially determine the microphysics of a mixed-phase cloud parcel.

Based on the cloud classification, the influence of falling particles on the Doppler lidar and cloud radar velocity measurements were analyzed. Strong influence of falling particles was found in the cloud-radar data, while the Doppler-lidar measurements seemed to be largely unaffected by the motion of falling particles for velocities between -0.9 and 0.9 m s^{-1} . Significant differences were only found for $v < -0.9$ m s^{-1} , however, affecting about 2% of the measurements. For the first time, different statistical moments of vertical motions were derived for layered clouds based on the classification of the cloud layers into liquid/mixed-phase and daytime/night-time occurrence. The mean values of the vertical velocity in all cloud types were found to deviate not more than ± 0.12 m s^{-1} from zero. The vertical-velocity variance has been found to be on average 0.21 $\text{m}^2 \text{s}^{-2}$ for all supercooled cloud layers. For liquid cloud layers a mean value of ± 0.003 m s^{-1} and a variance of 0.134 $\text{m}^2 \text{s}^{-2}$ was found. These efforts answer the second question, posed in Section 2.5, since they provide missing vertical-velocity statistics in layered clouds. The strengths of the deconvolution method gives high confidence in these parameters. It is worth noting again that no additional treatment – except of the deconvolution operation – was applied to the vertical-velocity values. The statistics were assembled from the measurement values as they were recorded by the measurement instrument. It is a good sign that the mean values lie so close to zero. An excess at negative vertical velocities in the statistics of mixed-phase clouds could be attributed to falling particles.

In a unique approach, a Doppler lidar, a cloud radar and a wind profiler were combined. Two main goals were reached. Firstly, the instruments were used to sense simultaneously the movements of large-scale gravity waves, small-scale turbulence, thermal updrafts and falling particles. The measurement of the terminal fall velocity of particles was enabled by correcting vertical velocities measured with cloud radar for vertical air motion with the help of the wind profiler. Secondly, a new technique was proposed to directly measure the ice-particle flux in a layered cloud. The technique independently measures the

broadening effects affecting the cloud-radar spectra with Doppler lidar or wind profiler. A deconvolution method is then used to remove the broadening from the spectra and restore separated particle modes. The retrieval of particle number concentration and, eventually, particle flux relies on the calculation of particle sizes from vertical-velocity measurements. The technique has been found to be applicable with a combination of Doppler lidar and cloud radar at cloud base. A combination of Doppler lidar, cloud radar and wind profiler was employed to even apply the method inside optically thick mixed-phase cloud layers. This effort approaches a frontier of current cloud-radar research and shows that substantial synergistic effects can be generated by combining the three measurement systems. The new method can help to quantify the effect of heterogeneous ice formation down to the influence of single particles by measuring the particle nucleation rate directly. In this way, remote atmospheric measurements and laboratory work could be better connected and directly compared for the first time.

The uncertainties of the retrieved particle number concentration and particle flux were found to be in the range of about two orders of magnitude. Missing particle classification and uncertainties in the geometric setup of the radar system were identified as potential problems. This deviation calls to put more effort into the further development of the technique. On the other hand, more simple data products that were developed in this context, like the vertical-velocity feature classification (see Fig. 5.20e), can already be used in this state of development.

8.2 Outlook

The importance of vertical motions in the atmosphere has been highlighted in this work. In an ever-changing physical system like the Earth's atmosphere, quantitative information about vertical movements is crucial for the understanding of physical processes. The focus of this work lies on vertical-velocity measurements at the base of layered clouds, but the techniques developed have a much broader range of possible application. Doppler lidar, cloud radar and wind profiler have been found to complement each other in a broad range of applications, reaching from the analysis of gravity waves to the derivation of microphysical products. It has also been shown that close inspection of the technical basics of the single systems is crucial. The data processing algorithms of Doppler lidar and cloud radar have been analyzed extensively.

The presented method for chirp removal enables Doppler-lidar systems equipped with pulse lasers of low complexity to reach very high velocity precisions in the range of 0.05 to 0.1 m s^{-1} . It could also be beneficial for the development of future Doppler lidar systems, because it relaxes the constraints on the pulse laser. The final precision is no longer determined by the chirp effect, but by other factors, e.g., the pointing stability of the scanning unit. The deconvolution technique is applied on the averaged spectra and can easily be applied on stored data or in real time during the measurement. Hence, no additional computational effort is necessary during data acquisition, which is especially interesting for systems with very high pulse repetition rates. Likewise, the technique could be used to remove the chirp influence from historical datasets, if only the averaged

spectra have been stored. The method works with arbitrary chirp and pulse shapes and can also be employed in chirp-free systems, simply to increase the range and frequency resolution.

The similarity of the vertical-velocity statistics of layered clouds in the mid-latitudes and sub-tropics is intriguing. This result indicates that the great diversity of ice-formation efficiencies measured in mixed-phase clouds by Kanitz et al. [2011] at various climatic regions is probably caused by differences in the aerosol conditions. The meteorological influences seem not to play a major role in this context.

The derived statistical properties of vertical motions can be used by modelers to verify simulations of cloud-resolving models or introduce them as parameterizations into large-scale modeling. The ice nucleation observations provide insight into the process of ice formation also usable by modelers. Such information can only be retrieved by real-world observations. There is currently no imaginable way to recreate the movement of a 300 m thin turbulent cloud layer in a laboratory. Even experiments with big cloud chambers like described by Connolly et al. [2009] cannot simulate the combined effects of, e.g., alternating up- and downdrafts, entrainment mixing, radiative cooling, droplet nucleation and ice formation occurring in a mixed-phase cloud layer. Combined observations will therefore be crucial in the research of cloud dynamics and heterogeneous ice formation. The third question of Section 2.5 was, at which point the presence of ice may play a significant role for the development of a mixed-phase cloud. This question could not yet be answered sufficiently, but this work opens some possible ways. End-to-end simulations as presented in Section 2.4 can help to narrow down the constraints on this question.

From the viewpoint of data processing, the LARDA software, developed for this work, was a step forward for TROPOS. This development follows the same philosophy like Cloudnet to bring quality-assured measurement data to the user in near-real time and make access easy. The future goal of this software is to provide fast user-friendly access to any remote-sensing and in-situ data collected at TROPOS and, in this way, to reduce the threshold for interdisciplinary research. The operational inclusion of vertical-velocity measurements from Doppler lidar WiLi into Cloudnet is also under way.

The retrieval of ice particle number concentrations directly from the radar spectra challenges the measurement accuracy of current cloud radars. An accuracy of $\pm 0.1 \text{ m s}^{-1}$ of the vertical-velocity measurement is at the edge of the capability of the current cloud radar system of TROPOS. In future, more efforts have to be taken to provide precision leveling of the antenna, in order to keep the vertical-velocity measurements free of any vector component of the horizontal wind speed. A high uncertainty in the retrieval of particle number concentration and particle flux is introduced by the missing particle classification. Promising work is going on in this field. Matrosov et al. [2012] showed that a MIRA-35 radar is capable of classifying particles by scanning over the zenith and analyzing changes in the depolarization ratio and the phase shift between the two polarization states of the received signal. Such algorithms are currently implemented into the TROPOS MIRA-35 cloud radar. Anyway, the potential of the presented flux retrieval method has been shown to be high. The mutual correction of Doppler lidar, cloud radar and wind profiler measurements could improve the purity of the air-velocity

measurement of the wind profiler and dramatically increase the informative value of the cloud-radar spectra. In turbulent cloud layers, a simultaneously measuring Doppler lidar is needed in any case, because the low time resolution of both radar systems does not easily allow the direct measurement of turbulent motion.

Bibliography

- Albrecht, B. A. Aerosols, cloud microphysics, and fractional cloudiness. *Science*, 245 (4923):1227–1230, 1989.
- Althausen, D., Müller, D., Ansmann, A., Wandinger, U., Hube, H., Clauder, E., and Zörner, S. Scanning 6-wavelength 11-channel aerosol lidar. *Journal of Atmospheric and Oceanic Technology*, 17(11):1469–1482, 2000.
- Althausen, D., Engelmann, R., Baars, H., Heese, B., Ansmann, A., Müller, D., and Komppula, M. Portable Raman lidar PollyXT for automated profiling of aerosol backscatter, extinction, and depolarization. *Journal of Atmospheric and Oceanic Technology*, 26(11):2366–2378, 2009.
- Ansmann, A., Tesche, M., Seifert, P., Althausen, D., Engelmann, R., Fruntke, J., Wandinger, U., Mattis, I., and Müller, D. Evolution of the ice phase in tropical altocumulus: SAMUM lidar observations over Cape Verde. *Journal of Geophysical Research: Atmospheres*, 114(D17):D17208, 2009.
- Ansmann, A., Fruntke, J., and Engelmann, R. Updraft and downdraft characterization with Doppler lidar: cloud-free versus cumuli-topped mixed layer. *Atmospheric Chemistry and Physics*, 10(4):9219–9252, 2010.
- Ansmann, A., Riebesell, M., and Weitkamp, C. Measurement of atmospheric aerosol extinction profiles with a Raman lidar. *Optics Letters*, 15(13):746–748, 1990.
- Ansmann, A., Mattis, I., Müller, D., Wandinger, U., Radlach, M., Althausen, D., and Damoah, R. Ice formation in Saharan dust over central Europe observed with temperature/humidity/aerosol Raman lidar. *Journal of Geophysical Research: Atmospheres*, 110(D18):D18S12, 2005.
- Ansmann, A., Petzold, A., Kandler, K., Tegen, I., Wendisch, M., Müller, D., Weinzierl, B., Müller, T., and Heintzenberg, J. Saharan Mineral Dust Experiments SAMUM-1 and SAMUM-2: what have we learned? *Tellus B*, 63(4):403–429, 2011.
- Baars, H., Ansmann, A., Althausen, D., Engelmann, R., Artaxo, P., Pauliquevis, T., and Souza, R. Further evidence for significant smoke transport from Africa to Amazonia. *Geophysical Research Letters*, 38(20):L20802, 2011.
- Baddeley, D., Carl, C., and Cremer, C. 4Pi microscopy deconvolution with a variable point-spread function. *Applied Optics*, 45(27):7056–7064, 2006.

- Banakh, V. A. and Werner, C. Computer simulation of coherent Doppler lidar measurement of wind velocity and retrieval of turbulent wind statistics. *Optical Engineering*, 44(7):071205, 2005.
- Bauer-Pfundstein, M. R. and Görsdorf, U. Target Separation and Classification Using Cloud Radar Doppler-Spectra. In *Proceedings of the 33rd Conference on Radar Meteorology, Cairns*, 2007.
- Bergeron, T. *Proces Verboux de l'Association de Meteorologie*, pages 156–178. International Union of Geodesy and Geophysics, 1935.
- Biggs, D. S. C. and Andrews, M. Acceleration of iterative image restoration algorithms. *Applied Optics*, 36(8):1766–1775, 1997.
- Bodenschatz, E., Malinowski, S. P., Shaw, R. A., and Stratmann, F. Can we understand clouds without turbulence? *Science*, 327(5968):970–971, 2010.
- Böhme, T., Hauf, T., and Lehmann, V. Investigation of short-period gravity waves with the Lindenberg 482 MHz tropospheric wind profiler. *Quarterly Journal of the Royal Meteorological Society*, 130(603):2933–2952, 2004.
- Boucher, O., Randall, D., Artaxo, P., Bretherton, C., Feingold, G., Forster, P., Kerminen, V.-M., Kondo, Y., Liao, H., Lohmann, U., Rasch, P., Satheesh, S., Sherwood, S., Stevens, B., and Zhang, X. Climate Change 2013: The Physical Science Basis. Contribution of Working Group I to the Fifth Assessment Report of the Intergovernmental Panel on Climate Change. In Stocker, T., Qin, D., Plattner, G.-K., M., T., Allen, S., Boschung, J., Nauels, A., Xia, Y., Bex, V., and Midgley, P., editors, *Climate Change 2013: The Physical Science Basis. Contribution of Working Group I to the Fifth Assessment Report of the Intergovernmental Panel on Climate Change*, chapter Clouds and Aerosols, pages 571–657. Cambridge University Press, Cambridge, United Kingdom and New York, NY, USA, 2014.
- Bucholtz, A. Rayleigh-scattering calculations for the terrestrial atmosphere. *Applied Optics*, 34(15):2765–2773, 1995.
- Bühl, J., Ansmann, A., Seifert, P., Baars, H., and Engelmann, R. Towards a quantitative characterization of heterogeneous ice formation with lidar/radar: Comparison of CALIPSO/CloudSat with ground-based observations. *Geophysical Research Letters*, 40(16):4404–4408, 2013.
- Bühl, J., Engelmann, R., and Ansmann, A. Removing the laser-chirp influence from coherent Doppler lidar datasets by two-dimensional deconvolution. *Journal of Atmospheric and Oceanic Technology*, 29(8):1042–1051, 2012.
- Chen, M.-Y. and Chu, Y.-H. Beam broadening effect on Doppler spectral width of wind profiler. *Radio Science*, 46(5):RS5013, 2011.

- Chernoff, D. I. and Bertram, A. K. Effects of sulfate coatings on the ice nucleation properties of a biological ice nucleus and several types of minerals. *Journal of Geophysical Research: Atmospheres*, 115(D20):D20205, 2010.
- Connolly, P. J., Möhler, O., Field, P. R., Saathoff, H., Burgess, R., Choulaton, T., and Gallagher, M. Studies of heterogeneous freezing by three different desert dust samples. *Atmospheric Chemistry & Physics*, 9(8):2805–2824, 2009.
- Dabas, A. M., Drobinski, P., and Flamant, P. H. Chirp-induced bias in velocity measurements by a coherent Doppler CO₂ lidar. *Journal of Atmospheric and Oceanic Technology*, 15(2):407–415, 1998.
- de Boer, G., Eloranta, E. W., and Shupe, M. D. Arctic mixed-phase stratiform cloud properties from multiple years of surface-based measurements at two high-latitude locations. *Journal of the Atmospheric Sciences*, 66(9):2874–2887, 2009.
- DeMott, P. J., Prenni, A. J., Liu, X., Kreidenweis, S. M., Petters, M. D., Twohy, C. H., Richardson, M. S., Eidhammer, T., and Rogers, D. C. Predicting global atmospheric ice nuclei distributions and their impacts on climate. *Proceedings of the National Academy of Sciences*, 107(25):11217–11222, 2010.
- Deng, M. and Mace, G. G. Cirrus microphysical properties and air motion statistics using cloud radar Doppler moments. Part I: Algorithm description. *Journal of Applied Meteorology and Climatology*, 45(12):1690–1709, 2006.
- Deng, M. and Mace, G. G. Cirrus cloud microphysical properties and air motion statistics using cloud radar Doppler moments: Water content, particle size, and sedimentation relationships. *Geophysical Research Letters*, 35(17):1690–1709, 2008.
- Di Girolamo, P., Summa, D., Cacciani, M., Norton, E. G., Peters, G., and Dufournet, Y. Lidar and radar measurements of the melting layer: observations of dark and bright band phenomena. *Atmospheric Chemistry and Physics*, 12(9):4143–4157, 2012.
- Engelmann, R., Wandinger, U., Ansmann, A., Müller, D., Žeromskis, E., Althausen, D., and Wehner, B. Lidar Observations of the vertical aerosol flux in the planetary boundary layer. *Journal of Atmospheric and Oceanic Technology*, 25(8):1296–1306, 2008.
- Field, P. R., Hill, A. A., Furtado, K., and Korolev, A. Mixed-phase clouds in a turbulent environment. Part 2: Analytic treatment. *Quarterly Journal of the Royal Meteorological Society*, 140(680):870–880, 2013.
- Field, P., Hogan, R., Brown, P., Illingworth, A., Choulaton, T., Kaye, P. H., Hirst, E., and Greenaway, R. Simultaneous radar and aircraft observations of mixed-phase cloud at the 100 m scale. *Quarterly Journal of the Royal Meteorological Society*, 130(600):1877–1904, 2004.

- Findeisen, W. Die kolloidmeteorologischen Vorgänge bei der Niederschlagsbildung. *Meteorologische Zeitschrift*, 55(4):121–133, 1938.
- Fleishauer, R. P., Larson, V. E., and Vonder Haar, T. H. Observed microphysical structure of midlevel, mixed-phase clouds. *Journal of the Atmospheric Sciences*, 59(11):1779–1804, 2002.
- Frehlich, R. Estimation of velocity error for Doppler lidar measurements. *Journal of Atmospheric and Oceanic Technology*, 18(10):1628–1639, 2001.
- Frehlich, R., Hannon, S. M., and Henderson, S. W. Coherent Doppler lidar measurements of wind field statistics. *Boundary-Layer Meteorology*, 86(2):233–256, 1998.
- Frisch, S., Shupe, M., Djalalova, I., Feingold, G., and Poellot, M. The retrieval of stratus cloud droplet effective radius with cloud radars. *Journal of Atmospheric and Oceanic Technology*, 19(6):835–842, 2002.
- Gage, K. S., Williams, C. R., Ecklund, W. L., and Johnston, P. E. Use of two profilers during MCTEX for unambiguous identification of Bragg scattering and Rayleigh scattering. *Journal of the Atmospheric Sciences*, 56(21):3679–3691, 1999.
- Giez, A., Ehret, G., Schwiesow, R. L., Davis, K. J., and Lenschow, D. H. Water vapor flux measurements from ground-based vertically pointed water vapor differential absorption and Doppler lidars. *Journal of Atmospheric and Oceanic Technology*, 16(2):237–250, 1999.
- Goodman, J. W. *Introduction to Fourier Optics*, chapter 2.1.3 Fourier Transform Theorems. Roberts & Company Publishers, third edition, 2005a.
- Goodman, J. W. *Introduction to Fourier Optics*, chapter 4. Fresnel and Fraunhofer Diffraction. Roberts & Company Publishers, third edition, 2005b.
- Groß, S., Tesche, M., Freudenthaler, V., Toledano, C., Wiegner, M., Ansmann, A., Althausen, D., and Seefeldner, M. Characterization of Saharan dust, marine aerosols and mixtures of biomass-burning aerosols and dust by means of multi-wavelength depolarization and Raman lidar measurements during SAMUM-2. *Tellus B*, 63(4):706–724, 2011.
- Grund, C. J., Banta, R. M., George, J. L., Howell, J. N., Post, M. J., Richter, R. A., and Weickmann, A. M. High-resolution Doppler lidar for boundary layer and cloud research. *Journal of Atmospheric and Oceanic Technology*, 18(3):376–393, 2001.
- Gurdev, L. and Dreischuh, T. On an approach for improving the range resolution of pulsed coherent Doppler lidars. *Journal of Modern Optics*, 55(9):1441–1462, 2008.
- Gurdev, L. L. and Dreischuh, T. N. High range resolution velocity estimation techniques taking into account the frequency chirp in coherent Doppler lidars. *Optics Communications*, 219(1–6):101–116, 2003.

- Harris, M., Hand, M., and Wright, A. Lidar for turbine control. *National Renewable Energy Laboratory, Golden, CO, Report No. NREL/TP-500-39154*, 2006.
- Hartmann, S., Niedermeier, D., Voigtländer, J., Clauss, T., Shaw, R. A., Wex, H., Kiselev, A., and Stratmann, F. Homogeneous and heterogeneous ice nucleation at LACIS: operating principle and theoretical studies. *Atmospheric Chemistry and Physics*, 11(4):1753–1767, 2011.
- Hartmann, S., Augustin, S., Clauss, T., Wex, H., Šantl Temkiv, T., Voigtländer, J., Niedermeier, D., and Stratmann, F. Immersion freezing of ice nucleation active protein complexes. *Atmospheric Chemistry and Physics*, 13(11):5751–5766, 2013.
- Henderson, S., Gatt, P., Rees, D., and Huffaker, R. M. Wind Lidar. In Fujii, T. and Fukuchi, T., editors, *Laser Remote Sensing*, pages 469–472. CRC Press, 2005.
- Heymsfield, A. J. and Westbrook, C. D. Advances in the estimation of ice particle fall speeds using laboratory and field measurements. *Journal of the Atmospheric Sciences*, 67(8):2469–2482, 2010.
- Heymsfield, A. J. and Iaquinta, J. Cirrus crystal terminal velocities. *Journal of the Atmospheric Sciences*, 57(7):916–938, 2000.
- Hill, A. A., Field, P. R., Furtado, K., Korolev, A., and Shipway, B. J. Mixed-phase clouds in a turbulent environment. Part 1: Large-eddy simulation experiments. *Quarterly Journal of the Royal Meteorological Society*, 140(680):855–869, 2013.
- Hogan, R. J., Bouniol, D., Ladd, D. N., O’Connor, E. J., and Illingworth, A. J. Absolute calibration of 94/95-GHz radars using rain. *Journal of Atmospheric and Oceanic Technology*, 20(4):572, 2003.
- Hogan, R. J., Mittermaier, M. P., and Illingworth, A. J. The retrieval of ice water content from radar reflectivity factor and temperature and its use in evaluating a mesoscale model. *Journal of Applied Meteorology and Climatology*, 45(2):301–317, 2006.
- Illingworth, A. J., Hogan, R. J., O’Connor, E. J., Bouniol, D., Delanoë, J., Pelon, J., Protat, A., Brooks, M. E., Gaussiat, N., Wilson, D. R., Donovan, D. P., Baltink, H. K., van Zadelhoff, G.-J., Eastment, J. D., Goddard, J. W. F., Wrench, C. L., Haeffelin, M., Krasnov, O. A., Russchenberg, H. W. J., Piriou, J.-M., Vinit, F., Seifert, A., Tompkins, A. M., and Willén, U. Cloudnet. *Bulletin of the American Meteorological Society*, 88(6):883–898, 2007.
- Kanitz, T., Seifert, P., Ansmann, A., Engelmann, R., Althausen, D., Casiccia, C., and Rohwer, E. G. Contrasting the impact of aerosols at northern and southern midlatitudes on heterogeneous ice formation. *Geophysical Research Letters*, 38(17):L17802, 2011.

- Käsler, Y., Rahm, S., Simmet, R., and Kühn, M. Wake measurements of a multi-MW wind turbine with coherent long-range pulsed Doppler wind lidar. *Journal of Atmospheric and Oceanic Technology*, 27(9):1529–1532, 2010.
- Kiemle, C., Ehret, G., Fix, A., Wirth, M., Poberaj, G., Brewer, W. A., Hardesty, R. M., Senff, C., and LeMone, M. A. Latent heat flux profiles from collocated airborne water vapor and wind lidars during IHOP 2002. *Journal of Atmospheric and Oceanic Technology*, 24(4):627–639, 2007.
- Klett, J. D. Stable analytical inversion solution for processing lidar returns. *Applied Optics*, 20(2):211–220, 1981.
- Kollias, P., Tanelli, S., Battaglia, A., and Tatarevic, A. Evaluation of EarthCARE Cloud Profiling Radar Doppler velocity measurements in particle sedimentation regimes. *Journal of Atmospheric and Oceanic Technology*, 31(2):366–386, 2013.
- Kolmogorov, A. The local structure of turbulence in incompressible viscous fluid for very large Reynolds’ numbers. *Akademiia Nauk SSSR Doklady*, 30(4):301–305, 1941.
- Korolev, A. Limitations of the Wegener Bergeron Findeisen mechanism in the evolution of mixed-phase clouds. *Journal of Atmospheric Sciences*, 64(9):3372–3375, 2007.
- Korolev, A. and Field, P. R. The effect of dynamics on mixed-phase clouds: Theoretical considerations. *Journal of Atmospheric Sciences*, 65(1):66–86, 2008.
- Korolev, A. and Isaac, G. Phase transformation of mixed-phase clouds. *Quarterly Journal of the Royal Meteorological Society*, 129(587):19–38, 2003.
- Korolev, A. and Isaac, G. A. Relative humidity in liquid, mixed-phase, and ice clouds. *Journal of the Atmospheric Sciences*, 63(11):2865–2880, 2006.
- Korolev, A. V. and Mazin, I. P. Supersaturation of water vapor in clouds. *Journal of the Atmospheric Sciences*, 60(24):2957–2974, 2003.
- Lebo, Z., Johnson, N., and Harrington, J. Radiative influences on ice crystal and droplet growth within mixed-phase stratus clouds. *Journal of Geophysical Research: Atmospheres*, 113(D9):D09203, 2008.
- Lottman, B. T., Frehlich, R. G., Hannon, S. M., and Henderson, S. W. Evaluation of vertical winds near and inside a cloud deck using coherent Doppler Lidar. *Journal of Atmospheric and Oceanic Technology*, 18(8):1377–1386, 2001.
- Lucy, L. B. An iterative technique for the rectification of observed distributions. *Astronomical Journal*, 79(6):745–754, 1974.
- Luke, E. P. and Kollias, P. Separating cloud and drizzle radar moments during precipitation onset using Doppler spectra. *Journal of Atmospheric and Oceanic Technology*, 30(8):1656–1671, 2013.

- Mace, G. G., Heymsfield, A. J., and Poellot, M. R. On retrieving the microphysical properties of cirrus clouds using the moments of the millimeter-wavelength Doppler spectrum. *Journal of Geophysical Research: Atmospheres*, 107(D24):AAC22, 2002.
- Macke, A., Mueller, J., and Raschke, E. Single scattering properties of atmospheric ice crystals. *Journal of the Atmospheric Sciences*, 53(19):2813–2825, 1996.
- Magono, C. and Chung, W. Meteorological classification of natural snow crystals. *Journal of the Faculty of Science, Hokkaido University. Series 7, Geophysics*, 2(4):321–335, 1966.
- Mandelbrot, B. B. *The Fractal Geometry of Nature*. W.H. Freeman and Co., New York, 1982.
- Matrosov, S. Y., Korolev, A. V., and Heymsfield, A. J. Profiling cloud ice mass and particle characteristic size from Doppler radar measurements. *Journal of Atmospheric and Oceanic Technology*, 19(7):1003–1018, 2002.
- Matrosov, S. Y., Mace, G. G., Marchand, R., Shupe, M. D., Hallar, A. G., and Mc Cubbin, I. B. Observations of ice crystal habits with a scanning polarimetric W-band radar at slant linear depolarization ratio mode. *Journal of Atmospheric and Oceanic Technology*, 29(8):989–1008, 2012.
- Mattis, I., Ansmann, A., Müller, D., Wandinger, U., and Althausen, D. Multiyear aerosol observations with dual-wavelength Raman lidar in the framework of EARLINET. *Journal of Geophysical Research: Atmospheres*, 109(D13):D13203, 2004.
- McFarquhar, G. M., Um, J., and Jackson, R. Small cloud particle shapes in mixed-phase clouds. *Journal of Applied Meteorology and Climatology*, 52(5):1277–1293, 2013.
- Miles, N. L., Verlinde, J., and Clothiaux, E. E. Cloud droplet size distributions in low-level stratiform clouds. *Journal of the Atmospheric Sciences*, 57(2):295–311, 2000.
- Mishchenko, M. I. and Sassen, K. Depolarization of lidar returns by small ice crystals: An application to contrails. *Geophysical Research Letters*, 25(3):309–312, 1998.
- Mitchell, D. L. Use of mass- and area-dimensional power laws for determining precipitation particle terminal velocities. *Journal of the Atmospheric Sciences*, 53(12):1710–1723, 1996.
- Morrison, H., de Boer, G., Feingold, G., Harrington, J., Shupe, M. D., and Sulia, K. Resilience of persistent Arctic mixed-phase clouds. *Nature Geoscience*, 5(1):11–17, 2012.
- Müller, D., Mattis, I., Wandinger, U., Ansmann, A., Althausen, D., and Stohl, A. Raman lidar observations of aged Siberian and Canadian forest fire smoke in the free troposphere over Germany in 2003: Microphysical particle characterization. *Journal of Geophysical Research: Atmospheres*, 110(D17):D17201, 2005.

- Noh, Y.-J., Seaman, C. J., Vonder Haar, T. H., and Liu, G. In situ aircraft measurements of the vertical distribution of liquid and ice water content in midlatitude mixed-phase clouds. *Journal of Applied Meteorology and Climatology*, 52(1):269–279, 2012.
- O’Connor, E. J., Illingworth, A. J., and Hogan, R. J. A technique for autocalibration of cloud lidar. *Journal of Atmospheric and Oceanic Technology*, 21(5):777, 2004.
- O’Connor, E. J., Illingworth, A. J., Brooks, I. M., Westbrook, C. D., Hogan, R. J., Davies, F., and Brooks, B. J. A method for estimating the turbulent kinetic energy dissipation rate from a vertically pointing Doppler lidar, and independent evaluation from balloon-borne in situ measurements. *Journal of Atmospheric and Oceanic Technology*, 27(10):1652–1664, 2010.
- Pappalardo, G., Amodeo, A., Apituley, A., Comeron, A., Freudenthaler, V., Linné, H., Ansmann, A., Bösenberg, J., D’Amico, G., Mattis, I., Mona, L., Wandinger, U., Amiridis, V., Alados-Arboledas, L., Nicolae, D., and Wiegner, M. EARLINET: towards an advanced sustainable European aerosol lidar network. *Atmospheric Measurement Techniques*, 7(8):2389–2409, 2014.
- Paschotta, R. *Field Guide to Laser Pulse Generation*, volume 14, chapter Introduction to optical pulses, pages 1–9. SPIE Press Bellington, 2008.
- Peters, G. and Görtsdorf, U. Cloud Radar - Fundamentals and Measurements. *Promet Meteorologische Fortbildung*, 36(3/4):144–153, 2010.
- Phillips, V. T. J., Demott, P. J., Andronache, C., Pratt, K. A., Prather, K. A., Subramanian, R., and Twohy, C. Improvements to an empirical parameterization of heterogeneous ice nucleation and its comparison with observations. *Journal of Atmospheric Sciences*, 70(2):378–409, 2013.
- Pospichal, B., Kilian, P., and Seifert, P. Performance of cloud liquid water retrievals from ground-based remote sensing observations over Leipzig. In *Proceedings of the 9th International Symposium on Tropospheric Profiling (ISTP), L’Aquila*, 2012.
- Protat, A. and Williams, C. R. The accuracy of radar estimates of ice terminal fall speed from vertically pointing Doppler radar measurements. *Journal of Applied Meteorology and Climatology*, 50(10):2120–2138, 2011.
- Reinking, R. F., Matrosov, S. Y., Brientjes, R. T., and Martner, B. E. Identification of hydrometeors with elliptical and linear polarization Ka-band radar. *Journal of Applied Meteorology and Climatology*, 36(4):322–339, 1997.
- Reitebuch, O., Volkert, H., Werner, C., Dabas, A., Delville, P., Drobinski, P., Flamant, P. H., and Richard, E. Determination of airflow across the Alpine ridge by a combination of airborne Doppler lidar, routine radiosounding and numerical simulation. *Quarterly Journal of the Royal Meteorological Society*, 129(588):715–727, 2003.

- Remmele, S. and Hesser, J. Vector Extrapolation-Based Acceleration of Regularized Richardson Lucy Image Deblurring. In Meinzer, H.-P., Deserno, T., Handels, H., and Tolxdorff, T., editors, *Bildverarbeitung für die Medizin 2009*, Informatik aktuell, pages 400–404. Springer Berlin Heidelberg, 2009.
- Richardson, W. H. Bayesian-based iterative method of image restoration. *Journal of the Optical Society of America*, 62(1):55–59, 1972.
- Riihimaki, L. D., McFarlane, S. A., and Comstock, J. M. Climatology and formation of tropical midlevel clouds at the Darwin ARM site. *Journal of Climate*, 25(19): 6835–6850, 2012.
- Rose, T., Crewell, S., Löhnert, U., and Simmer, C. A network suitable microwave radiometer for operational monitoring of the cloudy atmosphere. *Atmospheric Research*, 75(3):183–200, 2005.
- Sassen, K. Polarization in lidar. In Weitkamp, C., editor, *Lidar: Range-Resolved Optical Remote Sensing of the Atmosphere*, Springer Series in Optical Sciences, pages 19–40. Springer, 2004.
- Schmidt, J., Wandinger, U., and Malinka, A. Dual-field-of-view Raman lidar measurements for the retrieval of cloud microphysical properties. *Applied Optics*, 52(11): 2235–2247, 2013.
- Schmidt, J., Ansmann, A., Bühl, J., Baars, H., Wandinger, U., Müller, D., and Malinka, A. V. Dual-FOV Raman and Doppler lidar studies of aerosol-cloud interactions: Simultaneous profiling of aerosols, warm-cloud properties, and vertical wind. *Journal of Geophysical Research: Atmospheres*, 119(9):5512–5527, 2014.
- Seifert, P., Ansmann, A., Mattis, I., Wandinger, U., Tesche, M., Engelmann, R., Müller, D., Pérez, C., and Hausteiner, K. Saharan dust and heterogeneous ice formation: Eleven years of cloud observations at a central European EARLINET site. *Journal of Geophysical Research: Atmospheres*, 115(D20):D20201, 2010.
- Seifert, P., Engelmann, R., Bühl, J., Schmidt, J., Ansmann, A., Wandinger, U., and Pfitzenmaier, L. Impact of drizzle on lidar-derived aerosol properties below clouds validated with cloud radar. In *Proceedings of the 9th International Symposium on Tropospheric Profiling (ISTP)*, L’Aquila, 2012.
- Shupe, M. D., Kollias, P., Poellot, M., and Eloranta, E. On deriving vertical air motions from cloud radar Doppler spectra. *Journal of Atmospheric & Oceanic Technology*, 25(4):547–557, 2008.
- Simmel, M., Bühl, J., Ansmann, A., and Tegen, I. Ice formation in altocumulus clouds over Leipzig: Remote sensing measurements and detailed model simulations. In *Proceedings of the EGU General Assembly*, Vienna, 2014.

- Skupin, A., Ansmann, A., Engelmann, R., Baars, H., and Müller, T. The Spectral Aerosol Extinction Monitoring System (SAEMS): setup, observational products, and comparisons. *Atmospheric Measurement Techniques*, 7(3):701–712, 2014.
- Smalikho, I., Köpp, F., and Rahm, S. Measurement of atmospheric turbulence by 2- μ m Doppler lidar. *Journal of Atmospheric and Oceanic Technology*, 22(11):1733–1747, 2005.
- Squires, P. The growth of cloud drops by condensation. II. The formation of large cloud drops. *Australian Journal of Scientific Research A Physical Sciences*, 5(3):473–493, 1952.
- Stobie, E. B., Hanisch, R. J., and White, R. L. Implementation of the Richardson-Lucy algorithm in STSDAS. In Crabtree, D. R., Hanisch, R. J., and Barnes, J., editors, *Astronomical Data Analysis Software and Systems III*, volume 61 of *Astronomical Society of the Pacific Conference Series*, pages 296–299. 1994.
- Stratmann, F., Kiselev, A., Wurzler, S., Wendisch, M., Heintzenberg, J., Charlson, R. J., Diehl, K., Wex, H., and Schmidt, S. Laboratory studies and numerical simulations of cloud droplet formation under realistic supersaturation conditions. *Journal of Atmospheric and Oceanic Technology*, 21(6):876–887, 2004.
- Strauch, R. G., Merritt, D. A., Moran, K. P., Earnshaw, K. B., and De Kamp, D. V. The Colorado Wind-Profiling Network. *Journal of Atmospheric and Oceanic Technology*, 1(1):37–49, 1984.
- Tadrous, P. J. BiaQIm Software (available at <http://www.deconvolve.net/bialith>), 2011.
- Taylor, G. I. The spectrum of turbulence. *Royal Society of London Proceedings Series A*, 164(919):476–490, 1938.
- Tinel, C., Testud, J., Pelon, J., Hogan, R. J., Protat, A., Delanoë, J., and Bouniol, D. The retrieval of ice-cloud properties from cloud radar and lidar synergy. *Journal of Applied Meteorology and Climatology*, 44(6):860–875, 2005.
- Tonttila, J., Räisänen, P., and Järvinen, H. Monte Carlo-based subgrid parameterization of vertical velocity and stratiform cloud microphysics in ECHAM5. 5-HAM2. *Atmospheric Chemistry and Physics*, 13(15):7551–7565, 2013.
- Twomey, S. The influence of pollution on the shortwave albedo of clouds. *Journal of the Atmospheric Sciences*, 34(7):1149–1152, 1977.
- Wandinger, U. Introduction to lidar. In Weitkamp, C., editor, *Lidar: Range-Resolved Optical Remote Sensing of the Atmosphere*, Springer Series in Optical Sciences, pages 1–18. Springer, 2004.

- Wandinger, U., Mattis, I., Tesche, M., Ansmann, A., Bösenberg, J., Chaikovski, A., Freudenthaler, V., Komguem, L., Linné, H., Matthias, V., Pelon, J., Sauvage, L., Sobolewski, P., Vaughan, G., and Wiegner, M. Air mass modification over Europe: EARLINET aerosol observations from Wales to Belarus. *Journal of Geophysical Research: Atmospheres*, 109(D24):D24205, 2004.
- Weber, B. L. and Wuertz, D. B. Comparison of rawinsonde and wind profiler radar measurements. *Journal of Atmospheric and Oceanic Technology*, 7(1):157–174, 1990.
- Wegener, A. *Thermodynamik der Atmosphäre*. Verlag von Johann Ambrosius Barth, Leipzig, 1911.
- Weissmann, M., Busen, R., Dörnbrack, A., Rahm, S., and Reitebuch, O. Targeted observations with an airborne wind lidar. *Journal of Atmospheric and Oceanic Technology*, 22(11):1706–1719, 2005.
- West, R. E. L., Stier, P., Jones, A., Johnson, C. E., Mann, G. W., Bellouin, N., and Kipling, Z. The importance of vertical velocity variability for estimates of the indirect aerosol effects. *Atmospheric Chemistry and Physics*, 13(10):27053–27113, 2013.
- Westbrook, C. D., Hogan, R. J., Illingworth, A. J., and O’Connor, E. J. Theory and observations of ice particle evolution in cirrus using Doppler radar: Evidence for aggregation. *Geophysical Research Letters*, 34(2):L02824, 2007.
- Westbrook, C. D., Illingworth, A. J., O’Connor, E. J., and Hogan, R. J. Doppler lidar measurements of oriented planar ice crystals falling from supercooled and glaciated layer clouds. *Quarterly Journal of the Royal Meteorological Society*, 136(646):260–276, 2010.
- Westbrook, C. and Illingworth, A. The formation of ice in a long-lived supercooled layer cloud. *Quarterly Journal of the Royal Meteorological Society*, 139(677):2209–2221, 2013.
- Wulfmeyer, V., Randall, M., Brewer, A., and Hardesty, R. M. 2- μm Doppler lidar transmitter with high frequency stability and low chirp. *Optics Letters*, 25(17):1228–1230, 2000.
- Zhang, D., Wang, Z., and Liu, D. A global view of midlevel liquid-layer topped stratiform cloud distribution and phase partition from CALIPSO and CloudSat measurements. *Journal of Geophysical Research: Atmospheres*, 115(D4):D00H13, 2010a.
- Zhang, Y., Klein, S. A., Boyle, J., and Mace, G. G. Evaluation of tropical cloud and precipitation statistics of Community Atmosphere Model version 3 using CloudSat and CALIPSO data. *Journal of Geophysical Research: Atmospheres*, 115(D14):D12205, 2010b.
- Zhao, Y. and Hardesty, R. M. Technique for correcting effects of long CO_2 laser pulses in aerosol-backscattered coherent lidar returns. *Applied Optics*, 27(13):2719–2729, 1988.

List of symbols

α	Extinction
\bar{P}	Mean pulse power
\bar{v}	Mean vertical velocity
β	Lidar backscatter coefficient
δ	Depolarization ratio
δf	Pulse bandwidth
Δf	Bin size in frequency space of Doppler spectra
Δr	Bin size in range space of Doppler spectra
Δt	Measurement interval
Δv	Bin size in velocity space of Doppler spectra
Δx	Bin size in probability density function (PDF)
ΔZ^*	Critical updraft height
ϵ	Turbulent energy dissipation rate
η	Radar scattering cross section
η_{air}	Kinematic viscosity of air
γ	Coefficient describing the influence of a Gaussian pulse form in the pulse-bandwidth product
γ_0	First coefficient for calculation of the Reynolds number (Re)
γ_1	Second coefficient for calculation of the Reynolds number (Re)
γ_3	Sample skewness
γ_4	Sample kurtosis (Pearson kurtosis)
Λ	Structure size (related to wavenumber)
$\lambda_{R,L}$	Operating wavelength of radar (R) and lidar (L)
μ	Exponent of the Gamma distribution
ν	Discrete index of frequency dimension of Doppler spectra
Ω	Solid angle from backscattering volume to receiver
ϕ	Cloud radar opening angle
ρ	Discrete index of range dimension of Doppler spectra
ρ_{air}	Density of air
σ	Standard deviation
σ^2	Variance
σ_{bt}	$\sqrt{\sigma_b^2 + \sigma_t^2}$
σ_b	Standard deviation introduced by beam-width broadening
σ_t	Standard deviation introduced by turbulence broadening
σ_v	Vertical-velocity standard deviation
θ	Opening angle of first diffraction order of an aperture

a	Coefficient of the area parametrization
A_e	Effective aperture size of a radar telescope
A_i	Mean cross section of the illuminated cylinder
A_p	Area of a particle projected to the fall direction
A_r	$A_p/(\frac{\pi}{4}D_m^2)$
A_t	Telescope area
b	Exponent of the area parametrization
$B(r)$	Backscatter properties at range r
c	Coefficient of the mass parametrization
C	Kolmogorov constant
c_l	Speed of light
D	Volume-equivalent droplet diameter
d	Exponent of the mass parametrization
d_r	Diameter of the system aperture
D_{vh}	Mean between projected vertical and horizontal particle diameter
D_{es}	Equal-sensitivity diameter
D_0	Median particle diameter of the Gamma distribution
d_l	Depth of a turbulent layer
D_m	Maximum diameter of a particle
D^*	Undisturbed signal distribution in deconvolution
$E(k)$	Turbulent-energy spectrum
f	Doppler frequency
F	Particle flux
f_{ref}	Reference frequency in the heterodyne detector of Doppler lidar WiLi
g	Acceleration of gravity
$I_i(r)$	Intensity of the illuminating pulse
k	Wavenumber
$K_{w,i}^2$	Dielectric factor
k_c	Cut-off wavenumber
k_l	Wavenumber related to the layer depth
l	Pulse length
$L_{w,i}$	Lidar ratio α/β
l_f	Folded pulse length
m_p	Mass of a particle
$N_{i,w}$	Number concentration of ice crystals or water droplets
N_ν	Number of points in frequency dimension of Doppler spectra
N_ρ	Number of points in range dimension of Doppler spectra
N_{crit}	Critical number concentration (particle concentration needed for detection)
$O(r)$	Overlap function
p	Air pressure

P_{Ω}	Power scattered into the solid angle of the receiver
P_{\parallel}	Power received in parallel channel
P_{\perp}	Power received in perpendicular channel
P_0	Emitted pulse power of one pulse
P_c	Power collected at a receiver
P_c^*	Test function in deconvolution algorithm
r	Distance from lidar/radar to the observation volume
r_{FZ}	End of Fresnel zone
r_i	Radius of ice crystals
r_w	Radius of water droplets
Re	Reynolds number
$s_{180^\circ} = \left. \frac{\partial s}{\partial \Omega} \right _{180^\circ}$	Differential particle backscattering cross section
S_{Ω}	Scattering cross section of the complete illuminated volume
S_{qsw}	Limit of S_w in quasi-steady solution
S_w	Water vapor supersaturation over liquid water
t	Time
T	Air temperature
u_z	Vertical velocity of air
u_z^*	Critical updraft velocity
u_a	Advection speed
v	Velocity
v_{90}	90%-percentile of the positive vertical-velocity values
$V_i(r)$	Illuminated volume
$V_p(r)$	Pulse volume
v_t	Terminal fall velocity
X^*	Best number
Z	Radar reflectivity factor
Z_{\min}	Minimum detectable radar reflectivity factor

For values a_0 , a_1 , a_2 , B_i , b_i , B_i^* , b_i^* , B_w , b_w , C_0 and τ_p please refer to the original publication of Korolev and Mazin [2003].

List of abbreviations

A-Train	Satellite constellation of NASA
AC	Altostratus cloud
ACI	Aerosol-cloud interactions
AERONET	AEROSOL ROBOTIC NETWORK
AOM	Acousto-optical modulator
AS	Altostratus
BERTHA	Backscatter Extinction lidar–Ratio Temperature Humidity profiling Apparatus
CALIPSO	Cloud-Aerosol Lidar and Infrared Pathfinder Satellite Observations
CCN	Cloud condensation nuclei
CDL	Coherent Doppler lidar
CloudSat	An Earth observation satellite of NASA carrying a cloud radar
CPR	Cloud profiling radar (on CloudSat)
CBH	Cloud base height
CTH	Cloud top height
CTT	Cloud top temperature
CWC	Condensed-water content
CWP	Condensed-water path
DFT	Discrete Fourier transform
DFOV	Dual field of view
DWD	Deutscher Wetterdienst (German Meteorological Service)
EARLINET	European Aerosol Research Lidar Network
FFT	Fast Fourier Transform
FWHM	Full width at half maximum
GDAS	Global Data Assimilation System
HALO	HALO Photonics Company
HATPRO	Humidity And Temperature Profiler
IN	Ice nuclei
IPCC	Intergovernmental Panel on Climate Change
IWC	Ice-water content
IWP	Ice-water path
LACROS	Leipzig Aerosol and Cloud Remote Observations System
LARDA	LACROS Research Data Application
LDR	Linear depolarization ratio (radar-specific notation of δ)
LWC	Liquid-water content
LWP	Liquid-water path

MARTHA	Multiwavelength Atmospheric Raman Lidar for Temperature, Humidity, and Aerosol Profiling (TROPOS)
MIRA-35	35-GHz cloud radar
MO	Master oscillator
MOL	Meteorological Observatory Lindenberg
MOPA	Master oscillator power amplifier
NASA	National Aeronautics and Space Administration
PDF	Probability density function
PO	Power oscillator
PollyXT	Portable Lidar System (TROPOS)
PSF	Point spread function
pyLARDA	LACROS Research Data Application (python implementation)
RL algorithm	Richardson-Lucy algorithm
ROZ	Rocking over the zenith
SAEMS	Spectral Aerosol Extinction Monitoring System
SAMUM	Saharan Mineral Dust Experiment
SC	Stratocumulus cloud
SNR	Signal-to-noise ratio
TKE	Turbulent kinetic energy
TROPOS	Leibniz Institute for Tropospheric Research
UDINE	Up- and Downdrafts in Drop and Ice Nucleation Experiment
UHF	Ultra-high frequency
UTC	Coordinated Universal Time
WBF process	Wegener-Bergeron-Findeisen process
WiLi	Wind Lidar (TROPOS)